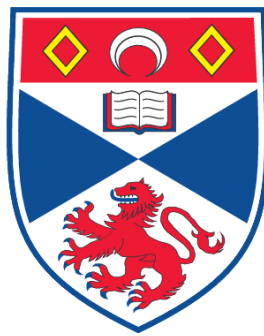


FREE SPACE OPTICAL INTERCONNECTS FOR SPECKLED COMPUTING

Christopher P. Reardon

**A Thesis Submitted for the Degree of PhD
at the
University of St. Andrews**



2009

**Full metadata for this item is available in the St Andrews
Digital Research Repository
at:**

<https://research-repository.st-andrews.ac.uk/>

Please use this identifier to cite or link to this item:

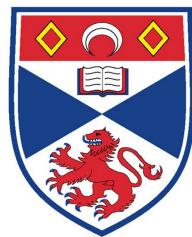
<http://hdl.handle.net/10023/697>

This item is protected by original copyright

**This item is licensed under a
Creative Commons License**

Free Space Optical Interconnects for Speckled Computing

Christopher P. Reardon



University
of
St Andrews

Thesis submitted for the degree of Doctor of Philosophy

March 2009

Declarations

I, Christopher P. Reardon, hereby certify that this thesis, which is approximately 40000 words in length, has been written by me, that it is the record of work carried out by me and that it has not been submitted in any previous application for a higher degree.

I was admitted as a research student in September, 2004 and as a candidate for the degree of Doctor of Philosophy in September, 2004; the higher study for which this is a record was carried out in the University of St Andrews between 2004 and 2009.

Christopher P. Reardon

March 2009

I hereby certify that the candidate has fulfilled the conditions of the Resolution and Regulations appropriate for the degree of Doctor of Philosophy in the University of St Andrews and that the candidate is qualified to submit this thesis in application for that degree.

Thomas F. Krauss

March 2009

In submitting this thesis to the University of St Andrews we understand that we are giving permission for it to be made available for use in accordance with the regulations of the University Library for the time being in force, subject to any copyright vested in the work not being affected thereby. We also understand that the title and the abstract will be published, and that a copy of the work may be made and supplied to any bona fide library or research worker, that my thesis will be electronically accessible for personal or research use unless exempt by award of an embargo as requested below, and that the library has the right to migrate my thesis into new electronic forms as required to ensure continued access to the thesis. We have obtained any third-party copyright permissions that may be required in order to allow such access and migration, or have requested the appropriate embargo below.

Access to Printed copy and electronic publication of thesis through the University of St Andrews.

Christopher P. Reardon

Thomas F. Krauss

March 2009

Acknowledgments

I would like to thank my supervisor Prof. Thomas Krauss for giving me the opportunity to undertake this research and for his constant guidance and input.

I would also like to thank the current and past members of the Microphotonics Research Group who helped create a friendly and stimulating research environment. In particular, I would like to thank Dr Andrea Di Falco and Dr Christina Larsson for their time and contributions. I would also like to thank Dr Stephen Moore, Dr Maarten Verbraeken, Mr David Walsh and Dr David Miller for their support and sometimes helpful suggestions over the years.

Particular thanks goes to Mr George Robb and Mr Steven Balfour for their essential work of maintaining a multitude of laboratory equipment.

I am also grateful to the EPSRC through the SpeckNet consortium that allowed me to undertake this research and are helping to keep the UK at the forefront of scientific research.

Lastly I would like to thank my family for their never ending encouragement and support.

Abstract

The aim of this project was to produce an integrate-able free space optical transceiver for Specks. Specks are tiny computing units that together can form a powerful network called a SpeckNet. The SpeckNet platform is developed by the SpeckNet consortium, which consists of five Scottish Universities and combines computer science, electrical engineering and digital signal processing groups.

The principal goal of creating an optical transceiver was achieved by integrating in-house fabricated VCSELs (with lasing thresholds below $400\text{ }\mu\text{A}$) and custom designed detectors on the SpeckNet platform. The transceiver has a very low power consumption (approximately $100\text{ }\mu\text{W}$), which removes the need for synchronous communication through the SpeckNet thus making the network more efficient.

I describe both static and dynamic beam control techniques.

For static control, I used micro-lenses. I fabricated the lenses by greyscale electron beam lithography and integrated them directly on VCSEL arrays. I achieved a steering angle of 10 degrees with this design. I also looked at integrated gratings etched straight into a VCSEL and observed beam steering with an efficiency of 60%.

For dynamic control, I implemented a liquid crystal (LC) design. I built a LC cell with 30 individually controlled pixels, but I only achieved a steering angle of 1 degree. Furthermore, I investigated two different techniques for achieving beam steering by interference, using coupled VCSELs (a phased array approach). Firstly, using photonic crystals etched into the surface of the VCSEL, I built coupled laser cavities. Secondly, I designed and built bow-tie type VCSELs that were optically coupled but electrically isolated. These designs work by differential current injection causing an interference effect in the VCSELs far field. This technique is the first stepping stone towards realising a phased optical array.

Finally, I considered signal detection. Using the same VCSEL material, I built a resonant cavity detector. This detector had a better background rejection ratio than commercially available silicon devices.

Publications arising from this work

- James Matthews, Matthew Barnes, Christopher Reardon, Karl Welna, Andrea Di Falco, Thomas Krauss and D K Arvind, “Using low power optical receivers for asynchronous communication in SpeckNets,” to be presented at the twelfth Euromicro Conference on Digital System Design Architectures, Methods and Tools, Patras, Greece, August 2009 (Conference Presentation)
- Christopher Reardon, Andrea Di Falco, Karl Welna and Thomas Krauss, “Fabrication of integrated polymer microprisms with VCSELs for location discovery based of free space optical beam steering,” to be presented at SIOE '09, Cardiff, April 2009 (Conference Presentation)
- Karl Welna, Christopher Reardon, Andrea Di Falco and Thomas Krauss, “Fabrication of electrically pumped photonic-crystal laser for ultra-low threshold application,” to be presented at SIOE '09, Cardiff, April 2009 (Conference Presentation)
- Christopher Reardon, Andrea Di Falco, Karl Welna and Thomas Krauss, “Integrated polymer microprisms for free space optical beam deflecting,” *Optics Express*, 17(5): 3424–3428, March 2009 (Journal Publication)
- Christopher Reardon, Andrea Di Falco and Thomas Krauss, “SpeckNet: Optical Communication,” presented at EU–US Workshop, Edinburgh, July 2007 (Poster)
- Christopher Reardon, Christina Carlsson and Thomas Krauss, “SpeckNet: Optical Communication, Beam Conditioning and Location Discovery,” presented at Photon06, Manchester, September 2006 (Poster)
- Christopher Reardon, Christina Carlsson and Thomas Krauss, “SpeckNet: Medical Applications,” presented at Optical Biocips Open Day, Cardiff, April 2006 (Poster)

- Christopher Reardon, Christina Carlsson and Thomas Krauss, “SpeckNet: Optical Communication and Location Discovery,” presented at the ePIXnet Winter School on Optoelectronic Integration: Technology and Applications, Pontresina, Switzerland, March 2006 (Poster)
- Christopher Reardon, 7 SpeckNet Workshops attended, with 9 presentations given (September 2004–2008)

And God said ...

$$\nabla \cdot \vec{B} = 0$$

$$\nabla \cdot \vec{D} = \rho_\nu$$

$$\nabla \times E = -\frac{\delta B}{\delta t}$$

$$\nabla \times H = J + \frac{\delta D}{\delta t}$$

... and then there was light.

Contents

Declarations	i
Acknowledgments	iii
Abstract	v
Publications	vii
Table of Contents	ix
1 Introduction	1
1.1 Communication	3
1.1.1 Radio System	3
1.1.2 Optical System	4
1.2 Current Distributed Networks	5
1.2.1 SmartDust	5
1.2.2 Millibots	6
1.2.3 SunSPOTs	7
1.2.4 WiMoCA	8
1.2.5 Nintendo Wii and Wii Remote	9
1.2.6 Summary	9
2 Optical Communication	11
2.1 Computer Model	14
2.2 Results	16
2.2.1 Optimising the Optical Speck	16
2.2.2 Location Discovery	18
2.3 Conclusions	21
3 VCSEL Fabrication	23
3.1 Introduction	23
3.2 The VCSEL	25
3.2.1 Principal components of the VCSEL	27

3.2.2	Driving the VCSEL	29
3.3	Design and Fabrication	30
3.4	Lithography	31
3.4.1	Photolithography	31
3.4.2	Electron Beam Lithography	32
3.5	Photomask design and Fabrication	33
3.5.1	Mask Pattern Transfer	33
3.6	VCSEL Definition and Fabrication	33
3.6.1	Etching	34
3.6.2	Cleaning	35
3.6.3	Oxidation	36
3.6.4	Oxidation Results	37
3.7	Insulation	39
3.7.1	Silicon Nitride	39
3.7.2	Silicon Dioxide	40
3.7.3	SU8	41
3.8	Contacting	42
3.9	Fabricated VCSEL Characterisation	42
3.10	Conclusions	46
4	Micro-lenses	47
4.1	Introduction	47
4.2	SU8 Optical Elements	48
4.3	SU8 Exposure	49
4.3.1	Low/High Dose Test	49
4.3.2	Dose and Resulting Film Thickness Characterisations	50
4.3.3	Proximity Effect	50
4.3.4	Fresnel Prism Design and Fabrication	52
4.3.5	Local Thermal Reflow	54
4.4	Greyscale Micropism Results	54
4.5	Conclusions	57
5	Integrated Diffraction Gratings	59
5.1	Introduction	59
5.2	The Angled Grating	62
5.2.1	Angled Grating Fabrication	64
5.2.2	Angled Grating Conclusion	64
5.3	Sub-wavelength Gratings	65
5.3.1	Sub-wavelength Grating Design	66
5.3.2	Sub-wavelength Grating Fabrication	67
5.3.3	Sub-wavelength Gratings Conclusions	67

6	Liquid Crystal Cell	71
6.1	Introduction	71
6.2	Liquid Crystal Operation	72
6.3	Liquid Crystal Cell Fabrication	73
6.4	Liquid Crystal Results	76
6.5	Conclusions	79
7	Coupled VCSELs	81
7.1	Introduction	81
7.1.1	Beam Divergence Control	81
7.1.2	Beam Direction Control	82
7.1.3	Phase Control within a Coupled VCSEL	85
7.2	The Coupled VCSEL Array	86
7.2.1	Photonic Crystal VCSEL Design	86
7.2.2	Photonic Crystal VCSEL Fabrication	87
7.2.3	Photonic Crystal VCSEL Preliminary Results	88
7.2.4	Macro Double-VCSEL Mesa Design	89
7.2.5	Macro Double-VCSEL Mesa Fabrication	90
7.2.6	Macro Double-VCSEL Preliminary Results	91
7.2.7	Conclusions	95
8	SpeckNet Optical Transceiver Integration	97
8.1	Introduction	97
8.2	The Photodetector	97
8.3	The Resonant Cavity Detector	101
8.4	Packaging	104
8.4.1	Wire-bonding	105
8.5	Integration with the Speck	107
8.6	Conclusions	111
9	Conclusions	115
	References	123
	Appendix	131

Chapter 1

Introduction

Specks are minute computers that can sense, process and communicate data. A SpeckNet consists of a network of such Specks. Specks are being developed by the SpeckNet consortium, which consists of five Scottish Universities. Combining computer science, electrical engineering (University of Edinburgh), digital signal processing (University of Strathclyde), radio system design and fabrication (University of Glasgow) and human-computer interaction analysis (Edinburgh Napier University) groups. Present device designs call for Specks of the order of 5 cubic millimetres, equipped with their own source of power. Units of the order of 1 cubic millimetre are aimed for, as the longer-term goal. Each Speck therefore constitutes an autonomous micro-computing element. This is in contrast, for example, to the widely used RFID (Radio frequency Identification) tags [1], because RFID tags do not have their own power supply.

A multi-node, fully-distributed network (i.e. a network consisting of nodes without central control) can be thought of as the next natural progression in computing architecture. Computers, since their conception, have been getting ever smaller, more inexpensive and yet more powerful. They have evolved from the extremely large early computers, such as Turing's Colossus (University of Manchester, 1943) [2] and ENIAC (Electronic Numerical Integrator and Computer) (University of Pennsylvania, 1946) [3] (ENIAC consisted of approximately 18,000 vacuum tubes and measured 8 by 100 feet) to mainframes, desktop systems and the now commonplace laptop and PDA (Personal Data Assistant). Communication capabilities have also increased rapidly, starting from hardwired networks, first using copper wire, to optical fibre in today's supercomputers, as well as wireless capability, such as WiFi and Bluetooth. Specks and other distributed networks can be thought of as the epitome of such advancements. Specks will make use of extremely inexpensive processors and completely integrated communication systems.

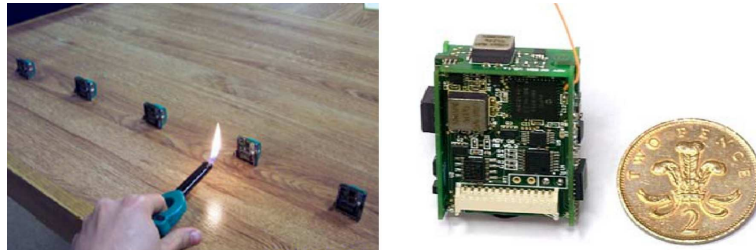


Figure 1.1: Images taken from the SpeckNet collaboration, showing possible uses of the SpeckNet platform, left — fire alarm system where each Speck is equipped with a heat sensor; right — motion capture specks (Orient2). When encapsulated these can be placed on a person to measure the position of their limbs with respect to other Specks.

A SpeckNet that is made up of a large number of Specks can be deployed into the physical environment, where it is able to monitor and report on any number of phenomena. At the same time, it remains practically undetectable due to the small size of the constituent Specks. By deploying such a network, it is possible to functionalise an area, or an object, with processing power, thus making everyday objects intelligent. The large number of potential applications and the importance of this technology are clear, because Speckled computing is leading to increasing integration of digital systems with the physical environment. Such pervasive, or “ubiquitous”, computing systems have already been considered in fields such as agriculture for monitoring greenhouse environments (i.e. temperature, humidity, etc.) [4, 5], health and safety (sensors for building security and fire safety), education (the intelligent kindergarten [6]), military [7], inventory control and asset tracking within the modern office space [8, 9] and others such as interfaces for the disabled [10]. Specks will be able to adapt to many different applications that are adaptations of the core unit— for example, a customer would order certain Specks to suit their own application (i.e. Specks with heat sensors, magnetometers or any number of different sensor configurations (see figure 1.1)).

Due to the small physical size of Specks, they can only carry a limited amount of processor power. However, they can form large networks, so the SpeckNet as a whole is quite powerful. The data collected on each Speck, can be transmitted throughout the network for further processing or for output to a user. Furthermore, the inherent redundancy in such a large multi-node network, increases stability. As such, the network can continue to operate, even if individual Specks fail.

To make sense of the data received from such networks, it is important that the user knows where the data originated (i.e. for tracking purposes you would of course need to know the physical location of the Speck). Location discovery is therefore an important aspect of the SpeckNet platform.

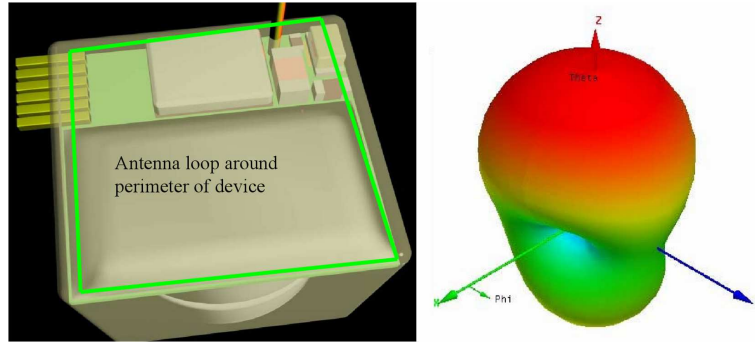


Figure 1.2: Illustration of Speck equipped with a simple loop antenna, also shown is the emission pattern of the antenna.

1.1 Communication

Communication between Specks is of paramount importance, as highlighted above. Initially, it was envisaged that the bulk of communications through a SpeckNet would be carried out by a radio system. However, this is not the only answer to communications within a distributed network. As an alternative, I have explored an optical communication scheme. There are a number of advantages associated with such an optical system compared to a radio based system. In the next section, I will highlight some of these points.

1.1.1 Radio System

A simple radio-based system is made up of a patch or loop antenna (with associated electronics i.e. amplifiers, switches and oscillators) that produces a dipole-like radiation pattern (see figure 1.2). This is fine for point-to-point communication, but for communication through a network, where many nodes may be addressed inadvertently, there is a better option. As an example, consider figure 1.3. Tx is the transmitting Speck which sends its message. On the other end of this conversation, there is the receiving Speck (Rx). If Rx senses a message, it awakens and processes the message. If the message was intended for Rx, it carries out its instructions. However, if the message was not intended for Rx, then it deletes the message and goes back into standby.

This is a relatively simple operation to accomplish, but it consumes energy. In the radio system, every Speck within the communication distance receives the transmitted signal. Inevitably, there is a lot of wasted energy (see figure 1.3). Another

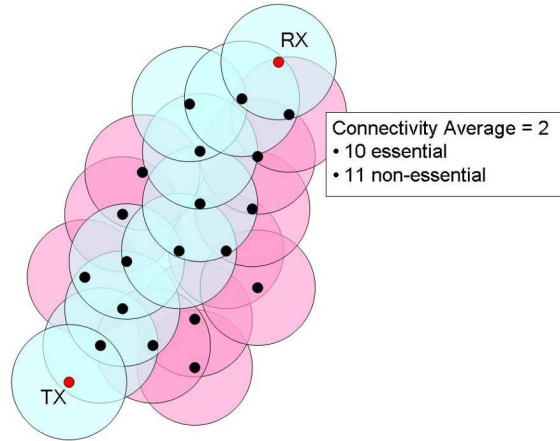


Figure 1.3: Illustration of a typical communication through a radio based SpeckNet. The Specks involved in a single communication across the network are highlighted. The connectivity average is a count of the number of Specks within one communication distance (in this case, the circular shell of the radio emission).

problem is data contention, which happens when a Speck receives a signal from more than one transmitter. A system where every Speck broadcasts its information to any other Speck in range is inefficient, whereas a directed messaging system, where the information is only passed on to the intended receiver, would be better.

1.1.2 Optical System

To address these issues one solution is to narrow the radiation pattern of each transmitter. This can be achieved with radio, by using directional antennae, but at the millimetre scale of the Speck this is difficult. I have therefore explored the potential of using a free-space-optical solution. I chose the infra-red regime, to limit the amount of interference from external light sources. I will also modulate the signal, to allow sources of noise to be filtered out of the communications. By narrowing the radiation pattern I can drastically reduce the number of Specks accidentally awoken by unwanted communications. It also allows me to set-up point-to-point communications (see figure 1.4). Furthermore, by using accurate location discovery, it will be possible to have messages relayed directly to the target Speck. Narrow radiation patterns also allow for more energy efficient communications instead of “losing” energy to empty parts of the SpeckNet (as the radio radiation sphere expands) — this will allow for lower powered communications or for longer distance communications. An optical system is also less susceptible to electronic interference compared to the radio. Optical systems are also more compact and less complicated (i.e. optical systems, for example lasers, do not require local oscillators). Optical systems can

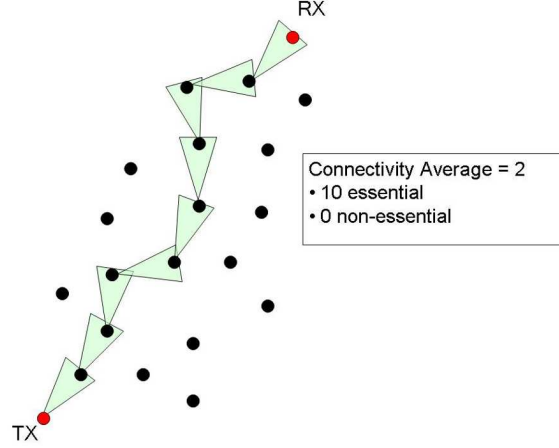


Figure 1.4: Illustration of a typical communication through an optical based SpeckNet, highlighting the Specks involved in a single communication across the network. In comparing this scenario to the one shown in figure 1.3, it can be seen that the optical emitter directionality eliminates the number of unintended Speck receptions.

also be easily integrated onto the size of the proposed SpeckNet platform.

The most important disadvantage is that optical systems require line-of-sight with the intended receiver. To some extent this issue can be addressed by using redundancy, which also makes the network more robust. Redundancy means that SpeckNets are made up of many Specks, more than absolutely necessary. With this increased number of Specks, the probability of having network “line-of-sight” between any two Specks (taking into account multi-hop communication lines), increases.

1.2 Current Distributed Networks

1.2.1 SmartDust

The research group at Berkeley, led by Kristofer Pister [11], can be considered the inventors of the “sensor network”. Their core unit, which is equivalent to our Speck, is referred to as a “mote”. This mote is similar to our Speck and designed to carry a number of embedded sensors including magnetometers, accelerometers, heat, light and humidity sensors. Currently, the SmartDust mote is based on two semiconductor chips, built on top of a class-5 hearing-aid battery — this makes the system approximately 100 mm³ (see figure 1.5). The SmartDust program has looked at a number of communication techniques including the following two platforms:

- Corner cube retro-reflectors — this platform makes use of MEMs controlled

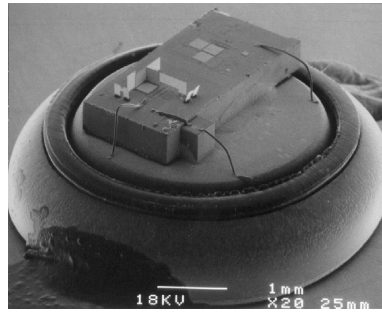


Figure 1.5: Electron micrograph of a Smart Dust mote, 63 mm^3 employing bi-directional communication with a MEMs optics chip containing corner-cube retro-reflector and controlling circuitry [12]

corner cubes that communicate with interrogating systems usually laser beams. The beams are reflected back to the interrogator via the corner cubes. In order to encode information onto this beam the corner cubes on each mote are deformed using a MEMs system.

- On-mote lasers — this platform makes use of an integrated laser to transmit its data. In order to transmit to a given destination the mote employs a MEMs actuated beam steering system, which is made up of a micron scale mirror.

These two platforms have their own benefits and drawbacks. Firstly, the corner cube design benefits from requiring only one type of modulation system — that of the corner cube controller for data encoding. Also the corner cube design benefits from lower power requirements than the on-mote laser, as it only needs to power the MEMs system connected to the retro-reflector. By comparison, the on-mote laser design requires two types of modulation: one to encode data onto the laser beam, and another to control the beam steering MEMs system, so the second design consumes more power. There are, however, two key issues: Firstly, using a small corner-cube poses targeting problems for any interrogating system — finding a SmartDust mote, with a powerful enough optical source, within any networked area is extremely difficult. Secondly, typical MEMs devices require drive voltages of over 100 volts, and up-converting the low battery voltage (of approximately 1.5 volts) to this level is very inefficient. For these reasons it appears that the Berkeley group have abandoned the MEMs based optical approach.

1.2.2 Millibots

Carnegie Mellon University (CMU), with their Millibot program [13] have developed a team of robots. The robots are on the scale of five to ten centimetres. The

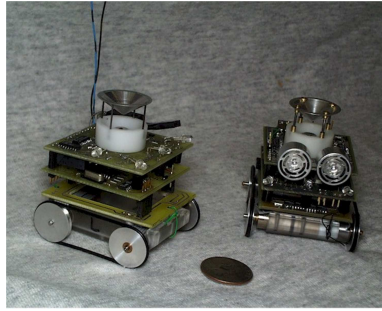


Figure 1.6: Photograph of CMU’s Millibots [13], features to note are the ultrasonic emitter and detectors (underneath aluminium cone)

robots collaborate in order to provide reconnaissance and surveillance (see figure 1.6). They are a mobile sensor platform that carries cameras, temperature and movement sensors. The Carnegie Mellon group have focussed on the larger platform of the Millibot which allows them to increase the amount of energy available. This increases the Millibot’s lifetime and the size of its workable payload. CMU have also developed a robot software architecture that allows the system to act as one logical unit. In order to achieve this, Millibots maintain an accurate sense of each other’s location during movement. They also collect sensor input in order to build maps of their surroundings as well as mission specific information, such as movement within their local environment.

To this end, within each robot, Carnegie Mellon University have used a combination of ultrasound and radio transmitters. The system works on the time-of-flight principle. In order to calculate the distance between each robot the Millibot emits both a radio pulse and ultrasonic chirp. These propagate at different speeds. The receiving Millibot records the time difference between the reception of the radio signal and that of the ultrasound chirp. By assuming that the radio signal travelled instantaneously, the time of flight of the ultrasound chirp is used to calculate the distance. This method provides a Millibot with a resolution of 8 mm over a distance of up to 3 m [13].

1.2.3 SunSPOTs

Sun Microsystems have developed their own wireless sensor network, called Sun Small Programmable Object Technology (SunSPOT) [14]. This system is aimed at large audiences. Sun have implemented a Java virtual machine on each object which makes the system easier to programme for novice users — meaning that SunSPOTs have found their way into the High School classroom [15]. SunSPOTs have a variety of integrated sensors. These include tri-axial accelerometers, temperature, light and



Figure 1.7: Photograph of a Sun Microsystems SunSPOT.

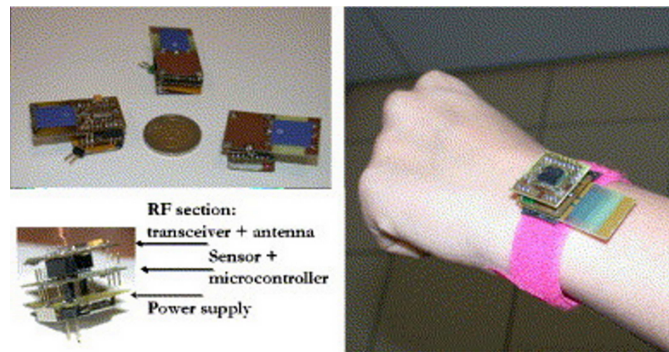


Figure 1.8: Photograph of the University of Bologna's WiMoCA system.

touch sensors. They also include 9 input/output (IO) ports, 4 of which are dedicated output pins, allowing a SunSPOT to affect external devices. The SunSPOT communicates using a radio system, see figure 1.7.

1.2.4 WiMoCA

The University of Bologna, have developed a Wireless sensor node for a Motion Capture system with Accelerometers (WiMoCA) [16]. Their aim is to build a sensor network for the specific application of tracking human movement. The system employs a number of motes mounted on different parts of the human body (making up a Wireless Body-Area Sensor-Network (WBASN)). The system uses a combination of tri-axial integrated accelerometers, microcontrollers and wireless transceivers. The network as a whole is used for gesture recognition, and can be built into a human computer interaction (HCI) application. The WiMoCA system employs tri-axial accelerometers, in order to overcome inaccuracies found from orthogonally mounted bi-axial units — this allows the individual motes to be made smaller (figure 1.8).

1.2.5 Nintendo Wii and Wii Remote

Although not strictly a distributed network, the Wii remote does have the ability to calculate its position relative to the Nintendo sensor bar. I have therefore included it in this section. The Wii remote uses a number of technologies to gather location information. These include accelerometers, gyroscopes and an infra-red camera. The accelerometers and gyroscopes give the Wii remote information about its orientation in space. The camera, in conjunction with the Wii sensor bar, gives information on its physical location. The Wii sensor bar consists of two separate infra-red light emitting diodes (LEDs). The Wii remote “sees” these LEDs and transmits their relative positions, along with the state of the accelerometers and gyroscopes, back to the Wii base unit (the Wii remote communicates with a radio system using the Bluetooth standard, this allows 2-way communication between the Wii remote and base station). Using a combination of triangulation (of the LED positions), and the accelerometer and gyroscope data, the Wii base station then calculates the position and orientation, in 3-dimensional space, of the Wii remote [17].

1.2.6 Summary

The SpeckNet collaboration is positioned between these other technologies, by using optical communication with lower powers than achieved by the SmartDust project. The integration and use of more sensors also makes SpeckNet a more versatile technology. With low power components, an energy neutral platform will be realised, where energy scavenging is used to replenish the Specks energy use (this will be mentioned again in chapter 8). The SpeckNet will then be capable of operating in more environments (i.e. with no replacement of batteries required) than other systems. By using optical location discovery (this will be outlined in chapter 4) the Speck will know its position as accurately as the Millibot system but by using a far smaller unit. Software and systems architecture will be developed so that the SpeckNet can collaborate with current systems such as Sun Microsystems’ SunSPOT objects. Using similar technology to the WiMoCA system, SpeckNets will be employed in gait analysis and motion capture applications. Using this same technology Specks will be employed as novel control systems for next generation games. In summary the SpeckNet’s position in this area is similar to that of Berkeley’s SmartDust. Whereby we shall design and fabricate very small, unobtrusive, multiple-sensor supporting platforms like SmartDust, however, our system will consume far less power making them longer-lived and ultimately more versatile.

Chapter 2

Optical Communication within a Distributed Network

This chapter describes the computer models that I built to investigate the use of optical communication components within the SpeckNet platform. I present work on a 2-dimensional model first, and then discuss some of the work carried out by my colleagues at Edinburgh University. The group at Edinburgh took the 2-dimensional model and expanded it into 3-dimensions.

Figure 2.1a, shows a photo of the first prototype Speck (this device was used extensively throughout the consortium, for the development of components and software). The power supply (i.e. the battery) occupies the majority of the device volume. This highlights the fact that power is the main constraint for operating a Speck, therefore considering the energy requirements of inter-Speck communication is an important task. As mentioned in the introduction chapter, current systems rely on radio for communication [11, 13, 16]. Given the dipole-like emission cone of a radio, all Specks receive any transmitted message from within the local neighbourhood (the local neighbourhood of a Speck is made up of the other Specks located within one communication hop), which is not very efficient.

There are two ways in which data can be transmitted in a distributed network. Firstly, “graph colouring”; each Speck, within a neighbourhood, designates its transmission with a certain colour (i.e. a data code). All other neighbours designate their messages with an alternative colour to avoid data contention. This technique is used elsewhere, for example, to assign aircrafts to flights and in commercial bandwidth allocation for radio stations [18]. The second method is random backoff, whereby a Speck first listens to the transmission channel. If the channel is busy, the Speck sleeps for a random amount of time before trying to communicate again. Both methods have drawbacks; graph colouring, while widely used, generates a large data

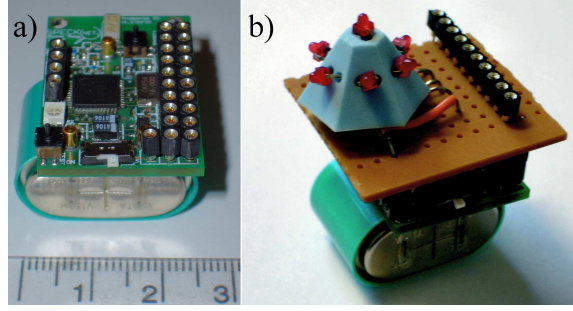


Figure 2.1: a) Photograph of ProSpeckz showing input and output ports. Note battery located on bottom of circuit board. b) ProSpeckz with integrated macro optical emitter board.

overhead that consumes power unnecessarily. Random backoff, on the other hand, can lead to severe delays, especially in large and busy networks.

To address these drawbacks, the emission lobes of each Speck can be made narrower. This reduces the amount of overlap seen within the network. Therefore, in the “graph colouring” process, there are less Specks in a local neighbourhood — reducing data overhead and therefore wasted energy. In the case of random backoff, narrowing the emission cone reduces the number of communication channels, so each channel is available more often — Specks have to check fewer channels before sending a message, so they waste less energy. I will quantify the power saving in terms of the reduction of unintended receptions.

In order to change the emission lobe of each Speck I propose to replace the radio system with an optical one. Using optical beams for communication allows us to use emission cones that can be collimated into a predetermined angle. In order to cover the same solid angle as a radio emission we can use multiple emitters each pointing in a different direction (figure 2.1b). Optical components are also beneficial for integration, within SpeckNet, due to their intrinsically small size. Medium-size arrays of emitters can be realised on mm^2 -size footprints. Optical systems can also operate at very high data rates — as a result, optical communication systems are typically more energy efficient than radio in terms of power required per bit. This is highlighted by an overview of different types of systems used today (table 2.1, figure 2.2).

Figure 2.2 shows that optical communication systems are capable of transmitting greater distances than similar radio systems. They can also achieve higher data rates. Within SpeckNet, the aim is to design a system that has a short to medium transmission range, as highlighted in figure 2.2.

Source	Data Rates (Kbps)	Range (m)	Power (mW)
Bluetooth Class 1 [19]	723	0.1	1
Bluetooth Class 2 [19]	723	2.5	10
Bluetooth Class 3 [19]	723	100	100
Wi-Fi [20]	54 000	10	2 000
Z-Wave [21]	9.6	30	2.5
WiMAX [22]	18 000	8 000	720 000
GSM (GPRS) [23]	22.8	16 000	2 280
IrDA [24]	4 000	0.5	500
TereScope [25]	155 000	510	1.1
SONAbeam 1250-M [26]	148 000	5 300	560
SONAbeam 622-M [26]	715 000	5 400	560
SONAbeam 1250-S [26]	148 000	3 600	280
PAVLIGHT [27]	1 000 000	1 500	75
Cablefree G500 [28]	1 500 000	500	30.2
Cablefree G200 [28]	1 500 000	200	30.2

Table 2.1: Current System's data rates, transmission ranges and transmission powers; split according to radio or optical transmission means.

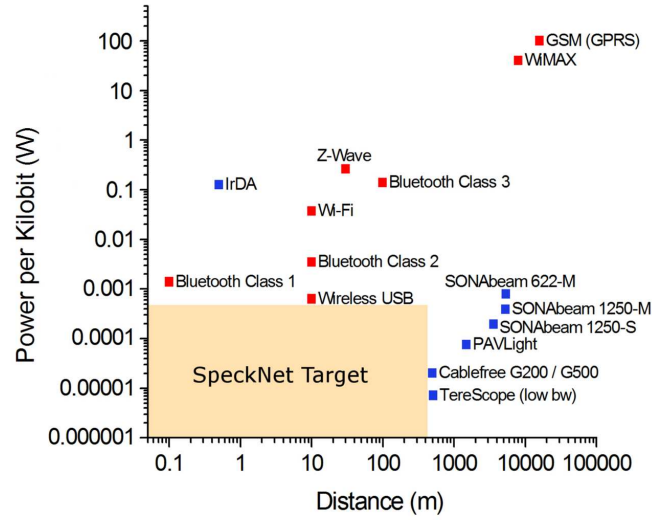


Figure 2.2: Graph showing power required to transmit one kilobit of information against maximum transmission distance. The low power, high transmission range regime is occupied by Free Space Optical systems, represented by blue square symbols, whereas most radio systems, operate in the high power, short range regime (red squares). SpeckNet intends to operate in the low power, mid range regime (Highlighted).

2.1 Computer Model

In order to look at the impact of collimated emitters on SpeckNet communication, I conducted a number of simulations. I varied the number of available emitters and their degree of collimation, ranging from the un-collimated dipole radio to tightly collimated lasers. The simulations use SpeckNet densities as a parameter, i.e. number of Specks per unit volume which makes the results scalable. Specks are then placed within a normalised volume with a random 2-dimensional location. Each Speck is limited to a transmission range of 0.2 units (i.e. 20% of the normalised length that makes up the sides of the normalised volume), which was chosen to represent the limited power available for communication (i.e. limited transmission distance) through a SpeckNet. They are each given a unique identifying number, thus allowing them to be tracked through the program (figure 2.3 and 2.4). The program follows this simplified algorithm:

- 1 Arrange Specks - give each Speck a location coordinate and direction according to random or Gaussian Distribution
- 2 Iterate over Speck list determining each Specks distance and respective direction to each other Speck (record these data in a communication array for each Speck)
- 3 Remove Specks, from each communication array, that are outside the communication range (both distance and direction)
- 4 Output the length of each Specks communication table (i.e. the number of Specks within communication range)
- 5 Output the number of Specks outside of communication range for any other Speck (i.e. the number of Specks with a communication table of length zero)
- 6 Repeat above steps altering the emitter divergence
- 7 Repeat steps above increasing the number of emitters on each Speck

For a SpeckNet to operate, any Speck within the network should be able to communicate with all other Specks. This may be a single-hop point-to-point communication or via intermediate Specks (multi-hop communication). In the given example, each Speck transmits over 20% of the network size. Five hops are therefore required to cover the length of the network, so $5^3 = 125$ Specks are needed to cover the volume (if Specks are evenly distributed (i.e. a grid formation)). For a random distribution, this number increases to 300. It is therefore expected that a message will take

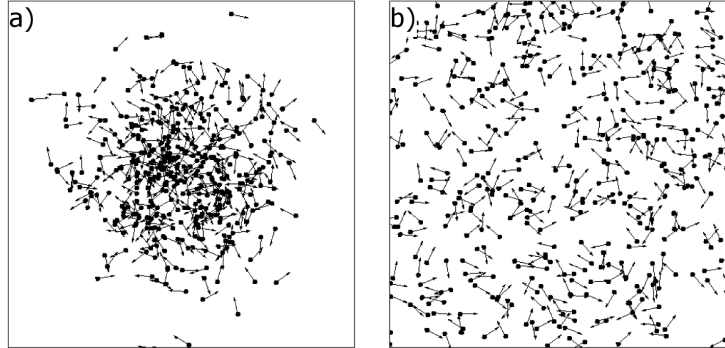


Figure 2.3: Computer representation of two SpeckNets, (left) Gaussian distribution (i.e. representing Specks that have been dropped from a single point) and (right) random distribution (i.e. representing Specks that have been spread throughout an area). The individual Specks are represented by circular marks with their principal direction indicated by arrows. These data arises from the computer model built as part of this work and described previously.

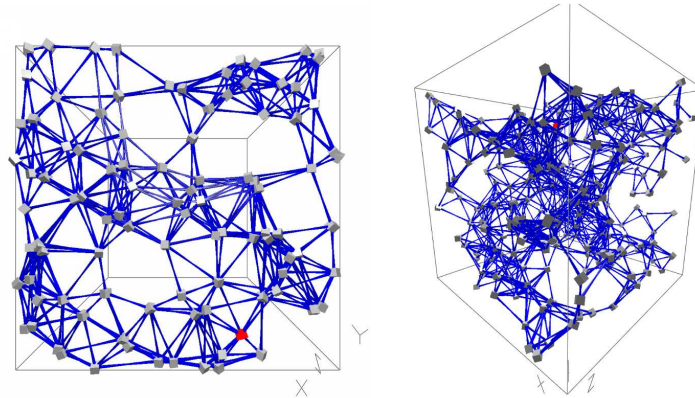


Figure 2.4: Computer representation of two different SpeckNets, simulated by the Edinburgh group. (left) 100 Specks distributed in 2-Dimensions (i.e. analogous to figure 2.3b) and (right) 300 Specks distributed in 3-dimensions (i.e. taking figure 2.3b into 3-dimensions). Images show both Specks (grey cubes) and network connections (blue connecting cones).

between 125 and 300 time-steps to permeate the entire network (a time-step, in the simulation, being defined as one communication between any two Specks).

With my simple 2-dimensional SpeckNet model I was able to obtain results that gave a starting point for further work on the optical communication system. However, the group at Edinburgh University were able to develop the model much further. The model from Edinburgh is capable of considering 3-dimensional networks therefore more accurately predicting real world SpeckNets. It works in a similar manner to my own model by identifying Specks that lie within a Speck's transmission volume (i.e. within some angle, determined by the direction and divergence of the emitter and within some distance). The model also looks at the multiple receivers, that would be required for the final Speck, and their field-of-view limitations. This calculation works much like the transmitter calculation but in reverse. At this point occlusions are also taken into account by looking for Specks that exist in-between the transmitter and receiver. Once these calculations have been made a table of connected Specks can be built and from this table, conclusions much like those presented in the next section are drawn.

2.2 Results

2.2.1 Optimising the Optical Speck

The results presented in this section have been taken from my own model. Edinburgh's model does add useful features to the simulation but does not change the underlying principles set out in this section. Figure 2.5 shows how the average Speck neighbourhood, for a 3-dimensional network, increases with increasing emitter divergence and number of emitters on each Speck. As each Speck keeps track of its own local neighbourhood, reducing the number of Specks in a neighbourhood reduces the total processing requirements.

To ensure that the network is maintained even if individual Specks fail, SpeckNets have built-in redundancy. As such, I place a lower limit on the Speck neighbourhood (it is these neighbourhoods that create the data redundancy). An average neighbourhood of 3 to 4 is a useful compromise. This means that if one of its neighbours fails, a Speck can still communicate with at least one other. It minimises the overhead associated with keeping track of the neighbourhood, while ensuring redundancy even in sparse sections of the network.

Figure 2.6 shows how the number of disconnected subgraphs (i.e. the number of

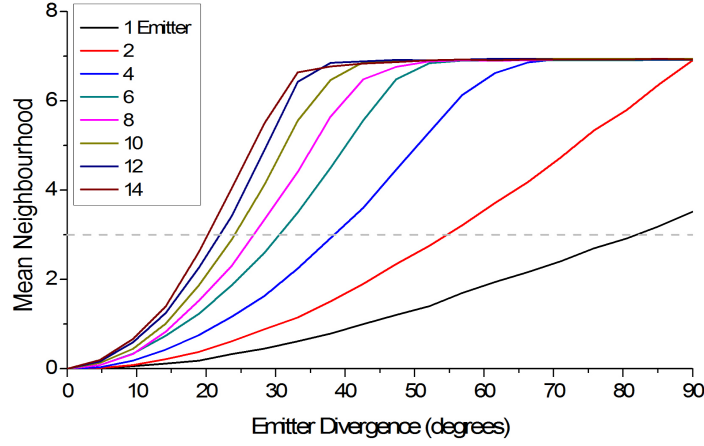


Figure 2.5: Average number of Specks per neighbourhood with respect to Emitter Divergence, assuming a 3-dimensional network containing 300 Specks. A neighbourhood of 3 constitutes a good compromise between processing/tracking requirements and network redundancy. These data arises from the computer model built as part of this work and described previously.

Specks within the network that can talk to some, but not all other Specks), decreases with increasing emitter divergence and number of individual emitters. To obtain a robust network, the number of disconnected subgraphs must be kept to a minimum. From figure 2.6 keeping the number of disconnected subgraphs below 10 results in a Speck requiring at least 2 emitters with a divergence of greater than 75 degrees, or more usefully a Speck with more than 4 emitters with divergence of 25–55 degrees.

Both figure 2.5 and figure 2.6 show that a system consisting of Specks with 12 emitters each with a divergence of 25 degrees, results in local neighbourhoods averaging 3 to 4. The number of disconnected subgraphs within the network is also kept to a minimum. Interestingly, an increase in the number of emitters per Speck results in little to no change in both the Speck neighbourhood and the number of disconnected subgraphs. This puts an upper limit on the number of required emitters. These two results yield the necessary constraints for building and operating a network with optical emitters.

The second simulation looks at the communication of a message from one side of a SpeckNet to the other, by keeping track of the Specks that receive and processes messages. Every time a Speck receives a message it must perform a number of tasks, each of which consumes power. By reducing the number of unintended receptions the power wastage is reduced and the operational lifetime of a Speck is prolonged.

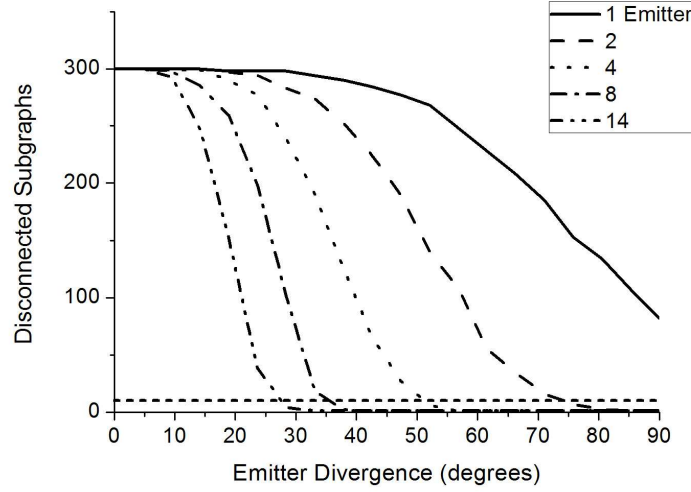


Figure 2.6: Graph of number of disconnected subgraphs within entire SpeckNet with respect to emitter divergence. Dashed horizontal line highlights the 10 disconnected sub-graph point, SpeckNets operating below this point are considered a good compromise for network connectivity. These data arises from the computer model built as part of this work and described previously.

It is both intuitive and evident from figure 2.7 that the number of Specks involved in a communication increases with increasing emitter divergence. Highlighted on the graph are two points, P1 refers to a Lambertian emitter, such as an un-packaged light emitting diode (LED) or radio. The second point refers to a typical vertical-cavity surface-emitting laser (VCSEL) (reasons for the selection, of the VCSEL, for this work will be outlined in chapter 3). A low divergence angle is clearly advantageous, with the lower limit being given by the need for a complete network (figure 2.6), and the upper limit by the imposed local Speck neighbourhood limit (figure 2.5). Taking these considerations into account, a saving of approximately 100 unintended receptions, for a single communication alone, can be achieved. Use of collimated emitters therefore translates into a power saving across the entire network. This model was implemented using Wolfram Mathematica, coding for the model can be found in the appendix.

2.2.2 Location Discovery

Using collimated emitters as a communication system also improves location discovery, as shown in figure 2.9. The algorithm uses the inherent directionality of a collimated emitter, along with received signal strength information (RSSI) data, to measure the direction of a Speck's local neighbour. The algorithm uses a feedback

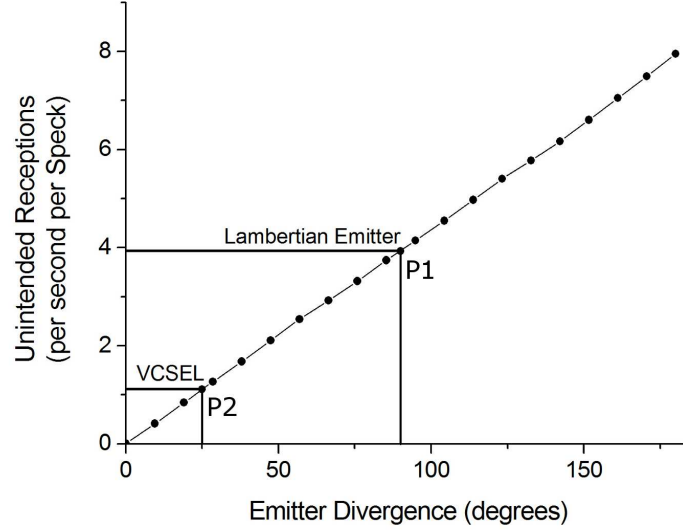


Figure 2.7: Number of Specks involved in a communication across the entire network against emitter collimation angle. Highlighted are radio and VCSEL emission profiles.

loop between the transmitting Speck (Tx), and the receiving Speck (Rx). Tx sends a small message on each of its emitters. Rx detects this message and measures its power; Rx waits for the same message relayed by a different emitter belonging to Tx. Rx takes the ratio of these two powers (taking the more powerful emission as the numerator) and from this data and the known shape of Tx's emission lobes, calculates its direction relative to Tx. Rx then relays this information back to Tx, who stores this information in a list, containing all other Specks within its local neighbourhood. Once a network is set-up, simple triangulation can give the location of each Speck.

Figure 2.10 shows typical results from the Edinburgh University simulation for location discovery throughout an optical SpeckNet. Figure 2.10a shows a sparse SpeckNet, all Specks can communicate with each other, this is shown by the blue connection lines between each Speck within the network. Each Speck has also calculated its location relative to the other Specks, this is done using simple geometry as outlined above (however, the Edinburgh model does not use RSSI data to further refine the Speck location data). The Speck's location errors are shown as black cones emanating from each Speck, the longer the black cone the larger the Specks location error. This change in location error can be seen in figure 2.10b which shows a dense SpeckNet, with more Specks the location error of each Speck is reduced as such the black cones are shorter.

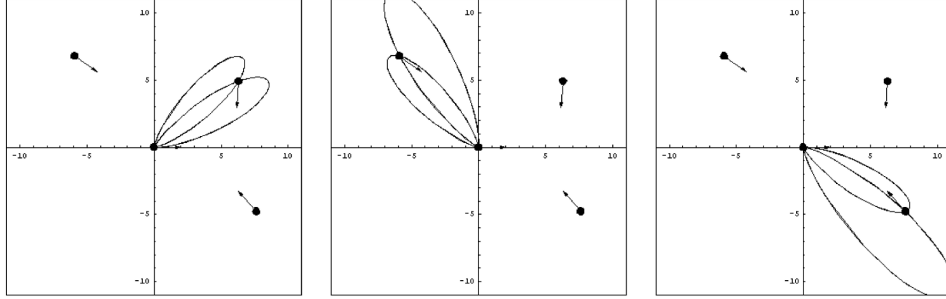


Figure 2.8: Graphical output for location discovery using VCSEL emission profile (from my own simulation), the narrow divergence of the VCSEL increases the resolution of the location discovery algorithm. These data arises from the computer model built as part of this work and described previously.

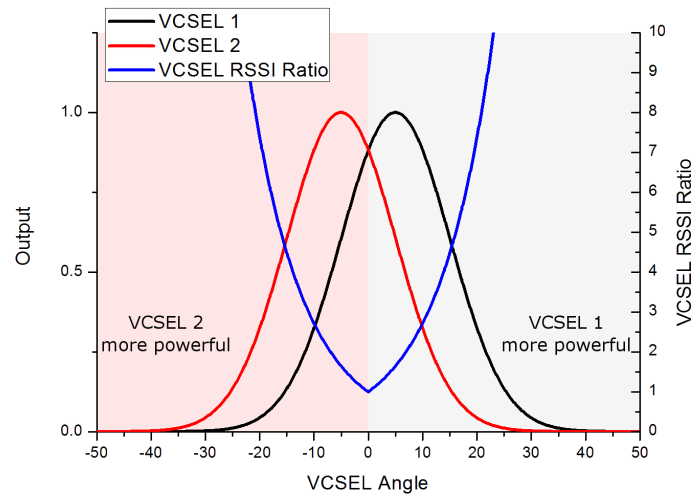


Figure 2.9: Graph of idealised Gaussian emission from 2 emitters belonging to Tx, RSSI ratio data is also plotted. Rx uses this information to discern its angular position relative to Tx.

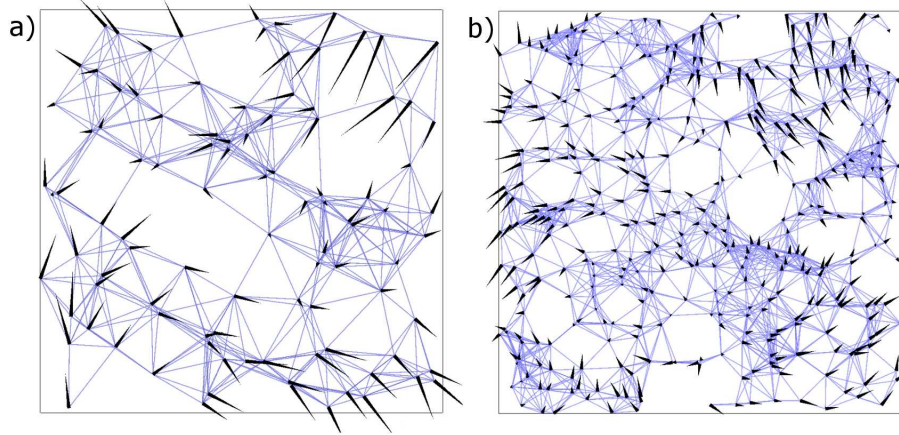


Figure 2.10: Graph of idealised Gaussian emission from 2 emitters belonging to Tx, RSSI ratio data is also plotted. Rx uses this information to discern its angular position relative to Tx.

2.3 Conclusions

I have discussed three critical aspects of emitters deployed for free-space communication in a distributed network. A typical embodiment for the different types of emitters is radio for the un-collimated case, and lasers for the collimated case. Given that the main constraint in a SpeckNet is the availability of power, collimated emitters by virtue of their narrow emission, are more efficient at transmitting information over longer distances. In addition, typical collimated systems, being optical, are able to operate at higher bandwidths. As a result, collimated optical systems tend to occupy the long-distance, low power area of free-space communication systems. Secondly, I have shown that additional power saving is afforded by collimated emitters due to the targeted fashion by which they transmit information. This leads to a reduced number of unintended receptions, so less unnecessary “wake-up calls” throughout the network. Finally, I have discussed the increased accuracy in determining the mutual location of Specks using collimated emitters, which is of particular interest for dynamic systems that need to update their location map frequently.

This work has given me a starting point for the development of an all optical transceiver. From these simulations, an emitter with a very narrow emission cone, although useful for long-haul communication, is not optimal for the SpeckNet platform. A divergence of around 25 degrees has been chosen for the optical emitter — using VCSELs as the source allows this. A multiple emitter design will be adopted to minimise the number of disconnected subgraphs and to attain a suitable Speck local neighbourhood size. For this, beam steering is investigated.

Chapter 3

VCSEL Fabrication

3.1 Introduction

Before this work could commence a choice between different emitters had to be made. I chose to use the vertical-cavity surface-emitting (VCSEL) for a number of reasons, these will now be outlined. To begin with I had to choose which semiconductor emitter to use, there are three principal choices those of the light emitting diode (LED), the VCSEL and the edge emitting laser (EEL). The EEL was discounted from the choice quite easily, the final aim of this project was to produce a communication array, EELs do not lend themselves to array integration because of their cleaving requirements.

The next choice was between the LED and the VCSEL, which was a far more difficult choice. Both the LED and VCSEL are fabricated in a similar manner, as such this could not be used to distinguish them, the VCSEL tends to have tighter fabrication constraints but not massively more. In the end this choice came down to the intended application for the devices. I aim to build an optical communication system that can be used instead of (or as a supplement to) a radio based system. Therefore, I needed to provide something that radio would find difficult i.e. point-to-point communication. A radio broadcasts in all directions, this is an inefficient means of communicating especially if the transmitted message is only meant for one other receiver. Using optical components it is quite easy to limit the angular extent of a transmission. The VCSEL then becomes the obvious choice, as the on-axis power of a VCSEL (i.e. the amount of light reaching a detector on the same optical axis as the emitter) is far greater than that of an LED. While it is true that at low drive currents an LED tends to have higher on-axis power than a VCSEL, once the threshold current (the point at which a VCSEL begins to lase) of the VCSEL has been surpassed its on-axis power increases massively compared to the LED. Therefore it is important to fabricate low-threshold VCSELs. This is possible with oxide

confined air-post VCSELs which will be described in this chapter. This project also aims to use a phased array approach to beam conditioning this technique will use bottom emitting sources which are only available when using the VCSEL, phased arrays are also only possible with a laser as the emission source, as such the LED could not be used.

The final choice that had to be made was that of wavelength. Exactly what wavelength should be chosen for this system. I chose to use 980 nm for a number of reasons, two of which are simply reliability and maturity — infra-red technology has existed for a long time and is well documented, therefore I could not foresee any major problems arising from using this regime. The materials that are used in creating these lasers have also been used extensively within my research group as such this knowledge base would be useful. It is also true that the materials required for fabrication, are some of the best with which to work, for example, very efficient dielectric mirrors can be fabricated, for the 980 nm regime, using materials that can be grown together with relative ease. Yet another reason for this choice was that of expediency — short-range optical communications already in production use the infra-red regime i.e. television remote controls, mobile phone-to-mobile phone communication, laptop and personal-data assistant (PDA) communication, although these technologies could not be used directly within the SpeckNet program (due primarily to power restrictions), I felt it would be useful if in the future inter-operability could be built into the SpeckNet, allowing PDAs, laptops or mobiles to be used as interrogating devices for implemented SpeckNets. Finally, another reason, that is evident from the proliferation of existing technology, is that of safety (in particular eye-safety) using low power infra-red emitters safety considerations are very easy to meet.

At this point I would like to mention one other optical regime that is receiving a lot of interest at the moment, that of deep ultra-violet (DUV) non-line-of-sight (NLOS) communication. This approach uses the sun-blind region of the optical spectrum, as such interference from the sun is minimal, using the infra-red regime will require optical filtering (this will be discussed in chapter 8), therefore the DUV regime would seem like a good choice. This type of communication system works on the principle of scattering within the atmosphere. A UV source is directed upwards where upon the UV radiation scatters in all directions, the detectors (which must be very sensitive due to only receiving low power scattered light) then measure this light and retrieve messages encoded on the emission. This approach does give NLOS communication to the DUV system, however, point-to-point communication is difficult. Therefore, this type of system could replace the radio based system but could not improve on the communication quality i.e. data collision and contention would still

need to be dealt with at a software level. The technology required to fabricate such DUV emitters and detectors is also in its infancy compared to that of the infra-red regime and development of this technology would prove to be a research project in itself.

3.2 The VCSEL

The Vertical-Cavity Surface-Emitting Laser (VCSEL) was developed in 1979 by Soda, Iga, Kitahara and Suematsu [29]. VCSELs are designed to emit vertically, as such they have very small gain volumes. The gain of a VCSEL is typically provided by a number of quantum wells. In my case, the VCSEL material has 3 quantum wells made up of indium gallium arsenide (*InGaAs*) and gallium arsenide phosphide (*GaAsP*), with a photoluminescence (PL) peak wavelength of 970 nm. The VCSEL cavity, on the other hand, is centred around 980 nm. The cavity is detuned from the PL wavelength because during operation, the VCSEL heats up and the PL shifts, bringing the cavity and PL into alignment. To create the laser cavity, VCSELs make use of highly reflective mirrors — in the form of distributed Bragg reflectors (DBRs). A DBR is made up of alternating high and low refractive index material. This VCSEL wafer is made from the ternary semiconductor aluminium_x gallium_{1-x} arsenide (*Al_xGa_{1-x}As*), where x denotes the amount of gallium replaced with aluminium¹.

The feedback is created by a grating with a period of $\frac{\lambda_0}{2n_{eff}}$, where λ_0 is the required wavelength of the VCSEL in free-space (i.e. 980 nm) and n_{eff} is the effective index typically near the average index of the grating. Such a grating has a characteristic stop band where light is reflected rather than transmitted through the Bragg stack. In my VCSEL material, quarter wavelength layers of *Al_{0.12}Ga_{0.88}As* (refractive index, $n \approx 3.39$ at 980 nm) and *Al_{0.9}Ga_{0.1}As* ($n \approx 2.95$ at 980 nm) are alternately grown. The laser cavity is created by forming a defect within the grating that creates a transmission spike at the laser wavelength (seen as a dip in figure 3.1).

Due to the small gain volume (only 3 quantum wells), the reflectivity of the cavity DBRs are of order 99%. This provides sufficient optical feedback to overcome the cavity losses. VCSELs come in two principal types — top emitting and bottom emitting. These differ in the reflectivity of their output coupler. Top emitters have a top mirror with a lower reflectivity, this provides Laser output through the top surface (bottom emitters have the opposite arrangement).

¹both *GaAs* and *AlAs* have almost the same lattice constant, this makes the two materials good for DBR construction. Aluminium can be substituted for gallium, within the crystal, causing only minimal stress. This allows many layers of different dielectric constant to be grown together.

The reflectivity (R) of a DBR can be calculated (from [30]):

$$R = \left[\frac{n_o(n_2)^{2N} - n_s(n_1)^{2N}}{n_o(n_2)^{2N} + n_s(n_1)^{2N}} \right]^2 \quad (3.1)$$

where: N is the number of mirror pairs within the DBR; and n_o , n_1 , n_2 , and n_s are the respective refractive indices of the medium surrounding the DBR, the alternating high and low index material making up the DBR, and the index of the substrate used for the structure.

Inserting the values for my material into equation 3.1 (i.e. a substrate of *GaAs*, $n_s = 3.52$; a low and high index material of indices $n_1 = 2.95$ and $n_2 = 3.39$; emitting into air, $n_o = 1.00$), yields the following result: For a top emitting VCSEL, with 24 top mirror pairs and 39 bottom mirror pairs the reflectivity of the top mirror is $R_{top} = 0.9824$ and that of the bottom mirror is $R_{bottom} = 0.9997$.

Due to the way a VCSEL is generally constructed (i.e. from a circular mesa), the laser emission from a VCSEL tends to have a circular profile. This provides an advantage compared to the astigmatic output from typical edge emitting lasers. The small cavity has a large free spectral range (FSR), so single longitudinal mode operation is achieved. Considering the equation for the FSR:

$$FSR = \Delta\nu = \frac{c}{2nL} \quad (3.2)$$

or, in wavelength:

$$\Delta\lambda = \frac{\lambda^2}{2nL} \quad (3.3)$$

where: n is the effective index, and L the effective length of the VCSEL cavity. The effective length of the cavity takes into account both the central cavity region and the penetration depth of the DBR mirrors. The penetration depth is calculated using the following equation (taken from [31]):

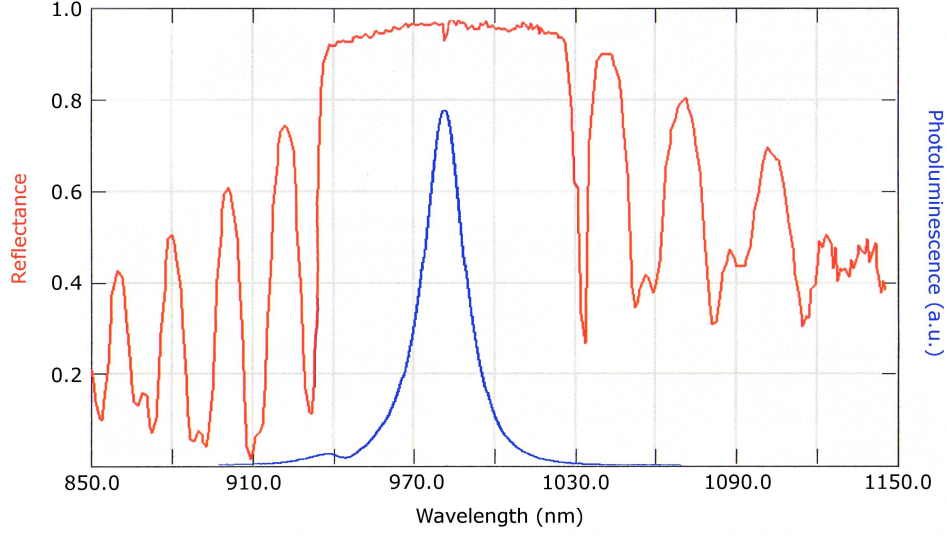


Figure 3.1: Separate charts taken from VCSEL wafer customer report (IEGENS-17-8). Combined here to show VCSEL cavity reflectance profile overlayed with active layer photoluminescence (PL) plot (PL plot shifted by 10 nm for clarity).

$$L_{\text{penetration}} = \frac{\lambda}{4\Delta n} \quad (3.4)$$

where: Δn is the refractive index difference between the materials of the DBR (i.e. $\Delta n = 3.39 - 2.95$). For this material a penetration depth of 557 nm results. Taking this into account along with the central cavity region length (i.e. $\frac{3\lambda}{2n} \approx 420$ nm). The effective cavity length of the VCSEL is approximately 1534 nm, resulting in an FSR of approximately 95 nm. Therefore, only one axial mode is supported by the available gain and the high-reflectivity region of the Bragg grating, see figure 3.1.

3.2.1 Principal components of the VCSEL

The semiconductor wafer:

I investigated both top- and bottom-emitting VCSELs which, along with the wavelength of interest (i.e. 980 nm), determined the choice of wafer. The material was grown by IQE plc. to a standard design, including three quantum wells to supply the gain. The material is doped to make a diode. The top and bottom DBRs are doped with carbon (*C*) and silicon (*Si*), respectively. Carbon, being a group IV element acts as an acceptor by replacing the group V element arsenic in the crystal, making the material p-type. Silicon, also being a group IV element, however, acts

as donor by replacing gallium, resulting in an n-type material. The central region of the wafer (around and including the quantum wells) is left un-doped creating an intrinsic layer.

DBR mirrors:

I used an air-post design which simplifies the fabrication procedure, but means that the drive current has to pass through both DBRs, the active region and the wafer substrate. This creates a relatively large ohmic resistance. In order to reduce this resistance, the wafer uses index-graded top and bottom DBRs. Within each mirror pair, instead of growing $Al_{0.9}GaAs$ directly on top of $Al_{0.12}GaAs$, a 20 nm transition layer of $Al_{0.9-0.12}GaAs$ is added. This smoothes the resistive barrier between the different layers.

For the top emitting wafer, the top DBR consists of 24 mirror pairs, while the bottom mirror consists of 39 pairs. The bottom emitting wafer on the other hand, features 31 top mirror-pairs and 28 bottom mirror-pairs (this mismatch ensured emission from the top or bottom of each wafer).

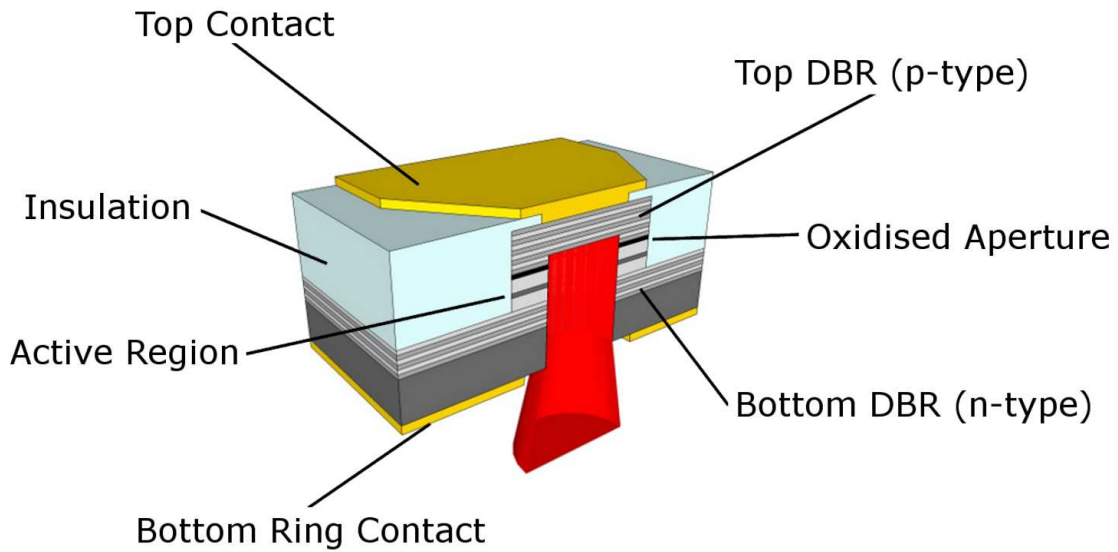


Figure 3.2: Overview image of a simplified bottom emitting VCSEL highlighting the principal components.

Oxide Aperture:

In order to keep the current from the etched surfaces to avoid unwanted surface recombination, VCSELs employ an internal aperture. This helps focus the drive

current into the small volume of the active region. This aperture is made from a high-aluminium content layer (here $Al_{0.98}Ga_{0.02}As$) located above the active region. This layer is then partially oxidised during fabrication of the VCSEL. Aluminium oxide provides both an optical (aluminium oxide has a lower refractive index than aluminium arsenide) and current aperture (aluminium oxide is an electrical insulator) within the laser.

Laser Substrate:

The substrate is typically 300–500 μm thick and does not form part of the laser cavity. It can therefore be patterned without affecting the VCSEL operation directly. This aspect can be used to control the output characteristics of the VCSEL and will be discussed in a subsequent chapter.

Top contact:

The top contact is made from 200 nm of gold. It is evaporated on to the top surface of the VCSEL with an adhesion layer of 20 nm nickel, nickel-chromium or chromium. Diffusion of this material into the semiconductor reduces the potential barrier between the contact and the wafer. For top emitting VCSELs the contact is shaped to allow Laser emission (i.e. a ring contact is formed).

Bottom contact:

Typically, the bottom contact is made up of five layers consisting of gold, germanium, gold, nickel, and gold — with thicknesses of 14-, 14-, 14-, 11- and 200 nm respectively. This recipe is used because the germanium will diffuse into the VCSEL acting as an n-type dopant.

3.2.2 Driving the VCSEL

VCSELs can be designed to have low thresholds, due to their extremely small (3–4 μm) aperture and correspondingly small gain volume. I will present results, in this work, that show lasers with 500 μA thresholds. The threshold can be further reduced by developing smaller apertures. In a later section I will outline how this can be achieved although the corresponding tolerances are difficult to control.

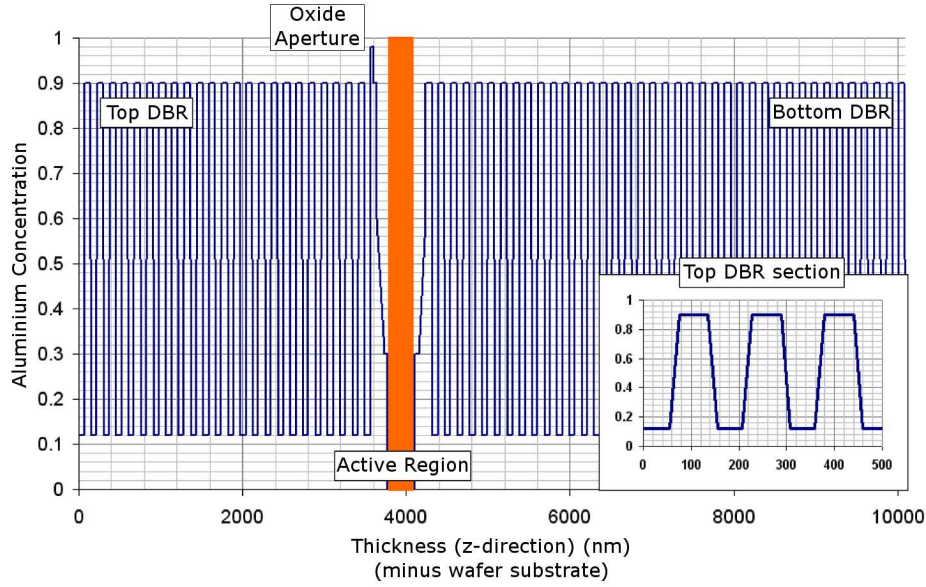


Figure 3.3: Graph of VCSEL wafer structure, focussing on aluminium concentration throughout wafer, graph shows both top and bottom DBR along with oxidation aperture and active layers. Inset: Shows graded-index between mirror pairs

3.3 Design and Fabrication

Mesa size

The main constraint of the SpeckNet platform is power. Low threshold emitters are therefore more important than high output power devices. This means that making the VCSEL mesas as small as practical was a priority.

Control over the oxidation process to create the oxide aperture is therefore a critical issue. To fabricate the internal aperture the VCSEL is placed within an oxidation oven typically for 20 minutes at a sample temperature of 450 °C. The device diameter is typically kept below 100 μm so that the oxidation proceeds linearly [32]. Another constraint is the shape of the electrical contact. For top emitting devices, the top contact is formed into a ring, which reduces the useable surface area of the mesa. Therefore, designing the mesa to be as large as possible is beneficial for the contact surface area. This results in low contact resistances.

Integration of beam controlling optics is another concern. Here, top emitters have an advantage over bottom emitters, because beam controlling structures can be integrated directly onto/into the surface of the mesa and structures can be aligned easily to the mesa (which is more difficult for bottom emitters). On the other hand, integrating beam controlling structures onto/into the top surface of a VCSEL could

compromise the top DBR, while this is not an issue for bottom emitting VCSELs. The integrated optics can use the substrate of the wafer.

In summary:

- Application of VCSELs in SpeckNet demands low threshold devices \Rightarrow small mesas are required.
- Control over the oxidation process is important \Rightarrow large mesas make this difficult.
- The electrical contact area should be maximised \Rightarrow larger mesas are preferred.
- Integration of beam controlling structures onto/into the VCSELs are alignment sensitive \Rightarrow this is achieved more easily with larger mesa diameters.

The compromise between all four areas was to choose a diameter of $50\text{ }\mu\text{m}$. This is: relatively large (should show good output power); easily aligned to using photolithography and EBL (good for beam controlling structures); well below the oxidation “saturation” point of $100\text{ }\mu\text{m}$ [32] (oxidation will be linear with time); and large enough for a top ring-contact.

3.4 Lithography

I used both photolithography and e-beam lithography (EBL) for the fabrication of my VCSELs. E-beam lithography allows rapid prototyping of new designs, whereas photolithography is a faster overall process and is preferred once the process is established and if the resolution allows it (EBL systems have resolutions below 50 nm while a photolithography system is limited to approximately $1\text{ }\mu\text{m}$).

3.4.1 Photolithography

The most important aspect of photolithography is the photo-resist as it contributes to the smallest resolution achievable in the process. The photo-resist also acts as the etch mask in subsequent fabrication steps. There are two types of photo-resist, namely positive and negative. In a positive resist, the ultra-violet (UV) radiation “cuts” the polymer chains that make up the resist, so the exposed areas become soluble to the developer. Alternatively, in a negative resist, the UV radiation promotes “cross-linking” of the polymer chains, so the un-exposed areas are washed away by

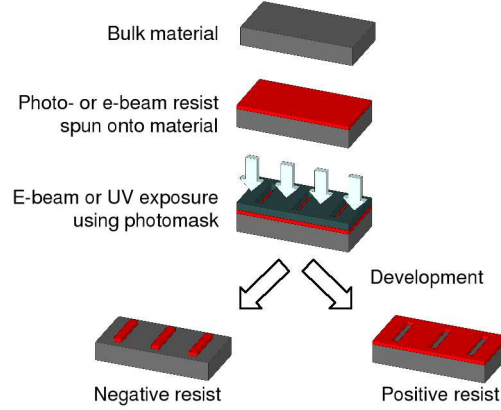


Figure 3.4: Process protocol for lithography.

the developer. The process is summarised in figure 3.4.

Exposure is a combination of both dose and time. In the photolithography system the exposure dose is constant, (i.e. a UV bulb is used with a power of approximately 2.8 mW/cm^2). So the exposure is controlled by varying the exposure time. Due to the steep absorption curve of the resist, the exposure process is typically digital, either on or off. A process known as greyscale lithography is also possible, which aims to expose only part of the resist. This can be used to fabricate 3-dimensional features as discussed in chapter 4.

The typical resolution of the photolithography system is of the order of $5 \mu\text{m}$, but I have realised features down to $2 \mu\text{m}$.

3.4.2 Electron Beam Lithography

In contrast to photolithography, electron beam lithography (EBL) is a serial process. In EBL an electron-beam is scanned across the resist-coated sample. Both positive and negative resists exist for EBL, much like photolithography. The smallest patterns that can be produced, using EBL, are of the order 30 nm . These are limited by the scattering of the electrons in the resist. Greyscale lithography is achieved by varying exposure time. Greyscale EBL is simpler than greyscale photolithography because it is a direct-write process. Which is why I used it for the microprisms described later.

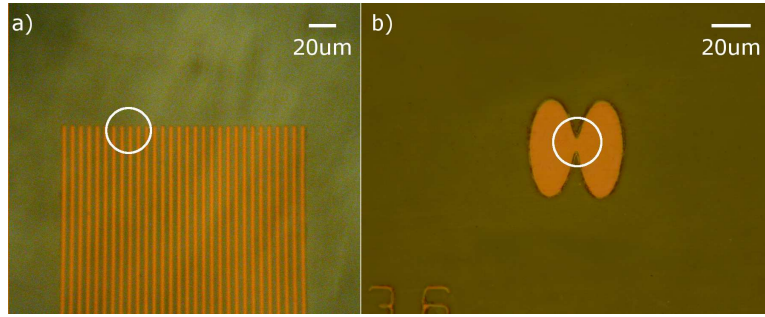


Figure 3.5: Photograph of completed photomask a) has features of $5\ \mu\text{m}$ and b) has features of approximately $2\ \mu\text{m}$.

3.5 Photomask design and Fabrication

3.5.1 Mask Pattern Transfer

A photomask is first patterned using EBL and a suitable electron beam resist. The pattern is transferred into the mask material by wet-etching. The mask is submerged in a solution of hydrochloric acid and deionised water for 8–10 minutes. A 1:1 solution ratio is preferred although transfer can be achieved with weaker solutions over longer times.

I redeveloped this process, during my research, because the resolution achievable began to deteriorate. Each mask suffered from low resolution, and it was evident that during the wet-etch stage undercut was occurring, ruining the pattern. To fix this problem I increased the number of PMMA layers from two to three. The EBL dose was altered to take this into account. With three layers of PMMA some undercut was still observed. The concentration of the acid etchant was reduced to 3:1 $\text{H}_2\text{O}:\text{HCl}$, and the etching time increased. I found that an etch time of 1 hour produced good masks, with resolutions down to approximately $5\ \mu\text{m}$. To increase the mask resolution it can be further etched in steps of 15 minutes. The etchant temperature was also stabilised, by keeping the etchant at $23\ ^\circ\text{C}$ using a water bath. Using this method I have produced optical masks with resolutions of approximately $2\ \mu\text{m}$.

3.6 VCSEL Definition and Fabrication

The fabrication process starts by cleaning the sample in acetone and isopropyl alcohol (IPA), which leaves the surface clear from organic contaminants. A single layer of resist (Microposit S1818 photo resist from Rohm and Haas) is spun onto the

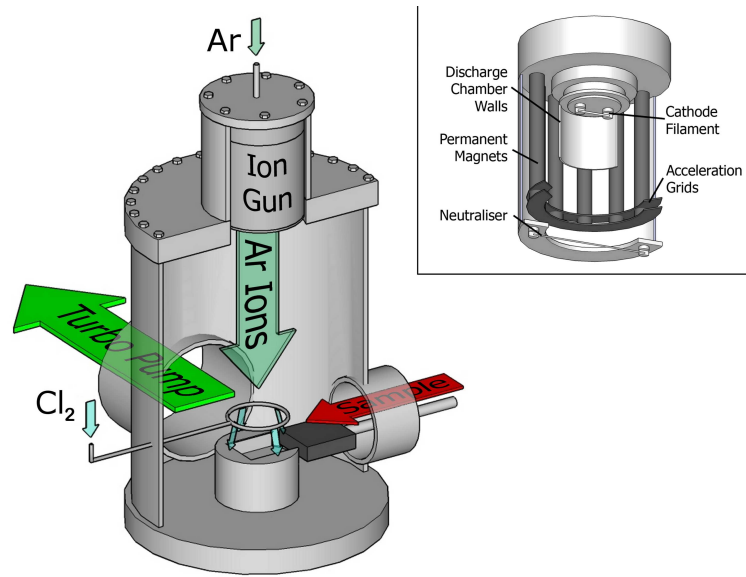


Figure 3.6: Cut away illustration of CAIBE etching system, inset shows cut away of ion beam gun.

sample at 5000 rpm for 1 minute and baked (95 °C, 1 minute) to drive the solvents from the resist. The sample is then exposed, using a photomask, for 60 seconds and developed until the pattern is clear (typically this takes 30–60 seconds). The resist pattern is then used as the dry etch mask, to produce 6 μm tall mesas.

3.6.1 Etching

The mesa is etched using chemically assisted ion beam etching (CAIBE) technology (figure 3.6). This process uses argon, which is ionised and accelerated towards the sample (using the acceleration grids within the ion gun). The Ar^+ ions impinge on the sample's surface and the impact removes material — this is known as physical etching. The process also uses a supply of chlorine gas (injected through a ring positioned above the sample stage) which reacts with the sample. This chlorine is responsible for the chemical component of the etching process. Using CAIBE, the mesas can be etched to a depth of 6 μm (i.e. through the active region of the VCSEL material), see figure 3.7.

Recipe Development

CAIBE is a combination of both physical and chemical processes. The physical component is controlled by the ion-beam parameters. These are the beam voltage (the

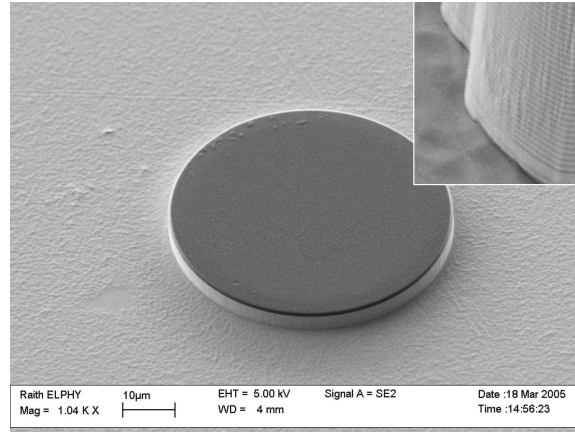


Figure 3.7: SEM image of etched mesa with resist etch mask (the mesas stand $6\ \mu\text{m}$ tall). The inset shows the active region at the bottom of the mesa.

voltage that accelerates the argon ions toward the sample) and the beam current (effectively the number of ions created per second) that can be controlled separately. One of the advantages of CAIBE over other etching methods (i.e. reactive ion etching (RIE)) is that the chemical and physical parameters can be controlled independently. The chemical etching is controlled by altering the flow of chlorine and the temperature of the sample. The higher the chlorine flow, the faster the etch, similarly, the higher the temperature of the sample, the quicker the chemical reaction can occur, speeding up etch rates.

In order to etch to a depth of $6\ \mu\text{m}$, it is necessary to have a high physical etch rate — so the beam voltage is set to 1450 V, and the beam current to 35 mA (the maximum possible). The physical etching alone is extremely low (10s nm/min — this is known as ion milling). Therefore, the chemical etch rate is increased by introducing chlorine. This results in far higher etch rates, but can result in undercutting through the increased isotropic etch rate. A sample temperature of $120\ ^\circ\text{C}$ and a chlorine flow of 3.5 sccm (standard cubic centimeters per minute) were empirically determined as the best parameters.

3.6.2 Cleaning

After etching, the original mask is removed. Since the next step involves baking at $450\ ^\circ\text{C}$ during the oxidation process any remaining photo-resist would be hardbaked, making it extremely difficult to remove. There are two methods for cleaning. First, the sample is placed in acetone (depending on the structure ultrasonic agitation can also be used), then rinsed in IPA. If this is not successful, specific resist-strippers can also be used, such as Shipley's SVC-14 positive photo-resist stripper. Secondly, the

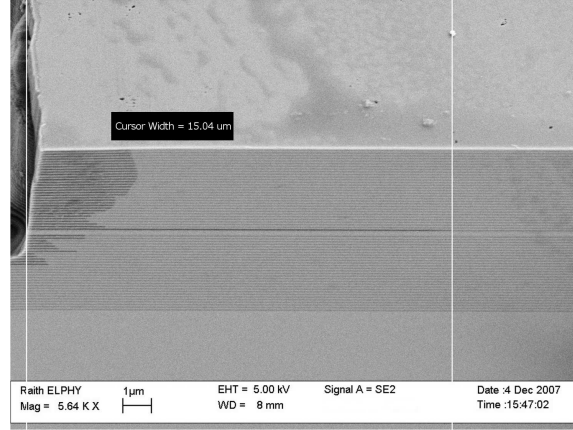


Figure 3.8: SEM image showing VCSEL cross-section, oxidised layers can be seen as the darker lines within the DBR stack.

sample can be placed in an oxygen plasma, using the Reactive Ion Etching (RIE) machine. This physically etches the remaining resist and cleans the sample. The RIE approach is used as a last resort, as exposing the $GaAs$ to an etch can damage the surface. However, leaving hard-baked photo-resist is deemed worse.

3.6.3 Oxidation

After mesa etching, the devices are oxidised to form the current aperture. The sample is placed in an oxidation oven, and heated in a steam atmosphere. The steam is created by bubbling nitrogen through a reservoir of water. This oxidises the high aluminium content layer within the VCSEL material and creates an aperture just above the active region of the laser (figure 3.8).

There are two oxidation regimes [33]: reactant limited, and diffusion limited. Reactant limited oxidation occurs first (while the amount of oxide is low). This regime is linear with time. Diffusion limited oxidation, which happens once a certain level of oxide exists, follows a parabolic relationship with time. The rate of oxidation is therefore seen to change with time (figure 3.9).

Nikel [35], looked at the oxidation kinetics of $Al_xGa_{1-x}As$ layers. The study looked at the vertical oxidation rate, from an open surface window. Two of his results are interesting with respect to my work. It was found that at fixed aluminium concentrations the oxidation rate followed an increasing exponential relationship (figure 3.10a). It was also found that the oxidation rate increased very strongly with aluminium concentration (figure 3.10b); Nickel investigated concentrations up to 78%. My material uses a concentration of 98%, therefore I expect a very much higher oxi-

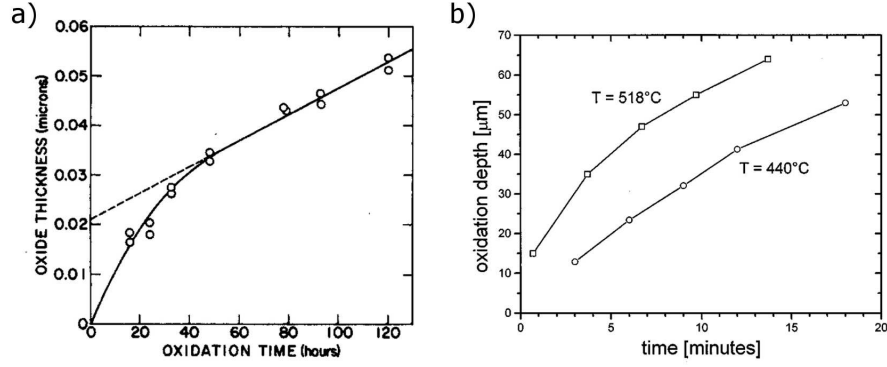


Figure 3.9: Graphs showing oxidation-rate saturation of a) silicon (taken from [33]) and b) aluminium arsenide (taken from [34]).

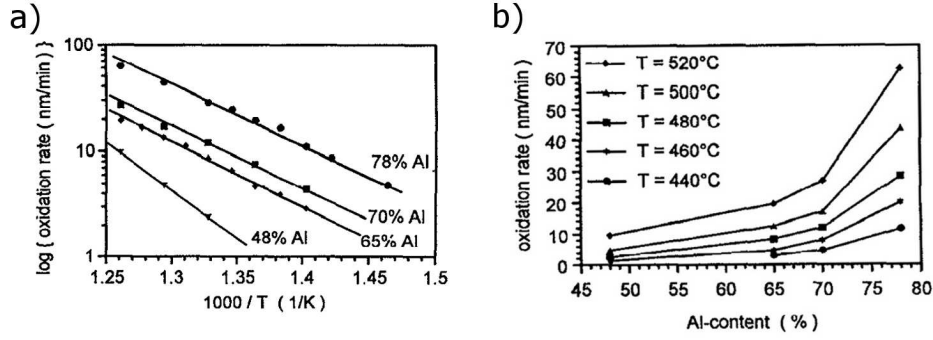


Figure 3.10: Graphs showing oxidation-rate dependence on a) temperature and b) aluminium concentration (taken from [35]).

dation rate. As mentioned, Nikel's experiment was for vertical oxidation not lateral, so I expect my results to vary. These results are therefore only used as a starting point for my own work.

Taking these points into consideration, initial oxidation measurements (described below) are only used as indications of the final oxidation rate.

3.6.4 Oxidation Results

Control over the oxidation process is paramount to controlling the VCSEL aperture size. The oxidation process is controlled by keeping the oxidation parameters constant (i.e. oxidation temperature, nitrogen flow, water-bath temperature), while varying the oxidation time. In order to measure the resulting aperture, I have used a number of techniques.

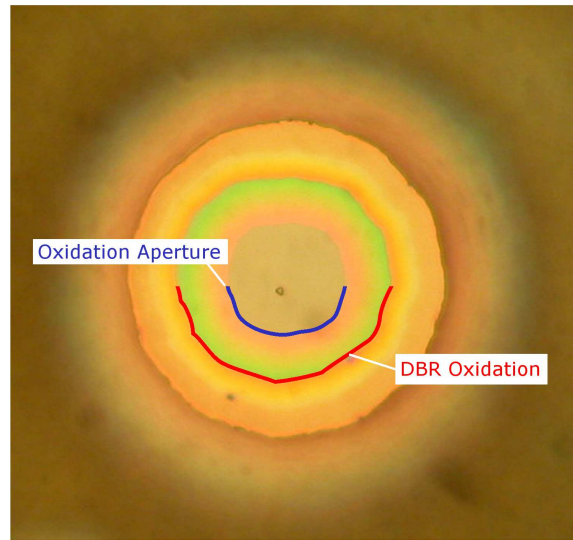


Figure 3.11: Optical microscope image of a VCSEL after oxidation, the evident ring (highlighted in blue) within the mesa indicates the extent of oxidation. During oxidation the top DBR partially oxidises (highlighted in red), therefore the extent of the actual oxidation aperture is more difficult to determine.

a) Direct Imaging

It is possible to observe a difference between an un-oxidised sample and an oxidised one under a microscope. Oxidation of the DBR material is slower than the oxidation at the aperture layer because of the lower aluminium concentration and so this oxidation is more evident in observation (see figure 3.11). As an extension to this technique, I etched the sample a second time to remove most of the top DBR. This gives a better view of the oxidation layer and resulting aperture. This technique is destructive and not as accurate as cleave tests (see figure 3.12).

b) Cleave Tests

After oxidation the sample can be cleaved in order to expose the oxidation front for examination by SEM. This process works well with a low error in measurement. Naturally, this technique is destructive, so sacrificial samples are fabricated (see figure 3.8).

c) On-chip Reference Tests

By placing a number of reference structures of differing size on the same chip, the presence (or lack) of light emission, can be used to infer the extent of oxidation. This technique is non-invasive and probes the real function of the device, rather

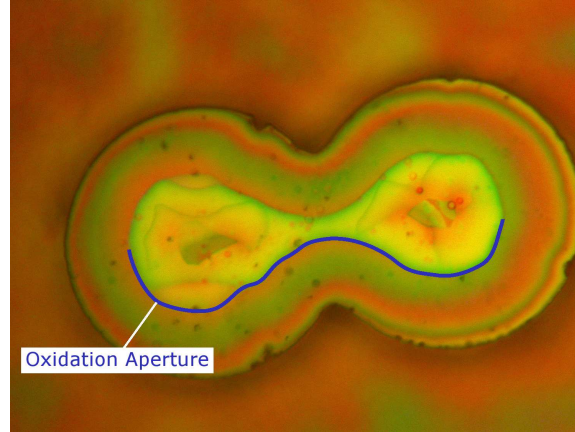


Figure 3.12: Optical microscope image of VCSEL after oxidation and second etch (i.e. removal of the majority of the top DBR), the extent of oxidation (highlighted in blue) is more easily determined than in figure 3.11.

than its structure alone.

Oxidation Conditions

A sample temperature of 450 °C, a water bath temperature of 80 °C, and a nitrogen flow of 400 sccm was chosen as the initial oxidation conditions. By keeping the oxidation parameters constant and adjusting the oxidation time, a time of 20–25 minutes was determined for approximately 20 μm of oxidation, resulting in both single- and multi-mode VCSELs. Single mode are desirable, and result from oxide apertures smaller than approximately 5 μm . The high-aluminium concentration and small thickness (i.e. 30 nm) of the oxide layer make reproducibly fabricating an oxide aperture of less than 5 μm difficult [36].

3.7 Insulation

The final step in fabricating a VCSEL is to provide an electrical insulation layer, which enables the use of wire-bonding for packaging. A number of insulation techniques were investigated.

3.7.1 Silicon Nitride

Silicon nitride (Si_3N_4) can be deposited onto GaAs by evaporation or sputtering. The Si_3N_4 was evaporated by using an electron beam evaporator. Complete cover-

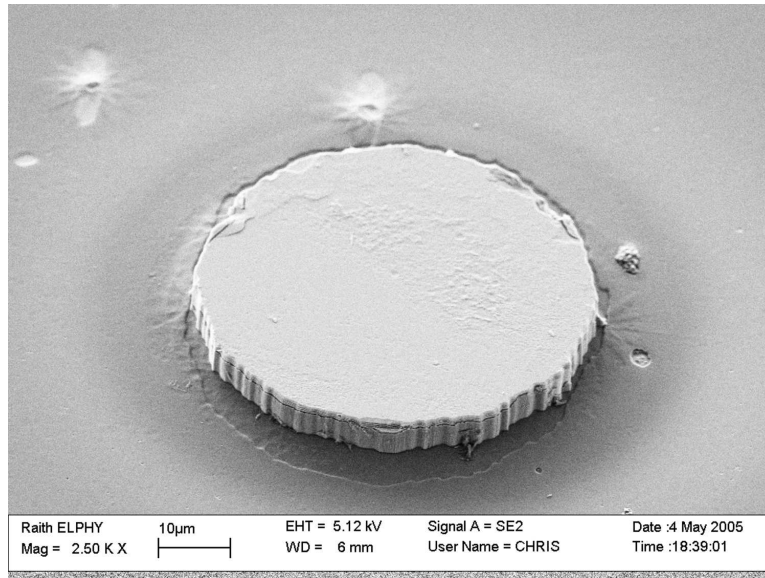


Figure 3.13: SEM image of Si_3N_4 insulation deposited by evaporation, the layer is very thin in the “shadow” of the VCSEL mesa.

age of the sample proved difficult, especially the step-coverage required across the 6 μm deep mesa. To cover the mesa sides the samples were mounted at an angle within the evaporator. The sample stage was also rotated during the process. This improved the layer marginally but the step-coverage problem was still evident, see figure 3.13.

The second technique was to sputter the material. Sputtering is less directional than evaporation, but the sputter rate in our system was too low (approximately 300 nm per hour). A problem of stress and of adhesion was also found when the Si_3N_4 layer was increased in thickness (see figure 3.14).

These problems might have been relieved if a planarisation layer was included in the VCSEL design. This layer would make the sample surface effectively flat, reducing the “shadowing” problem seen when evaporating. The planarisation layer could also increase the adhesion properties alleviating the sputtering issues. Therefore, planarisation layers were investigated.

3.7.2 Silicon Dioxide

In order to planarise the chip, silicon dioxide was investigated in the form of hydrogen silsesquioxane (HSQ). This is a spin-on glass available from Dow Corning as “flowable glass” (FOX-12). This insulating material is typically used in thin layers as etch masks. The HSQ is spun onto the VCSEL chip, in multiple layers to a thickness

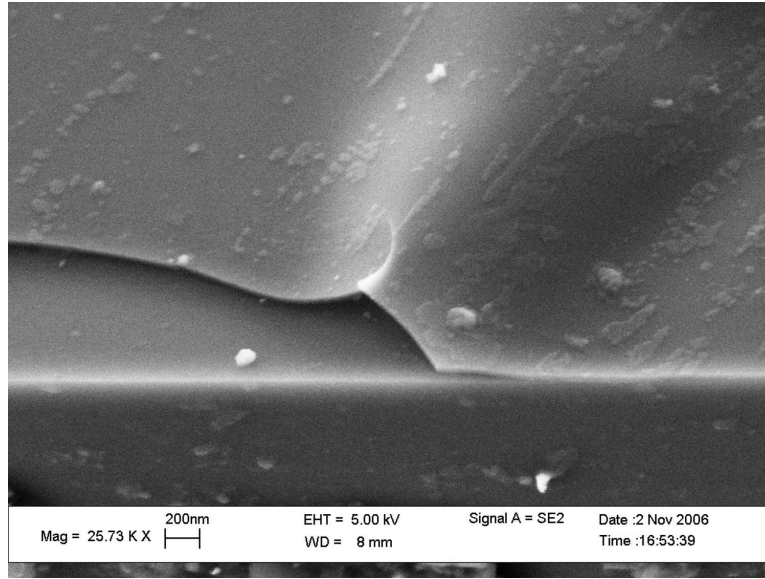


Figure 3.14: SEM image of Si_3N_4 insulation deposited by sputtering; delamination due to poor adhesion is visible.

of approximately $1\text{ }\mu\text{m}$ (sufficient to smooth, yet not planarise the VCSEL chip). It is then baked slowly raising the temperature from 100- to 400 °C over a number of hours. This cures the glass and transforms the film into silicon dioxide. Contact windows are then opened on the mesas, although this was difficult and etch times in excess of 40 minutes were necessary. This process, taking into account preparing the silica film and etching can take in excess of 6 hours, it was therefore superseded by the use of SU8 as a planarising polymer.

3.7.3 SU8

A different way to both insulate and planarise the VCSELs in a simple step is to use a polymer such as SU8 (see figure 3.16). Two approaches for using this polymer were available. The first was to spin a layer of SU8 over the sample, of the same thickness as the VCSEL mesas (i.e. between 5 and $6\text{ }\mu\text{m}$). SU8 can be far thicker than FOx-12, as such this approach is preferred. This coating leaves a minimal amount of SU8 on top of the mesa, which can be removed in an oxygen plasma. This approach is simple and worked well. However, spinning SU8 reliably is difficult and a number of variables can effect the final thickness of the layer. The main problem is that the SU8 is a mixture of both SU8 2000.5 (extremely thin) and SU8 2050 (extremely thick) in order to reach the desired thickness. By mixing these two polymers a mixture of the correct viscosity can be obtained. Unfortunately, slight variations in composition yield significant differences in film thickness which made reproducible results difficult to achieve. The temperature of the SU8 at the time of

spinning must also be kept constant, along with the humidity of the local environment. Working in a cleanroom, these two factors were not a problem. However, a change in insulation thickness was still observed.

In the second method, I used SU8 as a resist (e-beam or photo-). After spinning a layer, the resist is exposed. SU8 is very sensitive to e-beam exposure and the resolution required for insulation is low, so large areas can be written, using high e-beam currents and short exposure times. Typical contact pad sizes are 200 by 200 μm .

The SU8 layer can also be exposed using photolithography. The resolution in this case is lower than by e-beam exposure, but this is not a problem. Alignment of the contact window is more difficult, but can be achieved with good reproducibility. This exposure technique is superior to etch-back because almost any thickness of SU8 can be exposed to create both the insulation layer and contact window (see figure 3.15). It is also possible to thin the initial layer of SU8. This is sometimes necessary to ensure that the contact windows are not too deep (if the window is too deep the electrical contact may not cover the step). This thinning is not as critical as the above process.

The SU8 insulation and planarisation process was adopted for the rest of this work, due to its speed and reproducibility.

3.8 Contacting

The final step in fabricating a VCSEL is that of depositing electrical contacts as described before.

3.9 Fabricated VCSEL Characterisation

The VCSELs made using the above processes were to be used as a test-bed for beam controlling mechanisms. Therefore it is important to build reliable, reproducible devices. This was achieved. Figure 3.17, shows the light-current-voltage (L-I-V) graph of a fabricated VCSEL (this VCSEL has a small oxide aperture evidenced by its low threshold current). The VCSEL emits greater than 2 mW of continuous wave (CW) light (figure 3.17a), at 980 nm. The VCSEL has a low threshold, of below 500 μA (figure 3.17b). Figure 3.18, taken by coupling the VCSEL emission into an Ando AQ6317B Optical Spectrum Analyser, shows the emission spectrum of another typical VCSEL (this VCSEL had a larger oxide aperture resulting in a threshold of ap-

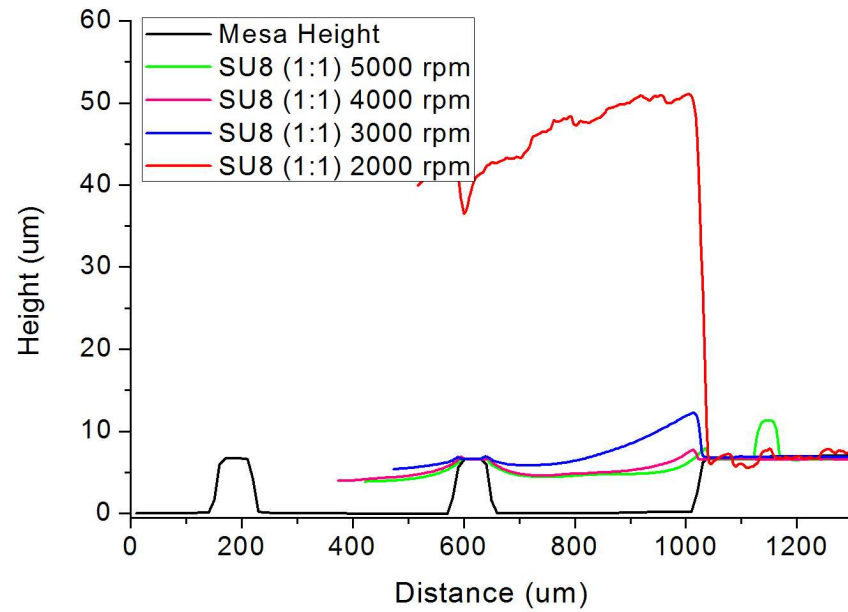


Figure 3.15: Graph showing resulting SU8 (1:1 mixture of SU8 2000.5 and SU8 2050) thicknesses, after the photolithography process, for different spin parameters.

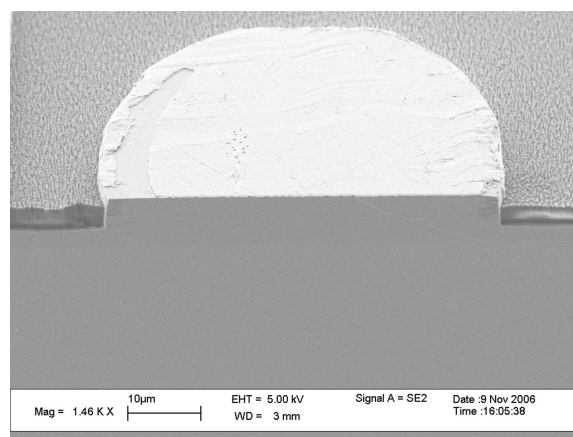


Figure 3.16: SEM image of VCSEL mesa with SU8 insulation, insulation can be seen to cover the active region.

proximately 4 mA). VCSELs with larger apertures, built during this project, tend to begin single mode just above laser threshold and become multi-modal quickly at less than $2I_{th}$. The VCSEL emission line shifts, to longer wavelengths, by approximately 1 nm every 10 mA of drive current (figure 3.20). This is due to thermal affects within the VCSEL structure [30]. Figure 3.21 shows a number of emission lobes taken from a single VCSEL (with threshold approximately 3 mA), as the drive current is increased the emission lobe changes, primarily due to spatial hole burning. Spatial hole burning is a process by which areas of the gain region become saturated, which limits the available amplification at that point. The resulting emission lobe of the laser changes to reflect the local gain across the emitting aperture.

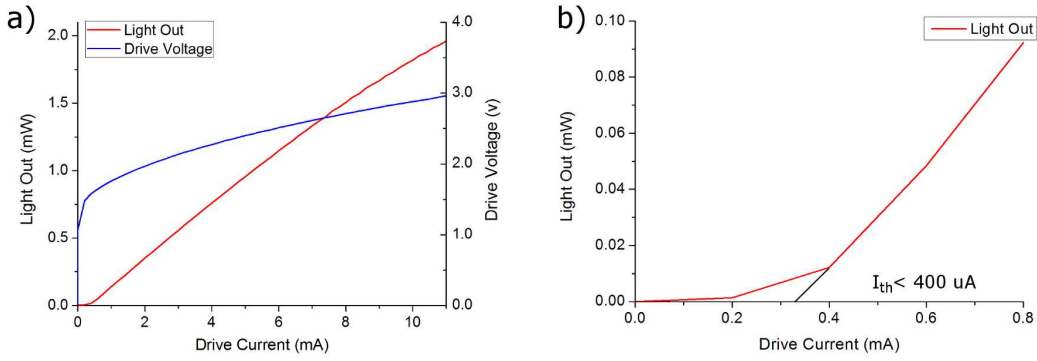


Figure 3.17: a) Typical VCSEL L-I-V graph and b) Sub-milliamper threshold (less than 400 μA) achieved with same VCSEL.

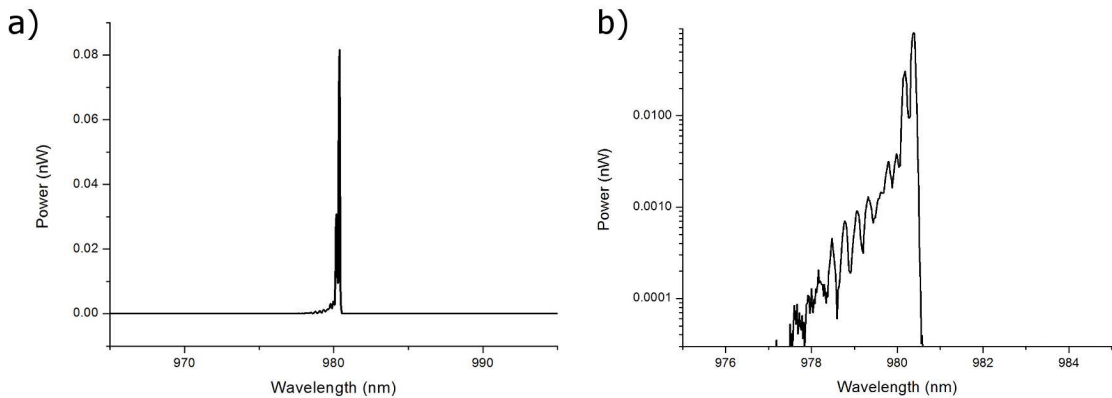


Figure 3.18: VCSEL emission spectrum, taken just above laser threshold (at 5 mA drive current), a) showing plot on a linear scale; b) the same plot with a logarithmic scale).

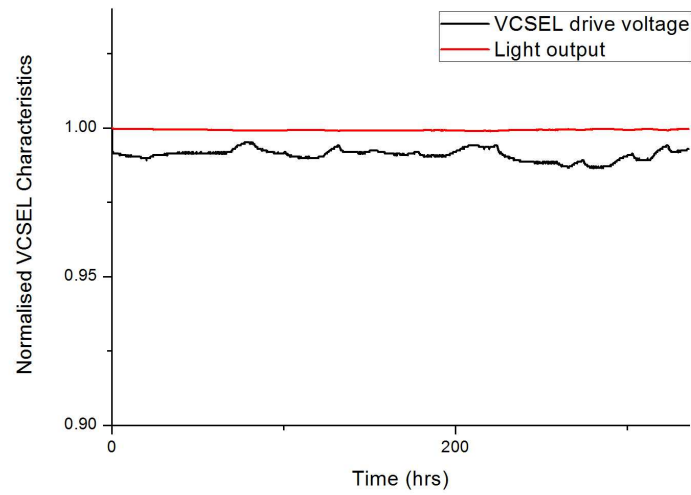


Figure 3.19: Non-accelerated lifetime results for a typical VCSEL. After 14 days the VCSEL output has only varied by 0.1%.

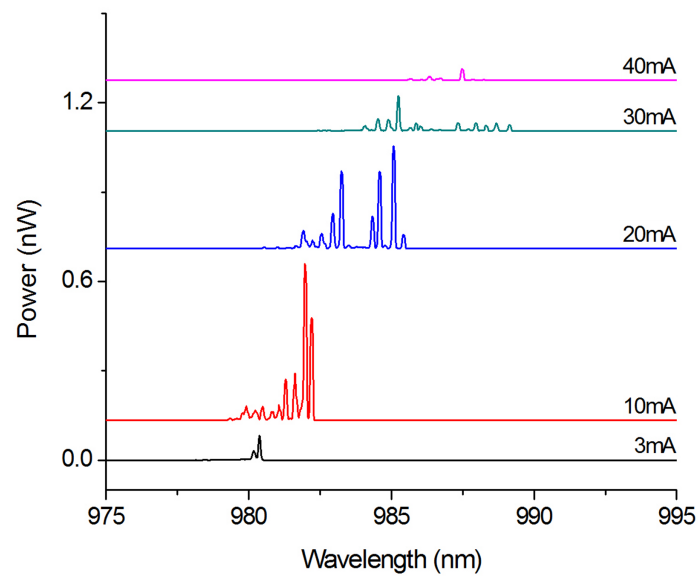


Figure 3.20: Graph showing spectral evolution of a typical VCSEL as the drive current is increased.

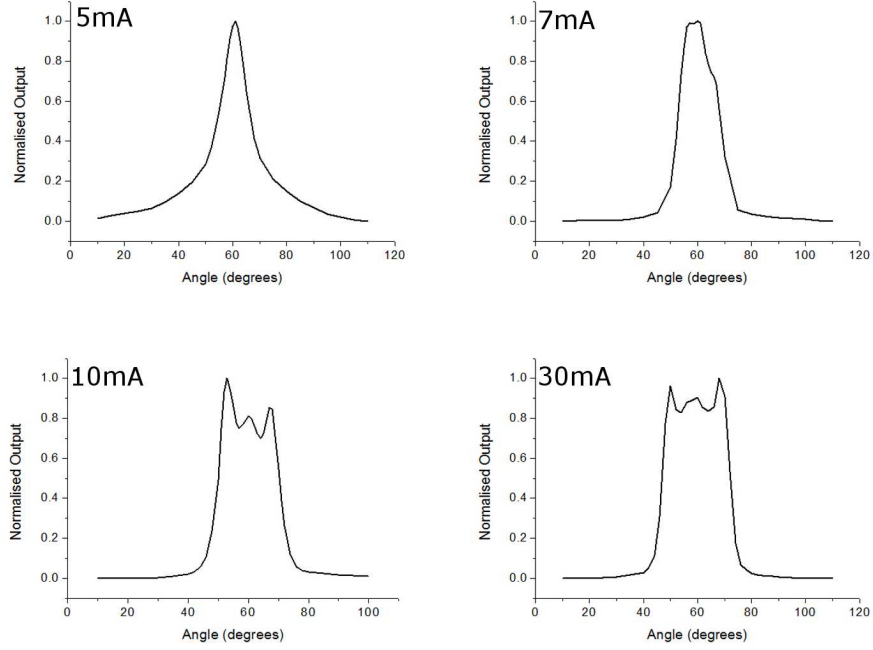


Figure 3.21: Graphs showing VCSEL emission lobes as drive current is increased.

3.10 Conclusions

This chapter introduced the design and fabrication of VCSELs for the SpeckNet project. During development of the VCSEL a number of challenges were overcome. These included designing an etching protocol that resulted in reproducible etch rates — this was accomplished with CAIBE technology. Insulating the devices, to aid in packaging final systems was also investigated. A number of insulation processes were looked at including evaporation of silicon nitride — step-coverage problems in the resulting film prevented the use of this technique. Sputtering of silicon nitride was also tried — sputtering rates were too low to make this a viable option, along with adhesion and film stability issues. Spin on glass (HSQ) was looked at, but process constraints and the etching of contact windows prevented this process from being adopted. Finally planarisation and insulation by use of SU8 was investigated. This is the best method and was used in fabricating the final devices. The process made use of photolithography to open contact windows within the polymer which is reliable and reproducible.

Chapter 4

Micro-lenses for Static Beam Control

4.1 Introduction

The aim of this chapter is to develop a mechanism by which beam conditioning, initially in the form of steering can be performed. The mechanism developed in this chapter is that of the microprism fabricated using greyscale lithography. This steering technique uses an array of multiple emitters, each source directed into a different volume of space. By employing an array structure on-chip testing throughout the fabrication process is also possible increasing the reproducibility of the devices. Dynamic steering with this technique is achieved by “turning-on” the different emitters. Therefore, this steering can be thought of as discrete, as such each emitter will be designed to have a divergence angle great enough to cover the communication volume between its two closest neighbours. This chapter will outline the methods I developed to fabricate such arrays an illustration of the proposed system is presented in figure 4.1.

Beam conditioning, in general refers to a number of properties that one wants to control, in particular beam divergence, direction and polarisation. Controlling beam divergence is useful, as it gives the ability to tailor vertical-cavity surface-emitting laser (VCSEL) outputs for use in multiple emitter systems, as outlined above. For example, increasing the divergence maybe useful such that fewer VCSELs are needed to cover a given communication volume (i.e. if each VCSEL emitted into a 20° half-angle then using only four VCSELs having their optical axes set at 45° to each other would cover 180° of field, whereas having VCSELs with only a 10° half-angle would require nine VCSELs. On the other hand, if the optical system is used as a supplement to the radio, used for long-haul point-to-point communication within the network, then limiting the divergence of the VCSEL is required in order to focus

the beam. Most of the energy emitted can then be directed to the receiving Speck, which affords more energy efficient devices or longer communication distances.

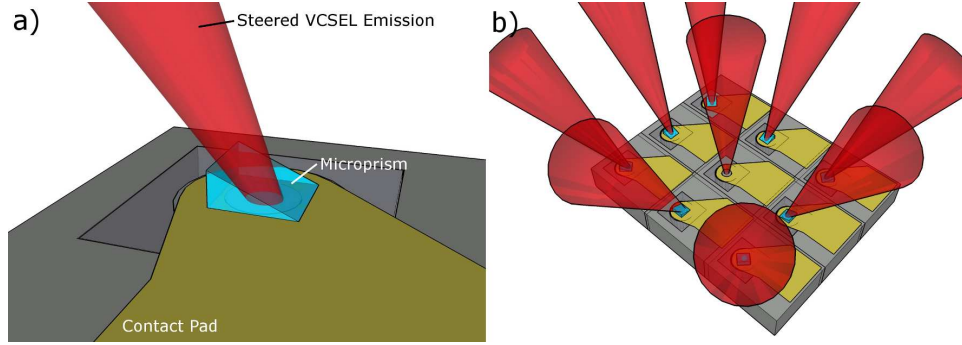


Figure 4.1: Illustration of intended microprism steering mechanism, using multiple emitters to access multiple directions.

4.2 SU8 Optical Elements

The first option I investigated was to use the polymer SU8. SU8 is a negative resist, i.e. the areas of the resist that are exposed (in this case using an electron beam lithography (EBL) system) become cross-linked. Once the sample is developed, the exposed areas remain while the other areas are washed away. A post exposure bake (PEB) completes the cross-linking process (figure 4.2 (taken from [37])). As the PEB temperature is increased, more of the exposed film is cross-linked resulting in lower doses producing the same thickness of SU8 after development.

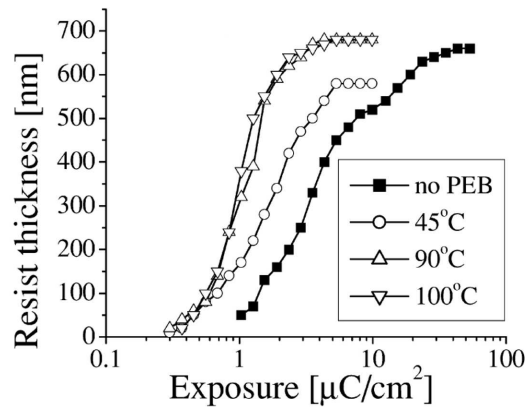


Figure 4.2: Graph taken from [37], showing change in resulting SU8 polymer thickness against electron-beam dose according to post exposure bake (PEB) parameters.

4.3 SU8 Exposure

The mechanism responsible for the electron beam exposure of SU8 is back-scattered electrons. The forward travelling electrons, direct from the column, are too energetic and mainly pass through the polymer film. However, once these electrons impact the substrate material they lose energy and some are reflected back. It is these electrons that cause the cross-linking effect. This is an important point. If it was the forward travelling electrons that caused exposure then the top of the film would cross-link first — altering the dose of the electrons would then mean that the top of the film would be exposed while the bottom part is not, as such during development the pattern would lift away from the substrate. Due to the back-scattered-electron exposure, it is the bottom of the film that is exposed first, as such the features remain attached during development. On the other hand, the penetration depth is determined by the acceleration voltage used during exposure, which limits the film thickness. If the film is too thick the electrons do not penetrate to the bottom of the film resulting in developed patterns lifting off.

In order to test the use of SU8 as a greyscale resist material I began by using glass as the lens substrate. I chose to begin with glass as it is a cheap and widely available substrate. I began by performing a number of dose tests. The backscatter coefficient of glass differs from *GaAs* (the target material) as such these dose tests are repeated using a *GaAs* substrate at a later stage.

4.3.1 Low/High Dose Test

To establish the useful dose range within the greyscale region, I designed a pattern of (10 x 10) 50 μm squares. Each square was given a different dose and after exposing and developing, the resulting squares of SU8 were examined. The low dose for the greyscale process was then chosen according to the first developed box and the high dose accordingly. This narrowed the dose range and a further higher resolution dose test (i.e. smaller dose steps) was performed. The resulting film thicknesses were measured by mounting each dose test in a scanning electron microscope (SEM) at an angle of 45 degrees to the column. By using the SEM to measure the film the results should have been extremely accurate (i.e. nanometer resolution). However, due to the sample being mounted at an angle and the higher doses not resulting in perfectly square features (see below) the accuracy decreased. With this said, the error, over the range of interest, is still well below 1 μm and a clear trend can be observed (see figure 4.4).

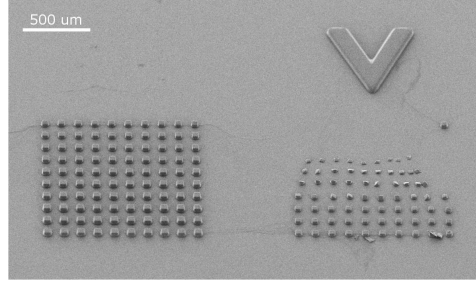


Figure 4.3: SEM image of two consecutive dose test patterns. An alignment mark, pointing to lowest dose region, is visible in the top right of the image.

4.3.2 Dose and Resulting Film Thickness Characterisations

From the results (figure 4.4), a clear linear region of dose against film thickness can be seen between the doses of $0.2 \mu\text{As}/\text{cm}^2$ and $0.8 \mu\text{As}/\text{cm}^2$. This yields a useful thickness range of approximately $5 \mu\text{m}$. It can also be seen that the film thickness saturates — this limits the height of the eventual element to below the maximum film thickness of $12 \mu\text{m}$. However, keeping the optical element slightly thinner than this height is beneficial as the resulting thicknesses at slightly lower doses are more predictable. To increase the thickness of the elements, it is necessary to increase the thickness of the initial SU8 film. This is not possible with our electron beam lithography (EBL) system because of the penetration depth of the impinging electrons already mentioned above. Our electron beam system uses an acceleration voltage of 30 kV. The higher this voltage, the thicker the film of SU8 that can be fully exposed. I confirmed the data from [38], which states that 30 kV allows electron penetration of the order of $10\text{--}12 \mu\text{m}$. When I used thicker films they peeled off, because the electrons did not penetrate the film and expose the bottom of the SU8. To increase this depth further I would have to work with a larger EBL system — this is possible, but was not carried out within the scope of this work.

4.3.3 Proximity Effect

Another feature, shown in figure 4.5, is that the size of the resulting SU8 boxes increases as the EBL dose is increased. This is due to what is known as proximity effect. Proximity effect comes from the fact that the charge due to the electron exposure spreads away from its intended position, which is more evident when the dose is high (i.e. the electrons are fired at one spot for longer). In simple designs, as in the dose tests, this results in areas within patterns getting larger and the edges of patterns becoming less well defined. In complex patterns, however, such as those for constructing lenses or prisms, areas with high doses effect the dose of neighbouring areas (hence the name proximity effect). This effect can be compensated for, but

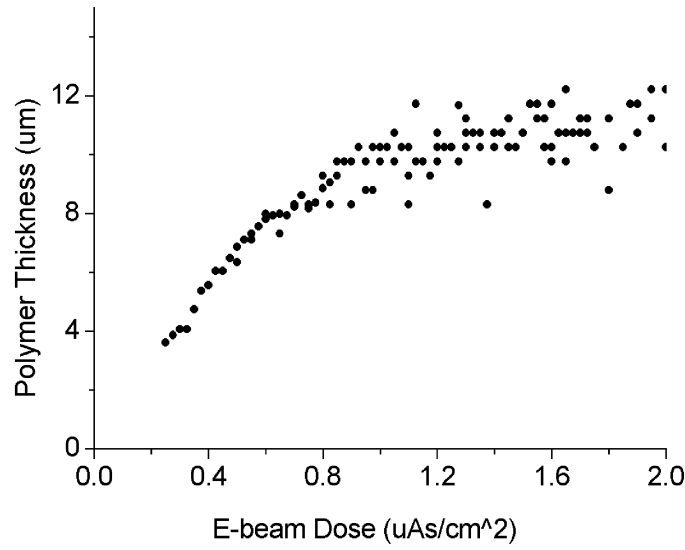


Figure 4.4: Graph showing resulting polymer thickness against electron-beam dose, greyscale lithography exploits the linear region between the doses of $0.2 \mu\text{As}/\text{cm}^2$ and $0.8 \mu\text{As}/\text{cm}^2$.

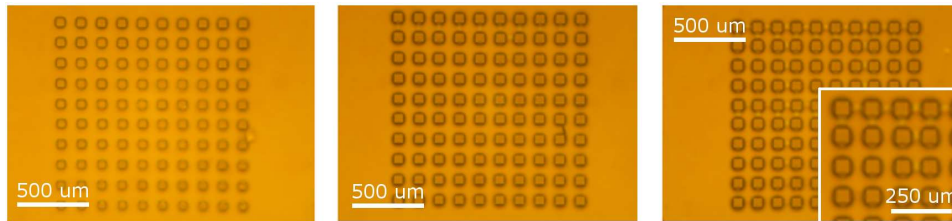


Figure 4.5: Microscope images of three dose test patterns, proximity effect is clear. Boxes increase in size from left (low dose) to right (high dose) of the pattern, inset shows high dose patterns starting to merge.

the process is very time consuming and results in very large and more complex, patterns¹. I found that non-proximity corrected patterns were as fit for purpose as corrected ones, so did not tend to use proximity correction.

¹The proximity correction process takes the large areas within the pattern and divides them into smaller areas it then alters the dose of each area, according to an algorithm, in order to balance out the proximity effect across the whole pattern. The patterns required for optical elements are relatively large (covering towards $50 \times 50 \mu\text{m}$) as such performing proximity correction becomes prohibitively processor-time consuming, the resulting patterns are also very large and hence processor and memory intensive to work with.

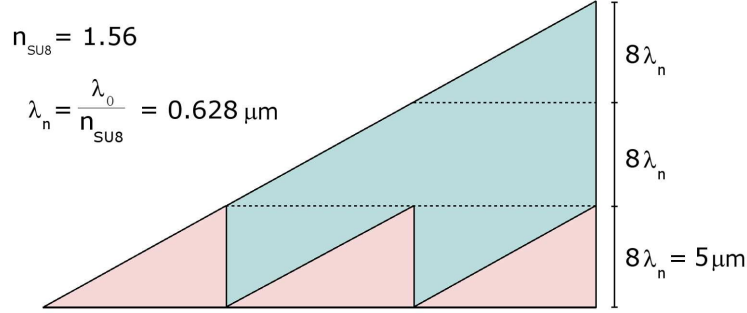


Figure 4.6: Illustration of Fresnel prism design, the prism is shortened by an integer-multiple of λ_{SU8} , i.e. $5 \mu\text{m}$.

4.3.4 Fresnel Prism Design and Fabrication

To achieve larger angles, I considered the idea of the Fresnel lens² applied to my prisms. I took this method and applied it to my own optical elements by removing approximately $5 \mu\text{m}$ of material from the back plane of the prism ($5 \mu\text{m}$ corresponding to approximately $8\lambda_n$, where λ_n , the wavelength of VCSEL emission in the SU8 material, is 628 nm) so that the new Fresnel prism would fit within the constraints of the SU8 film and dose window (figure 4.6). This approach resulted in good looking prisms, but due mainly to proximity effect and the non-linear transfer function of resulting film thickness with exposure dose (figure 4.4) did not produce prisms that worked as required, see figure 4.8b which shows a laser far-field after passing through a Fresnel prism. The prism tends to act as a diffraction grating although more light can be seen in the positive-first order than its negative counterpart. A perfect Fresnel grayscale prism requires a step from a very high dose (as high as the process will allow) to a low dose (the lowest the process allows) in a very small distance (instantaneously would be ideal). This is not possible, however the high dose effects the low dose to some extent tending to “round-off” the feature’s edges (see figure 4.8a).

²Fresnel lenses (originally designed for lighthouses) are thinned by removing very precise sections of the lens. It was Fresnel that looked at this problem originally and saw that it is not the thickness of the lens that the light travels through that matters, but the interface between the lens and the surrounding medium. This is not entirely true, for a lens to image properly the light must reach the focal point of the lens in phase, as such Fresnel knowing that light comes in and out of phase every 2π radians, removed thicknesses of material, from the back plane of the lens, equal to the distance travelled by the light over 2π radians. This reduced the thickness of the lenses substantially and allowed very large lenses to be constructed.

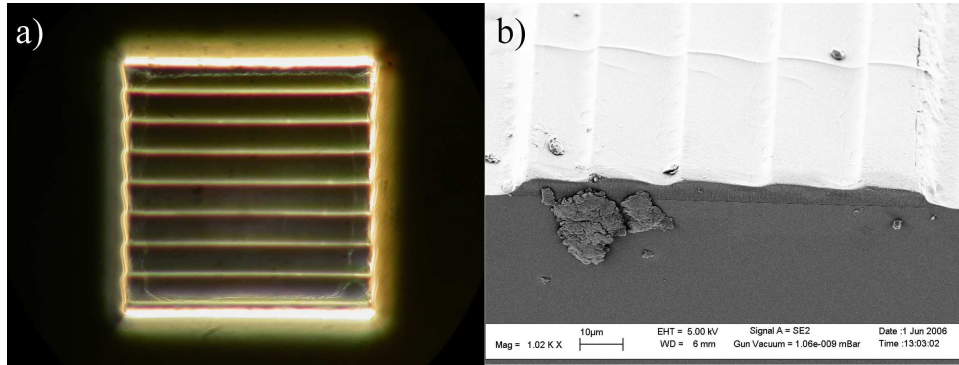


Figure 4.7: a) Dark field microscope photograph, showing Fresnel prism. b) SEM image of cleaved Fresnel prism.

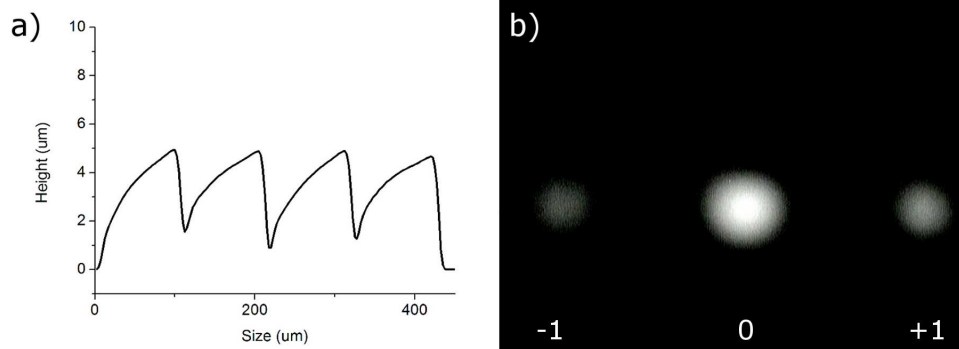


Figure 4.8: a) Graph showing profile of Fresnel prism. “Rounding-off” due to proximity effects, is evident at the large changes in film thickness. b) Laser far-field intensity distribution, after passing through a Fresnel prism. Poor selectivity between the emitted orders (labeled within image) indicates that the phase conditions of the Fresnel prism were not met, if these conditions had been met most, if not all, the light would be emitted into the positive-first order.

4.3.5 Local Thermal Reflow

In previous work [39], the technique of thermal reflow had been used to create spherical microlenses. This was accomplished by spinning a layer of polymer and then exposing and developing a pattern of, for example cylinders, each with a similar height to the required lens. These cylinders were then baked at the glass transition temperature (the temperature at which a polymer becomes soft on heating or brittle on cooling) for a number of hours. This causes the polymer to reflow, and due to its surface tension, form microlenses.

I also investigated this technique. I spun a layer of SU8 of approximately $8\text{ }\mu\text{m}$ thickness. This layer was then baked for 6 minutes (3 minutes at $65\text{ }^{\circ}\text{C}$ and 3 minutes at $95\text{ }^{\circ}\text{C}$). The sample was then optically exposed to create an array of cylinders. These were baked a second time and developed. Once the sample was complete, it was baked at a high reflow temperature of $285\text{ }^{\circ}\text{C}$ for 1 hour. After this reflow bake I noticed that the cylinders had gone brown and that no large scale reflow had occurred. I repeated the experiment at a lower temperature of $250\text{ }^{\circ}\text{C}$ in an inert atmosphere of nitrogen for an extended time of 2 hours. The cylinders still turned brown and still no large scale reflow occurred. The reflow technique is therefore not appropriate for my purpose. I noticed a change in surface roughness, however, so I looked at this more closely.

As part of the standard SU8 recipe, the sample is baked at $180\text{ }^{\circ}\text{C}$ for 10 minutes which is usually done to increase the robustness of the film. Taking three identical samples, each with a selection of microprisms, I baked one at $100\text{ }^{\circ}\text{C}$, one at $200\text{ }^{\circ}\text{C}$ (usual hard-baking takes place at $180\text{ }^{\circ}\text{C}$) and left the third sample un-baked. Using the DekTak surface profiler, I measured the roughness of some prisms on each sample. Figure 4.9 shows three typical traces. The un-baked sample shows a standard deviation of 14.9 nm over the scan length of $5\text{ }\mu\text{m}$, while the sample baked at $100\text{ }^{\circ}\text{C}$ shows a reduction to 7.7 nm and the sample baked at $200\text{ }^{\circ}\text{C}$ shows a further reduction to 4.0 nm . Baking the samples at higher temperatures will cause the microprisms to turn brown. As such, baking at $180\text{ }^{\circ}\text{C}$, as usual, seems to be the best procedure.

4.4 Greyscale Microprism Results

Due to the problems encountered during Fresnel prism fabrication, I decided to use single-angle prisms and integrate them on real VCSEL devices. In order to maximise the possible prism angle on an actual VCSEL, I fabricated a number of microprisms

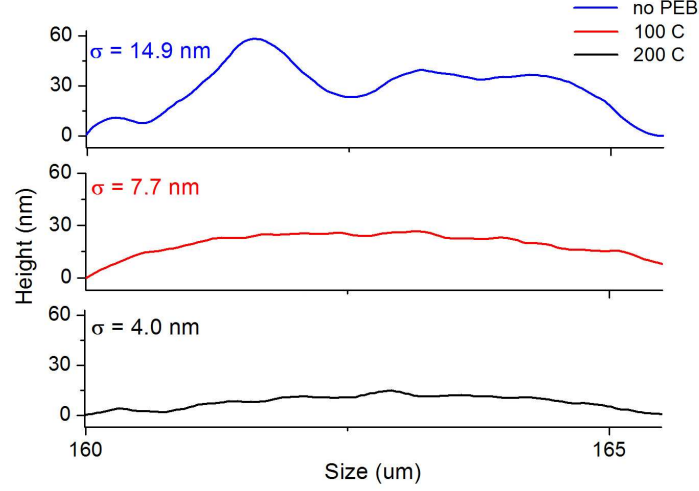


Figure 4.9: Three graphs showing the surface roughness of three typical microprisms each baked at a different temperature.

each with different lateral dimensions. By decreasing the lateral dimension of the prism, while keeping its height constant, the overall prism angle is increased. Figure 4.10a shows three prism profiles measured using a surface profiler, each having a different lateral dimension. Prism angles of $\alpha_1 = 5.2^\circ$, $\alpha_2 = 10.3^\circ$ and $\alpha_3 = 10.2^\circ$ for a 50-, 30- and 20- μm prism respectively, are shown. The usable area of each prism is also indicated in figure 4.10, which I have defined to be between the points at which the angle of the prism changes by 10%. This useful area decreases as the angle of the prism increases which is mainly due to the topology of the VCSEL chip.

The prisms are fabricated on the emitting surface of top emitting VCSELs. This

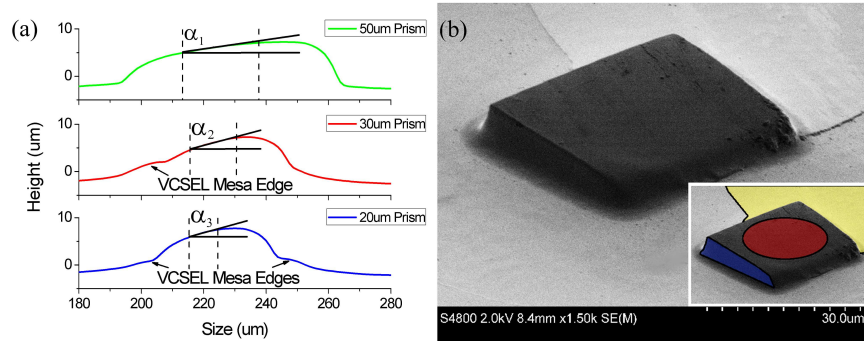


Figure 4.10: a) Surface profiles of three VCSELs with integrated prisms of differing lateral dimension. b) SEM image of a microprism integrated VCSEL. Inset shows contact pad (yellow), location of VCSEL aperture (red) and microprism angle profile (blue).

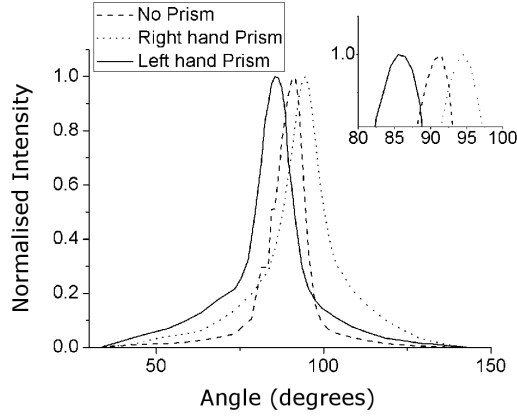


Figure 4.11: Emission lobe measurements of a microprism-steered VCSEL array. Inset shows a close-up of the steering angle achieved.

un-even surface clearly plays a role in the final shape of the microprism and causes the features to change from their desired shape (see figure 4.10a). I found that the $30\text{ }\mu\text{m}$ prism was best suited for the purpose as it provided both the largest prism angle and useable area. Figure 4.10b shows an SEM image of the completed VCSEL with microprism. The inset gives an indication of the important parts of the device, namely: the contact pad (yellow), used for wire-bonding and subsequent packaging of the final transceiver array; the VCSEL aperture (red), which needs to be completely covered in order for the prism to “steer” all of the emitted light; and the prism slope, highlighted in blue.

In order to test the completed VCSEL-prisms, I fabricated a (3×1) array of “steered” VCSELs. The emission lobe of each VCSEL was measured using a photo-detector mounted on an automatic rotation arm. The detector was held approximately 30 cm from the VCSEL chip and the output power read every 2 degrees. The data was then normalised to the maximum output and the results are shown in figure 4.11. The lobes of the two outer VCSELs are deflected by ± 5 degrees from normal (i.e. the central VCSEL emission). This is expected from the 10° prism angle made of SU8 (index of refraction $n = 1.56$). This figure also shows how the microprism does not adversely affect the quality of the emission lobe of the VCSEL since the central lobe is no different to the other deflected lobes that have passed through prisms. This good beam-shape highlights one of the advantages of using microprisms (or any refractive optic element (ROE)) over diffractive optic elements (DOEs). ROEs do not produce higher order lobes alongside the desired steered-lobe [40], and as such can be thought of as more efficient at “steering” light.

4.5 Conclusions

This chapter has introduced the idea of beam control using micro-optical-elements, in this case microprisms. I have described how the microprisms were designed and fabricated using the e-beam sensitive polymer SU8. In order to fabricate the largest prism angle and the largest “steering” angle possible, I looked at the use of Fresnel prisms. This technique did not work for my purpose. I adapted the initial design to use single-angle prisms instead. The single-angle prism has a lower prism angle than the Fresnel counterpart, and the maximum angle is limited by the EBL acceleration voltage. I used an EBL system with a maximum acceleration voltage of 30 kV, which allowed me to expose a maximum thickness of 10–12 μm of SU8. Increasing the acceleration voltage would increase this thickness [38]. Such scaling was not carried out but would be a possible extension to the process. Once a design and fabrication process had been put together and tested, I built a number of fully integrated “steered” VCSELs. I tested these VCSELs on a test rig, and demonstrated a steering angle of ± 5 degrees. In principle the angle could be increased using the technique outlined above. This approach to beam control is similar to previous work where micro-optical elements have been mounted onto finished laser arrays [41, 42], but here the prism is directly integrated with the laser, making the process simpler and in some aspects more versatile. Using this technique it is also possible to fabricate other interesting optical elements such as axicons and spiral-phase-plates [43], which is not possible with a technique such as complete large-scale thermal reflow which exploits the surface tension of polymers [39].

As mentioned the system described in this chapter creates a steering angle of 10 degrees (over the array), which would therefore require the use of over 30 such arrays to cover a 360 degree communication volume. Each individual array would have to be mounted at an angle of 10 degrees to each other around the Speck. However, with sensitive, well filtered detectors (discussed in chapter 8) the communication distance of such an array could surpass the 10 metre range (measurements within this chapter were taken at approximately 30 cm for convenience). Taking these points into account I believe this result can be seen as the first steps towards achieving an optical SpeckNet following the constraints laid out in chapter 2 (i.e. 10 emitters total; a steering angle of 30 degrees; and beam divergences of 25 degrees). Therefore both the steering angle of such an array would need to be increased (discussed below) and the divergence of the VCSELs, this can be achieved by tailoring the size of the initial mesa and oxide aperture.

In order to increase the “steering” angle of these microprisms, I looked at transferring the prisms into a material of higher refractive index. Such transfer being

achieved in other work [44, 45]. The VCSELs I fabricated have both a capping layer and substrate made of *GaAs* with an index, $n = 3.6$. Etching the prisms into this material would increase the steering angle approximately fivefold. In order to etch into *GaAs*, chlorine is used as an active gas. To etch through SU8, oxygen is used. Unfortunately, the equipment I had at my disposal, had these two gases in two different machines, so I was unable to attempt this transfer.

However, transferring the prisms into the *GaAs* would require one of two approaches. Firstly, increasing the VCSEL capping layer thickness to accommodate the prism — etching into the output mirror of the VCSEL would compromise the VCSELs performance. Or secondly, using bottom emitting VCSELs and etching the prism into the bottom surface of the substrate. This requires precise alignment of the VCSEL to the prism and would be difficult. As such, using a refractive optical element, direct-write integrated greyscale micropisms, I believe, is the best solution for beam steering. This work was published in [46].

Chapter 5

Integrated Diffraction Gratings for Static Beam Control

5.1 Introduction

As explored in the previous section, beam conditioning using integrated microprisms is a good solution. It is, however not the only solution. I have also looked at other techniques that employ gratings integrated directly onto the VCSEL devices (see figure 5.1). Gratings provide for a static means of steering, much like the previous microprism technique, as such multiple emitters would be employed in a final transmitter array, each emitter having a different emission angle. I will outline two approaches within this chapter. The first uses angled gratings (figure 5.1b and figure 5.2), the second will develop the grating approach further using similar principles to those of the microprism steering mechanism and employs sub-wavelength gratings (figure 5.1c).

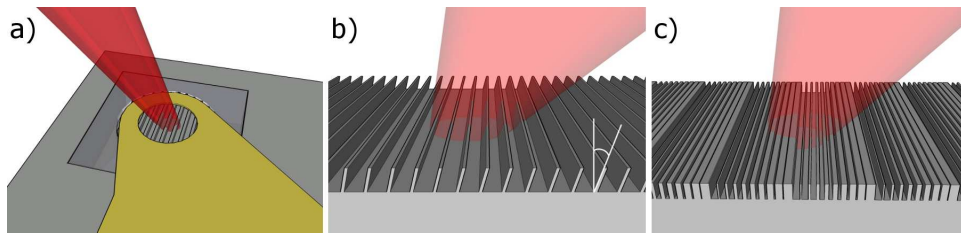


Figure 5.1: Illustration of intended grating steering mechanisms a) completed grating steered VCSEL, b) close-up of proposed angled grating technique and c) close-up of proposed sub-wavelength grating technique.

Therefore the idea is to create phase gratings by etching both macro- and wave-length scale periodic structures (i.e. gratings) into the semiconductor. Firstly, by “blazing” the grating, i.e. etching angled facets, most of the emitted light can be

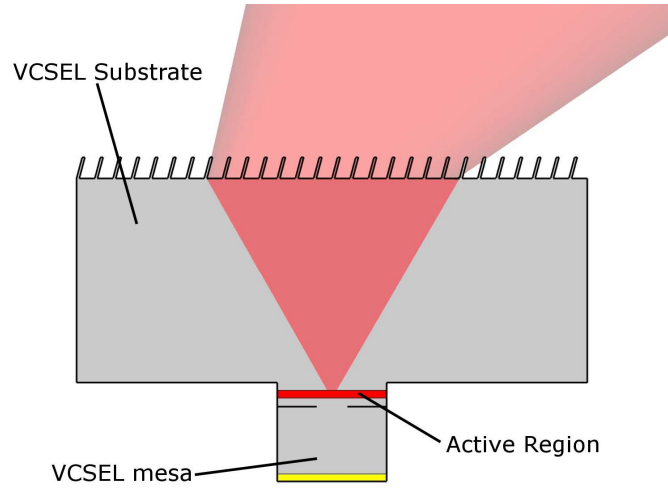


Figure 5.2: Illustration of VCSEL beam diverging as it passes through the VCSEL substrate. Because of this divergence gratings integrated into bottom-emitting VCSELs are made correspondingly larger.

put into a single order. Each segment is shaped such that incoming light is refracted into the diffraction angle. Therefore blazed gratings combine both refraction and diffraction (see figure 5.3).

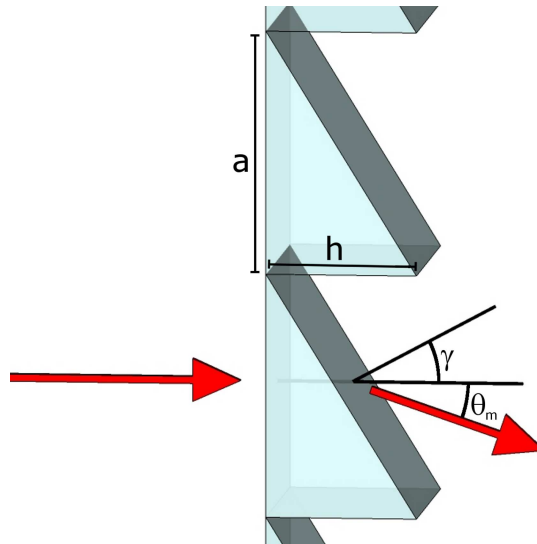


Figure 5.3: Diagram of blazed grating and component characteristics.

In order to design a blazed grating, we need to combine the equation of diffraction and Snell's Law:

$$\begin{aligned} d &= \frac{m\lambda}{\sin \theta_m} \\ \frac{n_2}{n_1} &= \frac{\sin(\theta_1)}{\sin(\theta_2)} \end{aligned} \quad (5.1)$$

Where 1 and 2 represent the different materials involved.

From figure (5.3), the diffracted angle θ_m can be defined using Snell's Law and trigonometric identities as:

$$\frac{n_2}{n_1} \sin(\gamma) = \sin(\gamma + \theta_m) \quad (5.2)$$

as such

$$\sin(\theta_m) = \frac{\frac{n_2}{n_1} \sin(\gamma) - \sin(\gamma) \cos(\theta_m)}{\cos(\gamma)} \quad (5.3)$$

From figure (5.3), the height of the blazed grating, h , can be defined from the blazed angle γ and equation (5.1) as:

$$h = d \tan(\gamma) = \tan(\gamma) \frac{m\lambda}{\sin(\theta_m)} \quad (5.4)$$

Therefore, from equation (5.3) and further trigonometric identities:

$$h = \frac{m\lambda}{\frac{n_2}{n_1} - \cos(\theta_m)} = \frac{m\lambda}{\frac{n_2}{n_1} - \sqrt{1 - (\frac{m\lambda}{d})^2}} \quad (5.5)$$

At this point all relevant variables are defined. From equations 5.1 and 5.5 it is possible to design a blazed grating where the majority of diffracted light is directed into almost any desired angle.

As an example, for a “steering” angle of 30° with a $\lambda = 980$ nm emission source, a grating with a period of $1.96 \mu\text{m}$ would produce first order diffraction at the desired angle. To maximise the light in the first order, the grating could be blazed to a depth of (from equation (5.5)) (taking into account the refractive index of the material (i.e. $n_2 = 3.6$) 358 nm. This corresponds to a blaze angle of 10.4° .

5.2 The Angled Grating

Etching of a true blazed grating into the VCSEL material would prove difficult. A greyscale mask technique could be employed — using techniques discussed in the previous chapter (i.e. both the mask and material beneath are etched simultaneously to transfer the 3-dimensional pattern in the mask to the substrate). However, etching of *GaAs* requires the use of chemically assisted ion beam etching (CAIBE) using chlorine as an etchant. In order to etch SU8 reactive ion etching (RIE) with oxygen is used. In my case these two gases are used in separate machines. I attempted to etch an SU8 mask using chlorine alone, however, the selectivity between the SU8 to *GaAs* was too high (i.e. the SU8 mask was barely etched while the *GaAs* was over etched) the opposite was true using oxygen, in the RIE (here the SU8 over etched while the *GaAs* was barely touched). Therefore this technique could not be employed.

A simpler method to create “steering” is to use an angled grating. The off-vertical-angle of the grating is made to match the 1st-order diffraction angle of the grating (figure 5.5). An angle of 30°, for example, requires a grating pitch of 1.96 μm (see figure 5.4), figure 5.4 is constructed using equation 5.6 (from [47]), which calculates the far-field of a multiple slit emission, by increasing the number of slits (N) a grating response can be approximated (this equation will be used again in chapter 7). By etching the grating at an angle of 15 degrees to the vertical, the zero-order light is also refracted at 30 degrees, so the zero and first diffraction orders both point in the same direction.

$$I(\theta) = I_0 \left(\frac{\sin(\beta)}{\beta} \right)^2 \left(\frac{\sin(N\alpha)}{\sin(\alpha)} \right)^2 \quad (5.6)$$

where:

$$\beta = \left(\frac{kd}{2} \right) \sin(\theta) \quad (5.7)$$

and:

$$\alpha = \left(\frac{ka}{2} \right) \sin(\theta) \quad (5.8)$$

with N the number of slits, $k = \frac{2\pi}{\lambda}$ where λ is the wavelength of the radiation, d the width of the slits and a the spacing between the slits.

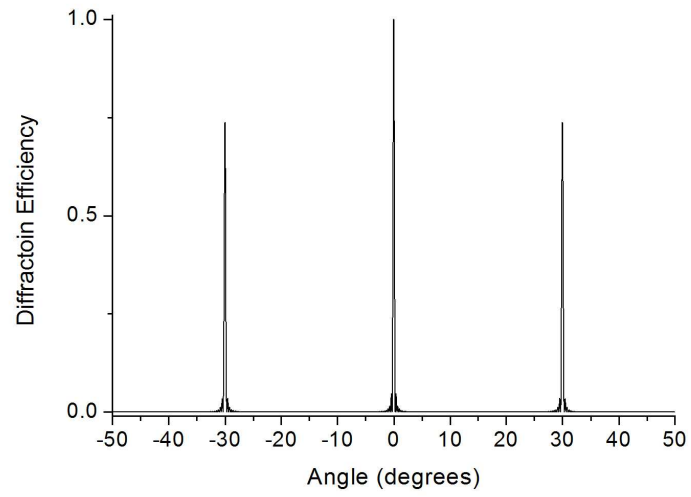


Figure 5.4: Graph of diffraction efficiency from a grating with a pitch of $2\ \mu\text{m}$.

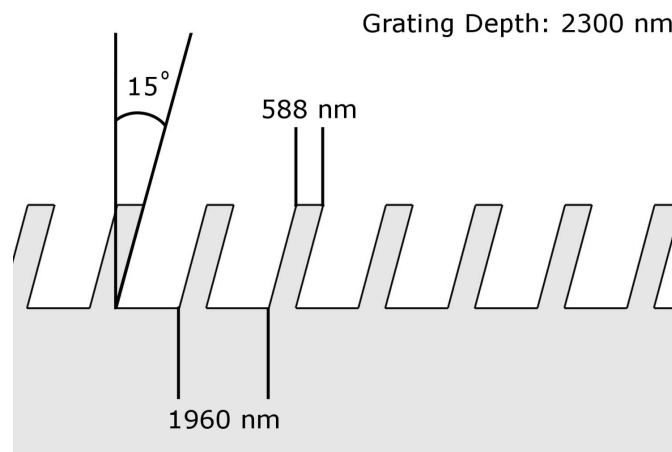


Figure 5.5: Illustration of proposed angled grating including key parameters.

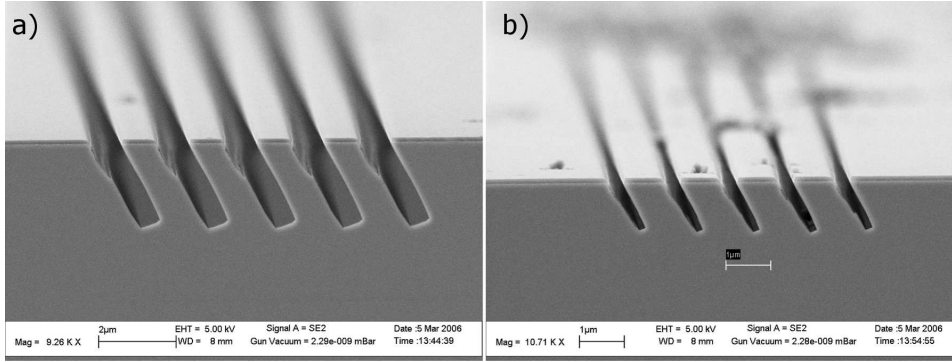


Figure 5.6: SEM images of angle etch grating tests. a) shows etch tests for depth — over $2\ \mu\text{m}$ is achieved b) shows etch tests for period — features approximately $300\ \text{nm}$ are observed.

5.2.1 Angled Grating Fabrication

Chemically assisted ion beam etching (CAIBE) was used in this process. To achieve an angled grating, the sample was mounted on an aluminium block. This block was milled to give an angle of 15° to the ion beam. Electron beam lithography (EBL) was used to create the pattern on the back of the VCSEL. To compensate for the diffraction of the light from a bottom emitting VCSEL (as light passes through the substrate the spot from a $5\ \mu\text{m}$ aperture will diffract to approximately $150\ \mu\text{m}$ in diameter), and because of difficult alignment to the VCSEL mesa, the grating pattern was made to cover a large area (i.e. $300 \times 300\ \mu\text{m}^2$). Figure 5.6 shows two SEM images of test etches performed on bare *GaAs* (i.e. *GaAs* without any VCSEL devices). Some degradation at the edge of each grating feature can be seen, but this did not have an adverse affect on performance. Figure 5.7 shows emission from an angled grating VCSEL demonstrating that steering was achieved.

5.2.2 Angled Grating Conclusion

This technique is therefore very interesting. The successful demonstration of steering highlighted the potential of such a technique. Steering with an efficiency of approximately 60% was achieved, which was measured by first determining the total emitted power (by placing a photodetector close to the emitting facet of the VCSEL), then the power in the positive-first order was measured by moving away from the VCSEL and blocking the negative-first and zeroth order emissions, the positive-first order was focussed onto the photodetector and the ratio between the total emitted power and power in the positive-first order was calculated. However, the fabrication method that is employed in such a process is complex. For multiple angle emission multiple etches are required to build the array and alignment toler-

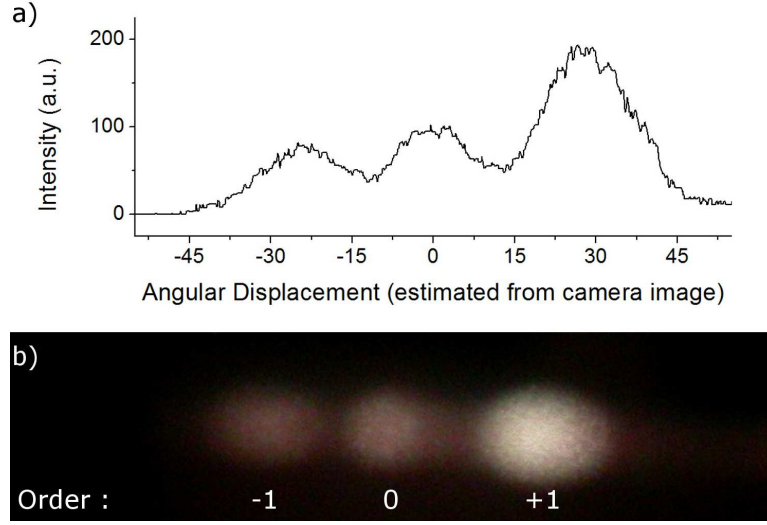


Figure 5.7: a) Cross-sectional cut through photograph of VCSEL emission through integrated angle grating (an estimated angular scale is given) and b) photograph of VCSEL emission. Principal emission is into the first diffraction order, steering efficiency is relatively low due to extra emission lobes.

ances would also require improvement. For these reasons, this technique was not adopted for future devices.

5.3 Sub-wavelength Gratings

As an extension to the angled grating work, and going back to the blazed grating idea, the use of sub-wavelength gratings was investigated. These gratings work on a different principle compared to the more macroscopic gratings already mentioned. The feature size within the grating is reduced to below the wavelength of the intended radiation. The radiation then does not “see” the fine structure of the grating, but instead sees an effective refractive index. This effective index can be approximated by the respective fill-factors of the high and low refractive index constituents. With the advanced micro-fabrication technologies available features sizes of approximately $\frac{\lambda_0}{10}$ have been achieved.

A continuous refractive index range from 3.6 (one unit cell full of *GaAs*) to 1.0 (one unit cell full of air) is possible with this technique. The depth of the grating is used to change the overall optical path length. The deeper the grating trenches the longer the path length (e.g. $10 \mu\text{m}$ of *GaAs* is equivalent to $(10 \times 3.6) \mu\text{m}$ of air).

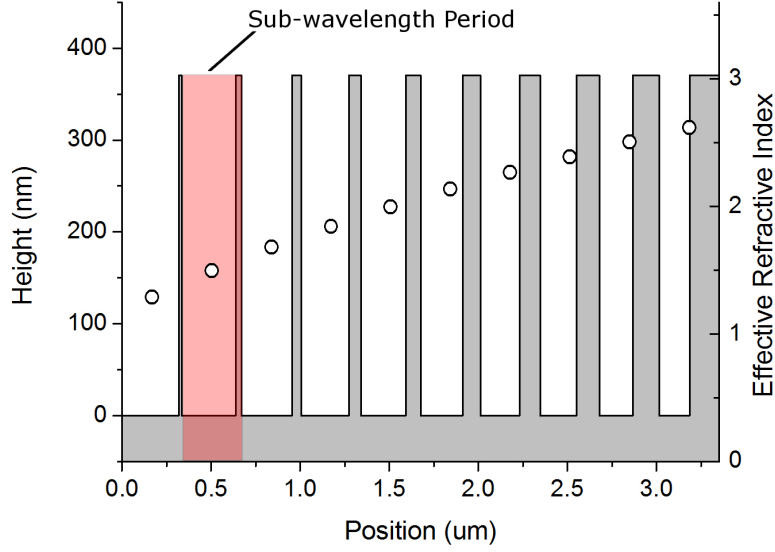


Figure 5.8: Graph of sub-wavelength grating profile with effective refractive index produced by each sub-wavelength-period (effective refractive index markers placed at the center of each sub-wavelength-period).

5.3.1 Sub-wavelength Grating Design

There are many ways to design sub-wavelength gratings, one of which uses the effective refractive index method outlined above which is simple to implement. However the technique above results in very small features. I designed a simple grating with a steering angle of 17 degrees using the effective refractive index method from above, which resulted in a grating period of $3.29 \mu\text{m}$. Splitting this grating-period into 10 sub-wavelength-periods and calculating the fill-factor for each period to give a linear, continuous effective refractive index change over the grating period. I found that the smallest feature required was 18.5 nm thick. Such small sizes could not be fabricated reproducibly in our systems.

However, work carried out at Sandia National Laboratories by M. E. Warren et al. [48] has shown that steering efficiencies of 85% are possible with this technique. Using an iterative method and an implementation of the rigorous coupled-wave analysis [49], they have designed an algorithm that maximises the steering efficiency of the grating, by varying the width and position of its grooves. Their design calls for a minimum feature size of 63 nm instead of 18 nm (see figure 5.9). I have, therefore begun by using their design which has feature sizes at the limit of our fabrication systems.

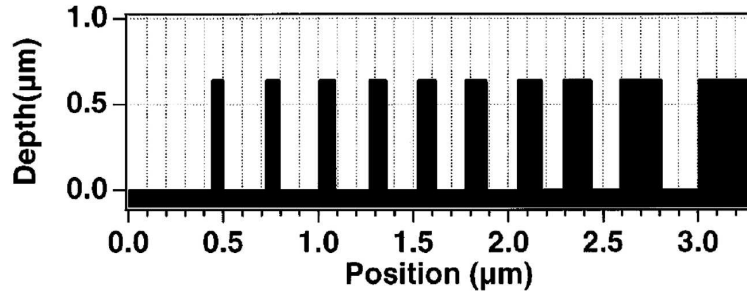


Figure 5.9: Sub-wavelength grating profile for 17.3° steering in *GaAs*, taken from [48]

5.3.2 Sub-wavelength Grating Fabrication

Due to the size of the features in these devices etch mask definition had to be done with EBL. A number of etch tests were performed first. Bare *GaAs* was used for the test substrates. These tests were performed to optimise the EBL resist. For this work ZEP (ZEP-520A, Zeon Corporation) was chosen as a resist. ZEP is a high resolution positive electron sensitive resist. It has a number of advantages over other resists such as Poly(methyl-methacrylate) (PMMA), such as three-fold increased sensitivity and better dry etch resistance. I started by using Undiluted ZEP, spun at 3000 rpm for 60 seconds and then baked at 180°C for 10 minutes. This resulted in a film approximately 350–400 nm thick. Initially, features of 650 nm were achieved. These were not small enough but useful for etch process development. By increasing the flow of chlorine (from 2.0 sccm (VCSEL mesa etch recipe) to 2.7 sccm), and reducing the acceleration voltage (from 1450 v to 87 v) an etch depth of 280 nm was achieved after a 4 minute etch, resulting in smooth, vertical sidewalls.

In order to increase the resolution of the ZEP, I increased the spin speed from 3000- to 5000-rpm (resulting in a film thickness of below 200 nm), a resolution down to 60 nm was then achieved. At this level of feature size, roughness in the etch mask becomes significant (see figure 5.10). As such, the etch recipes and exposure and development times are continually adjusted. With all processes in place to a good tolerance the gratings were integrated onto VCSELs (figure 5.11).

5.3.3 Sub-wavelength Gratings Conclusions

As of yet, steered emission from a VCSEL with integrated sub-wavelength grating has not been achieved, because of both VCSEL and grating issues. In fabricating a

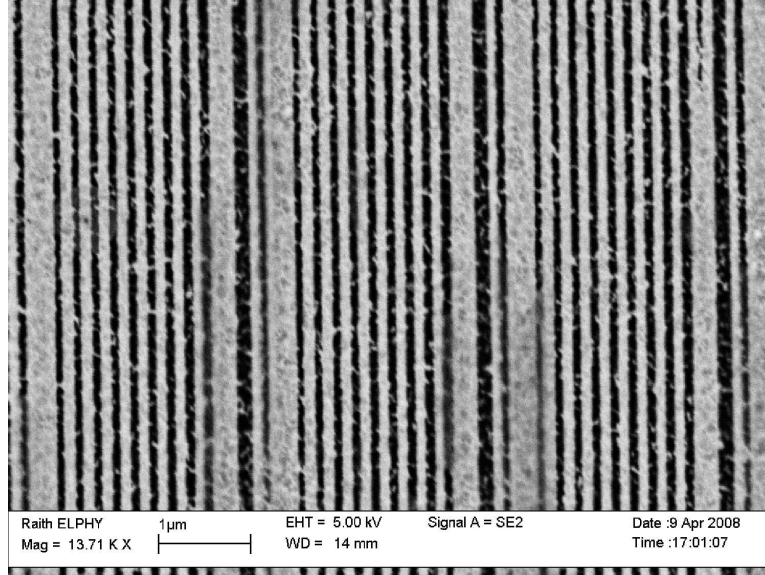


Figure 5.10: SEM image of sub-wavelength grating. Grating-scale edge roughness is evident.

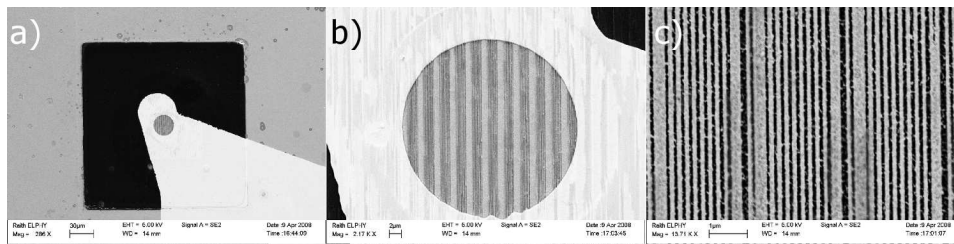


Figure 5.11: SEM images of completed sub-wavelength grating integrated VCSEL.

sub-wavelength grating, feature size tolerances are very important. To achieve high tolerances a good repeatable ZEP layer must be spun on top of the VCSEL chip. This is difficult due to the non-planar surface. Even using SU8 to planarise the VCSEL chip, deviations still exist that can disrupt the ZEP film. The top-emitting VCSELs used for this work have a 5 nm capping layer of *GaAs*, however the sub-wavelength gratings require an etch depth of greater than 500 nm. Therefore, the gratings are etched into the top DBR of the VCSELs this degrades their performance. In summary, integrated grating based beam steering is difficult to achieve while micro-prism greyscale fabrication is easier, due to micro-prisms not requiring complete planarisation of the VCSEL chip (due to their greater than micrometer heights) and their less stringent alignment tolerances. To take sub-wavelength gratings further a VCSEL wafer with a thicker capping layer would be required.

Chapter 6

Liquid Crystal Cell for Dynamic Beam Control

6.1 Introduction

Liquid Crystals (LCs) consist of special molecules that have the ability to exist between the solid and liquid phase. They can show both isotropic behaviour (i.e. long distance order), as well as anisotropic behaviour. The molecules within a liquid crystal are often shaped like rods or plates, which encourages them to align along certain directions within the bulk material. Liquid crystals are investigated here because their order can be manipulated by thermal and electrical forces.

Liquid crystals were first discovered in 1888 by Friedrich Reinitzer when conducting experiments on cholesterol based substances obtained from the common carrot. In trying to determine the melting point of the substance, he observed that the material seemed to have two separate and distinct melting points. At 145.5 °C, the solid crystal melted into a cloudy liquid and then on to a clear liquid at 178.5 °C. Reinitzer took his discovery to the German physicist Otto Lehmann who was an expert in crystal optics. Lehmann examined the intermediate liquid state and found that it contained a unique level of order. In contrast, he found that the final liquid state had the characteristic disordered state of all common liquids. Lehmann eventually determined that the intermediate liquid was in fact a new state of matter and it was Lehmann who coined the name “Liquid Crystal” [50].

Liquid crystals (LCs) have two main phases known as nematic and smectic. The nematic phase is the simplest LC phase and is close to the liquid phase. The molecules are free to move within the material but remain ordered in their orientation. The smectic phase, on the other hand, is close to the solid phase of a LC. The molecules within this LC are ordered into layers; within each layer, the crystals are free to

move, but they are unable to move from one layer to another. Therefore, nematic phase LCs can be thought of as ordered, while smectic phase LCs are unordered (although each phase does exhibit order of some fashion). Because the molecules that make up an LC are “rod-like” in shape, LCs exhibit two refractive indices (i.e. are birefringent) one refractive index when the molecules are aligned perpendicular to the propagation of light, and one when aligned parallel.

In this chapter I develop a liquid crystal cell that can be used for dynamic steering. This differs from the previous steering mechanisms in that the emission angle of the VCSEL can be controlled electronically, figure 6.1 illustrates the proposed system. A small liquid crystal cell is integrated directly on top of the emitting aperture of the finished VCSEL (contact pads for the cell are not shown in the diagram) by altering the drive current of the LC cell the VCSEL emission can be made to swing in direction. A number of considerations must be taken into account the first being whether to use top- or bottom-emitting VCSELs. Top emitting VCSELs provide for easy alignment of the LC cell but have a limited emitting aperture, where as bottom emitting VCSELs, due to divergence within the VCSEL substrate, have a far larger emitting aperture. As will be discussed (see section 6.3 and figure 6.6) the limits imposed by the fabrication steps used in fabricating the LC cell constrain the smallest LC pixel to a width of $2\text{ }\mu\text{m}$, therefore a top emitting VCSEL, with a typical aperture of $30\text{ }\mu\text{m}$ diameter, provides space for 7–8 pixels (i.e. $2\text{ }\mu\text{m}$ contacts with a $2\text{ }\mu\text{m}$ spacing), whereas far more pixels can be included if using a bottom emitting VCSEL. This choice then impacts on the spacing of the final VCSEL array, with larger LC cells mounted to the bottom of the VCSEL chip, the individual VCSELs must be spaced in accordance.

6.2 Liquid Crystal Operation

Using a twisted nematic liquid crystal (TNLC), sandwiched between two crossed polarisers, an array of LC pixels can be fabricated that transmits or rejects light (according to an applied electrical field). This effect is used widely today in the form of flat-panel displays [50]. By applying an electric field across the LC cell, the molecules within the LC align to the field. This removes the birefringence (the molecules are aligned so that only one refractive index is prevalent) and the polarisation of the light travelling through the cell is no longer rotated. With an appropriate cell design, pixels within the cell can be made to transmit or reject light. Colours within a liquid crystal display (LCD) use the same technique except that the back-light is filtered to produce pixels of red, green and blue. From these pixels any colour required can be built up. Figure 6.2 shows an illustration of the LC cell (the crossed polarisers are not shown).

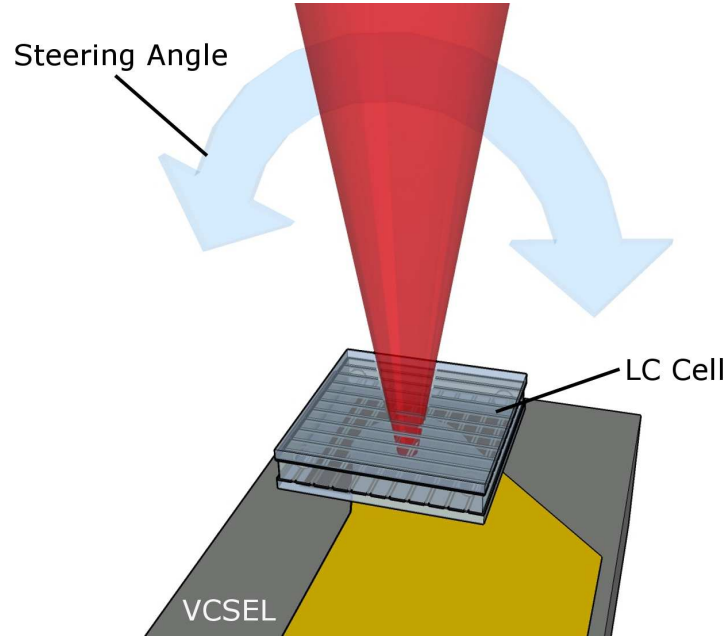


Figure 6.1: Illustration of liquid crystal cell integrated with a top-emitting VCSEL (although bottom-emitting VCSELs will be used during this work, a top-emitting VCSEL is illustrated for clarity).

By controlling the strength of the electric field, the response of the LC can be controlled. Therefore, the ordinary and extraordinary refractive indexes (n_o and n_e) of the material and hence the effective index can be adjusted, which can be used for beam shaping and dynamic beam steering. Linearly polarised light incident on a LC cell will experience a different refractive index according to the electric field applied to the cell. Two different examples for optical elements created by this method (a prism and a lens, respectively) are shown in figure 6.3. By integrating a LC cell with a VCSEL, the refractive index profile of the cell can be tailored to control the VCSELs emission. In order to facilitate this functionality, the VCSEL has to be polarisation-stable.

6.3 Liquid Crystal Cell Fabrication

A photomask containing the LC cell contact pattern was fabricated. The contact pattern consisted of an array of long thin pixel regions ($5 \mu\text{m}$ wide) (figure 6.4a) extending at their ends to wide contact pad areas ($200 \mu\text{m}$ wide) (figure 6.4c). Using glass cover slips, coated with a 120 nm layer of indium tin oxide (ITO) (a transparent conductor), the LC cell contacts were defined. The ITO was etched using

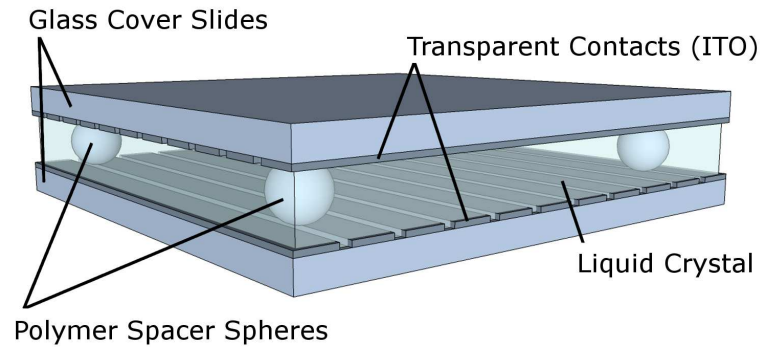


Figure 6.2: Illustration of liquid crystal cell, including transparent (in this case, indium tin oxide) contacts and polymer spacer spheres.

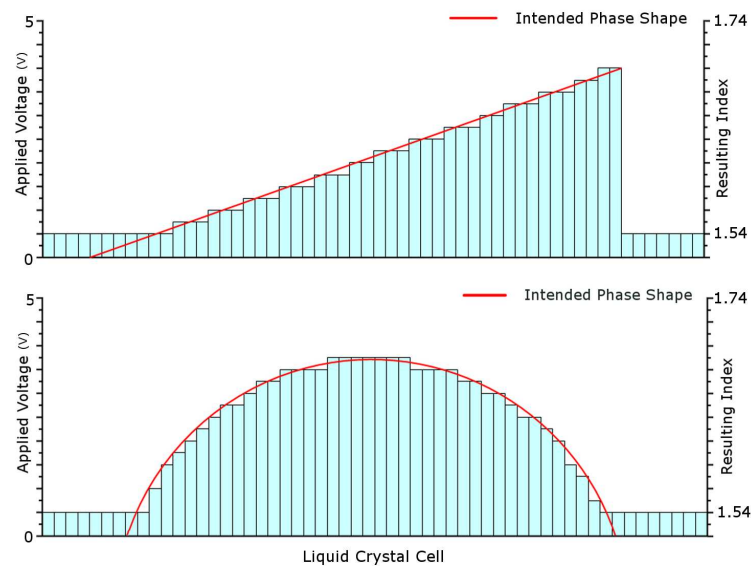


Figure 6.3: Illustrations showing that by changing the index of refraction of a Liquid Crystal cell (by applying a variable voltage) optical components such as lenses and prisms can be created.

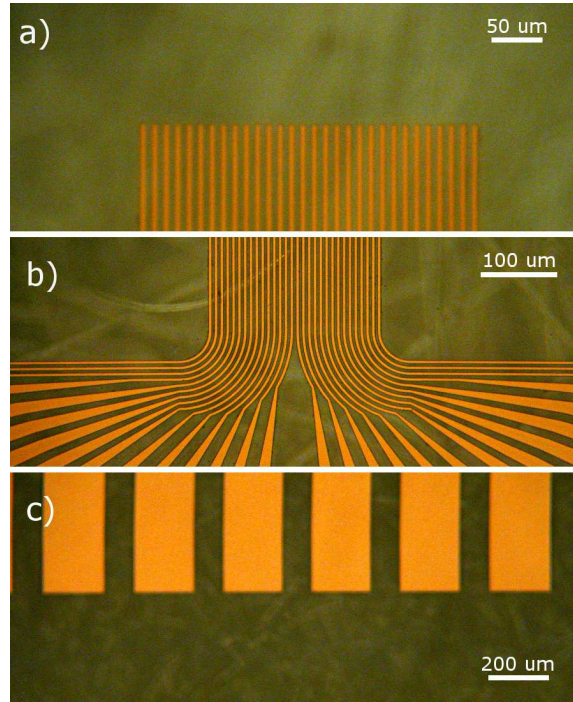


Figure 6.4: Photograph of liquid crystal photomask a) “finger” contacts, measuring $5\ \mu\text{m}$ with a $5\ \mu\text{m}$ spacing, b) transition region between “finger” contacts and electrical pads, and c) contact pads measuring $200\ \mu\text{m}$ with a $100\ \mu\text{m}$ spacing.

reactive ion etching (RIE) and an oxygen plasma for approximately 5 minutes. Two cover slips were prepared per LC cell. Each slip was given an alignment layer (by spinning a layer of flowable oxide (FOx-12) and baking the layer to form a layer of silica) and a preferred alignment direction by “rubbing” the silica covered face in the required direction of alignment (with a linen cloth or lens paper). Such “rubbing” leaves a uniform and unidirectional tilt of the dangling bonds or side chains on the “rubbed” surface. The LC then aligns itself preferentially to this axis [50].

First, a solvent containing polymer spacer spheres is inserted between the two slips. When the solvent evaporates it leaves the polymer spacers and the two plates are held apart by exactly $2\ \mu\text{m}$. Next, the two slips are sealed around the cell edges using glue leaving only small voids for introducing the LC. Finally, the LC is inserted into the cell. The cell is then completely sealed and electrical connections are made to the two plates for control and subsequent testing.

During this work, the LC pentylcyanobiphenyl (5CB) was used. This was chosen due to its wide use in other research areas. It has a temperature range of $25\text{--}35\ ^\circ\text{C}$ and an ordinary (n_o) and extraordinary refractive index (n_e) of 1.54 and 1.74 respectively (at $\lambda = 515\ \text{nm}$).

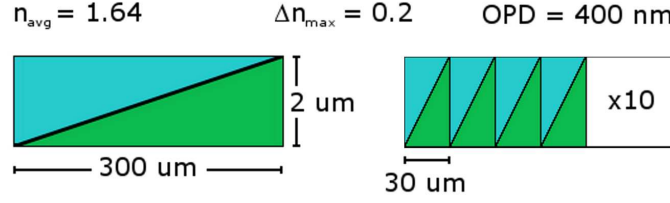


Figure 6.5: Illustration of prisms imposed on the liquid crystal cell during testing.

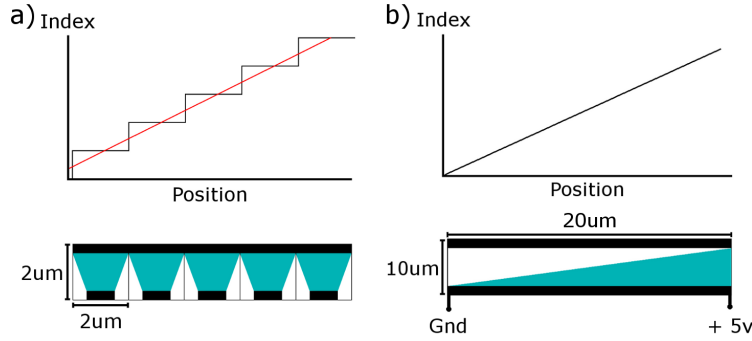


Figure 6.6: Illustration of possible liquid crystal cell designs, a) using $2\ \mu\text{m}$ pixels, a step-like index gradient would be observed, this would be smoothed somewhat due to the electric field overlap between each pixel. b) using the resistive properties of the bottom contact, a smooth varying electric field could be applied across the cell, resulting in a smooth index profile.

With a refractive index range of approximately 0.2, a prism set-up across the LC cell (i.e. with an index at one side of the cell of 1.54 and an index at the other side of 1.74), will produce an optical path difference of Δnd of 400 nm (figure 6.5). This results in a prism angle of only 0.1 degrees. Taking the average refractive index of the cell to be 1.64, a refraction angle of 0.16 degrees (taking into account the prism angle and a steering angle of 0.1 degrees from the normal of the cell) could be achieved. This could be increased by making multiple prisms across the LC cell. During this work ten prisms were created across the cell. This meant that in each sub-prism, three LC pixels were used. These sub-prisms would result in an approximate steering angle of 1.0 degree.

6.4 Liquid Crystal Results

A number of LC cells were fabricated. The first devices used a common ground contact (i.e. one ITO covered glass plate not etched with a contact pattern). To test

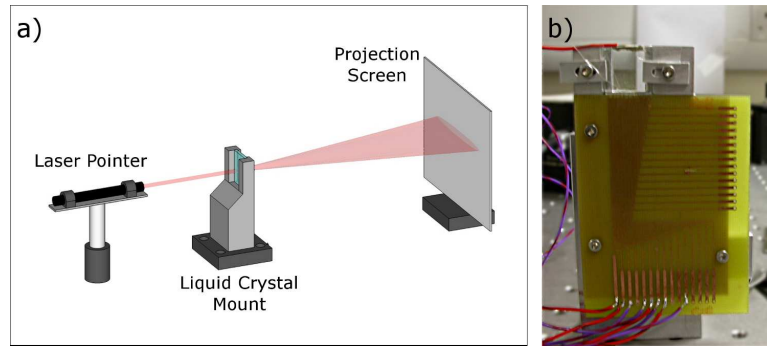


Figure 6.7: a) Illustration of liquid crystal experiment and b) photograph of liquid crystal mount and integrated circuitry.

the cell, a laser pointer (green or red) was mounted to an optical bench and directed towards and through the LC cell (figure 6.7). The far-field pattern produced by the LC cell was then observed and recorded using a digital camera.

Using the common ground devices a diffraction grating of differing period was imposed onto the cell. This is accomplished by energising only some of the “finger” contacts. Figure 6.8, shows the first results from one of the earliest devices. Without a voltage applied, a diffraction pattern is observed (figure 6.8a). This is due to the ITO contact fingers and their spacing of $5\ \mu\text{m}$. When the cell was energised with an additional grating (figure 6.8c), additional diffraction orders were produced (figure 6.8b). This proved that the LC cell operated as expected (i.e. a change in refractive index through the cell was observed).

To test the steering capabilities of the devices a multiple-prism, consisting of 10 small-width prisms, was imposed on the cell using a voltage range of 0–5 volts. To produce the voltages required a set of potential dividers was used — reducing the number of power supplies required. Figure 6.9 shows the results obtained from the experiment. Figure 6.9 shows that the efficiency of the LC steering was low. To view the steered lobes the central straight-through emission had to be obscured. This was because the central lobe was powerful enough to conceal the extra lobes created by the LC prism. As the voltage on the cell was increased from 0 volts (i.e. no prism) to a 2 volt maximum and finally a 5 volt maximum the steered lobe moved over a certain angle (approximately 0–1 degree) (see figure 6.9). This result matches the expected 1.0 degree. Extra diffraction patterns are observed due to the fashion the multiple-prism is set-up. Using only three different voltages, a smooth refractive index gradient is not possible.

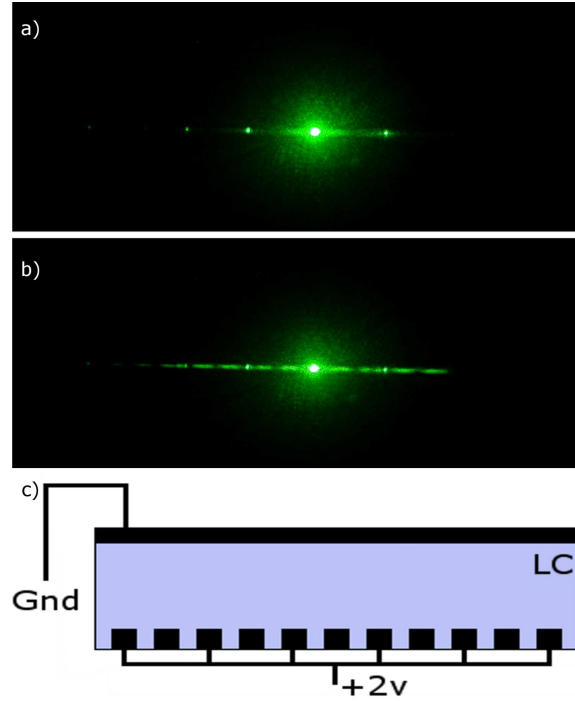


Figure 6.8: Photographs taken of a) laser light transmitted through liquid crystal cell with no voltage applied (diffraction pattern created by liquid crystal cells is visible), b) emission through liquid crystal cell with a 2 volt amplitude grating applied (extra diffraction orders become apparent)

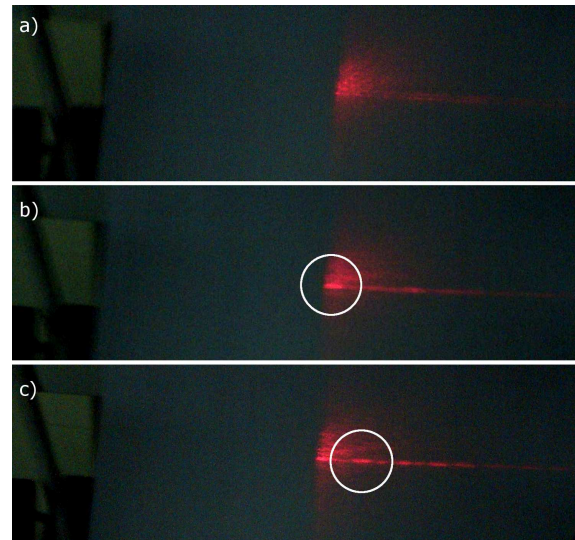


Figure 6.9: Photographs taken of laser light transmitted through liquid crystal cell a) no prism, b) prism created with 1 volt amplitude and c) prism created with 2 volt amplitude. Highlighted is the steered mode created by the imposed prism — as the voltage is increased the mode moves towards the right. The central beam and other diffraction orders of the pattern created by the liquid crystal cells have been obscured for clarity.

6.5 Conclusions

The liquid crystal cell is an elegant solution to the challenge of dynamic beam steering. The advantage of using LCs is their large index tuning range that can be controlled by altering an applied electric field. This tuning range, by using a matrix addressable pixel design, would allow the realisation of optical components such as lenses, prisms, etc. (see figure 6.3).

An LC cell consisting of 30 individually controlled $5\ \mu\text{m}$ wide strips was constructed. The resulting steering angle was approximately 1 degree. This steering angle was limited by a number of factors. Firstly the refractive index range, although large compared to other techniques, produces a small effect over the distances used in this work. The LC cells were $2\ \mu\text{m}$ thick, with a refractive index change of approximately 0.2 which resulted in an optical path difference of 400 nm. The active area of the cell was $300\ \mu\text{m}$ wide, with the optical path difference, this meant that using the entire width of the cell a prism with an angle of only 0.1 degrees could be achieved — this resulted in a steering angle of approximately 0.1 degrees. Increasing the cell's thickness would have increased this steering angle, however, the optical resolution of the system diminishes with increased cell thickness. The light passing through one pixel of the cell diverges into the neighbouring pixel, which tends to wash out the effect of the two individual cells.

The steering angle was increased by making use of a multiple-prism design (see figure 6.5). However, by decreasing the number of pixels used to create the prism the refractive index gradient was made worse. This decreased the efficiency of the cell by creating extra diffraction lobes in the far-field pattern. To improve the cell a finer pixel pitch would have to be chosen. Figure 6.3 shows that the index profile across the device depends upon the number of pixels within the cell (i.e. the number of individually addressable regions). To achieve a smooth index profile the pixel pitch must be made as small as possible. Decreasing the pixel size to $2\ \mu\text{m}$ (i.e. a $1\ \mu\text{m}$ contact with a 50% duty-cycle) (see figure 6.6a) and using, as before, 3 pixels per small-width prism, a maximum steering angle of 5 degrees could be achieved. However, using only 3 pixels, this design would not, as mentioned, create a smooth index profile. This design and any with smaller features, would also require moving to electron beam lithography.

Another approach for smoothing the index profile, would be to use two common contacts. By applying a voltage to one end of the contact and grounding the other, the voltage drop across the contact would create a varying electric field across the cell. Using a $20\ \mu\text{m}$ wide cell with a depth of $10\ \mu\text{m}$ a steering angle of approximately

5 degrees would result. This steering, however, would be more efficient as the far field would not include unwanted diffraction orders. The steering angle would also be variable, by simply altering the two differential voltages (see figure 6.6b).

The cell, unfortunately, was quite large (22x22 mm) (see figure 6.7). This could have been reduced to less than 10x10 mm, as the actual LC contact pattern covered a region of only 300x300 μm . However, with these problems we could not see how to improve the design as massively as was necessary, and we therefore moved away from this beam control technique. The next chapter will outline a more promising approach — that of coupled-VCSELs.

Chapter 7

Coupled VCSELs for Dynamic Beam Control

7.1 Introduction

As mentioned in the previous chapter as well as static beam conditioning I have also considered dynamic beam conditioning. These differ from the static methods by giving continuous control over a beam parameter such as beam divergence or beam direction (i.e. steering). This chapter will outline the work that has been carried out to date on coupled VCSEL arrays.

This work investigates evanescent optical coupling between at least two physically adjacent VCSELs. I will discuss two approaches used within this work. One approach uses macro-double-mesa designs (see figure 7.1a) and the second uses photonic crystal cavities to define the individual devices (see figure 7.1b).

Evanescent optical coupling between the VCSELs means that each emitter of the array can be treated as separate — this allows for simplification of the theory. This theory will be outlined in the following sections. For analysis of this technique, I have used simple single-transverse mode emitters.

7.1.1 Beam Divergence Control

It is possible to simplify the analysis of this system to that of antenna theory or a multiple slit/diffraction grating problem [51, 52]. Equation 7.1 (first seen in chapter 5) (from [47]) calculates the far-field intensity distribution of a multiple slit emission:

$$I(\theta) = I_0 \left(\frac{\sin(\beta)}{\beta} \right)^2 \left(\frac{\sin(N\alpha)}{\sin(\alpha)} \right)^2 \quad (7.1)$$

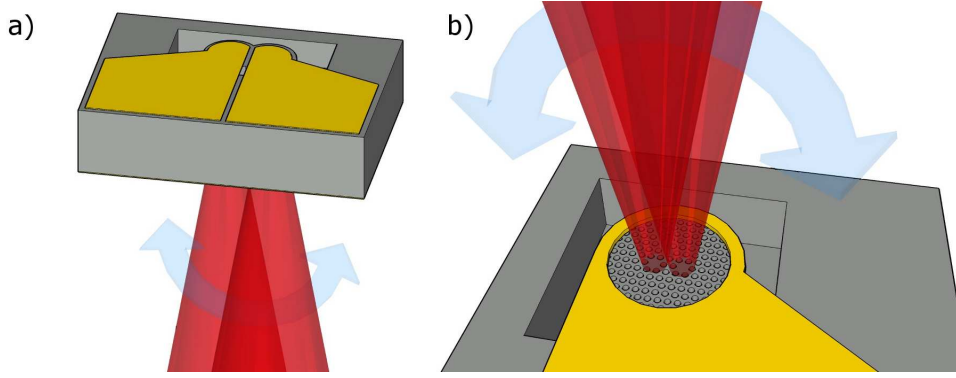


Figure 7.1: Illustration of coupled VCSEL for dynamic beam control. Control over the far-field intensity distribution is via the interference properties of the two emitted beams.

where:

$$\beta = \left(\frac{kd}{2} \right) \sin(\theta) \quad (7.2)$$

and:

$$\alpha = \left(\frac{ka}{2} \right) \sin(\theta) \quad (7.3)$$

with N the number of slits, $k = \frac{2\pi}{\lambda}$ where λ is the wavelength of the radiation, d the width of the slits and a the spacing between the slits.

Equations 7.1, 7.2 and 7.3 result in a Sinc^2 relationship in the far-field. The principal lobe (centred around zero) narrows as the number of slits (i.e. emitters) is increased (i.e. as N increases the full-width half-maximum (FWHM) of the principal lobe of the function decreases). Analogously by using large arrays of in-phase VCSELs, it is possible to have dynamic control over the divergence of the emitted radiation. Figure 7.2 shows results from the equations above. Figure 7.2 shows how the divergence of the array decreases as the number of emitters is increased. From equations 7.1, 7.2 and 7.3 by decreasing the spacing between the slits it is possible to make the emission pattern more efficient (i.e. increase the power in the 0^{th} order with respect to the higher orders). This is analogous to decreasing the spacing within the VCSEL array.

7.1.2 Beam Direction Control

Taking this argument into 2-dimensions it is possible to construct a model that simulates two or more single-mode VCSELs. By taking the Fourier transform of the

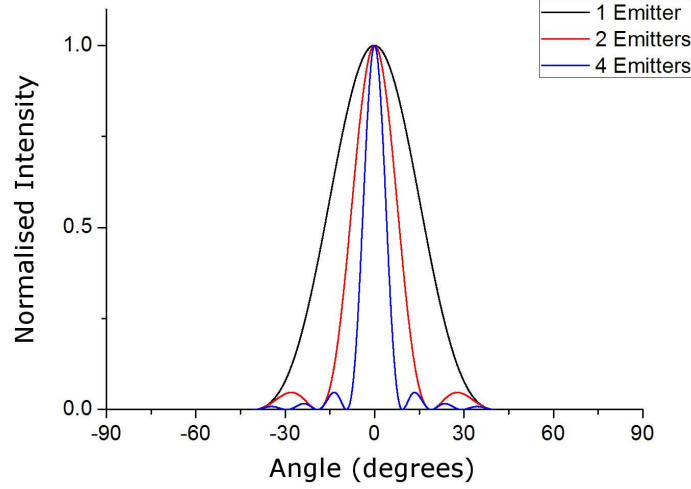


Figure 7.2: Graph of multiple in-phase emitter array far-field intensity profile. Data taken from the multiple slit model.

near-field intensity distribution produced by this model it is possible to look at the expected far-field distribution from such an emitter array. I have constructed such a model, whereby individual VCSELs are represented as pure Gaussian emitters and an arbitrary phase relationship is imposed between the resulting patterns. I have also simulated these types of arrays with commercially available beam propagation software (FullWAVETM from the RSoft Design Group). The model I have constructed, and that of the simulation software, compare favourably and therefore the model I have made will be used in this analysis.

This approach to modelling the coupled VCSEL array is much like that of coupled antenna theory. In particular the use of scanning antenna arrays. In this type of system it is possible to scan the emission direction of an array of antennas by varying the phase of the driving signal between each antenna (in an antenna the phase of the signal is varied by simply changing the phase of the driving current/voltage applied to the antenna — unfortunately this is not how the phase in a coupled VCSEL is varied and this will be discussed in the next section). By increasing the phase difference between adjacent coupled VCSELs, the direction of the main lobe of the far-field intensity pattern can be altered continuously.

Figure 7.3 shows the far-field of a double VCSEL coupled array with varying phase shifts between each emitter. As the phase difference is increased the 0^{th} order mode is shifted from 0 degrees to a maximum — determined by the spacing of the emitters, the greater the spacing the lower the maximum steering angle. However, as

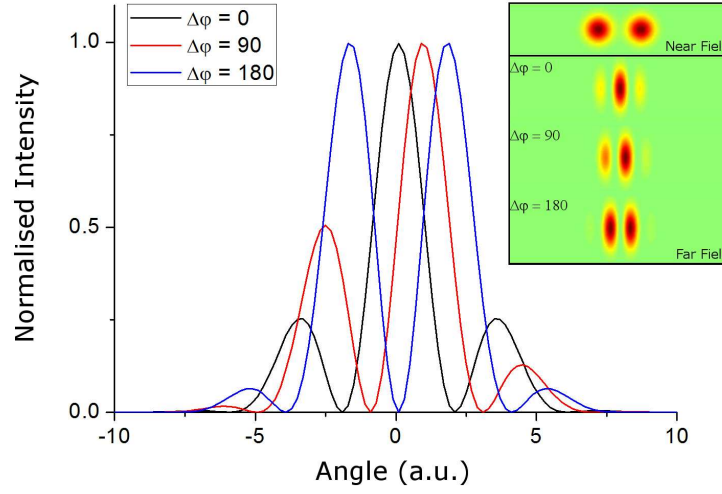


Figure 7.3: Graph of 2 coupled VCSEL emitters with varying degrees of phase difference. Insets show the 2-dimensional near- and far-field patterns from such arrays.

the phase is increased the major higher order mode increases in power. Therefore the efficiency of the steering system decreases (efficiency, in this case, is defined as the amount of light in the most powerful higher order with respect to the 0^{th} order) (see figure 7.4).

The major higher order increases in power to a maximum when the phase difference between the two emitters is 180 degrees. At this point the power in the major higher order is equal to the power in the main lobe (i.e. at this point the efficiency of the system has decreased to 50%). By shifting the phase in the other direction it is possible to have steering in the opposite direction (effectively doubling the total continuous steering angle of the system. However, the loss in efficiency must be taken into account).

By combining both of these effects it should be possible to build a system that has both continuous control over the divergence of the emission (by powering more VCSELs within the array) and continuous control over the steering angle of the emission (by changing the phase between the VCSELs within the array). In order to increase the total steering angle the emitters of the array must be placed closer together.

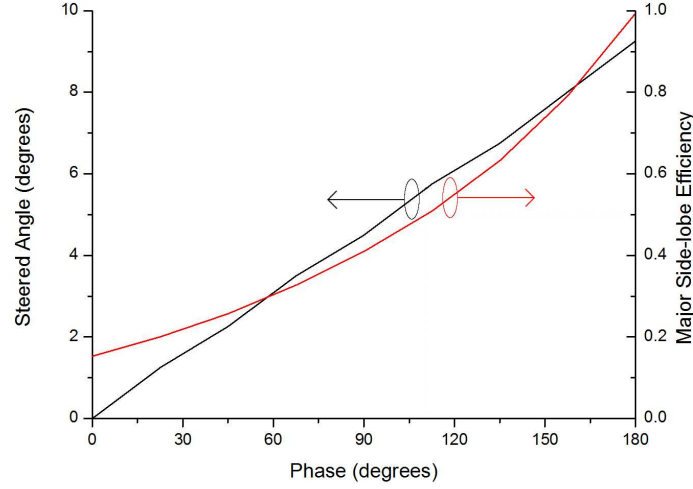


Figure 7.4: Graph showing main-lobe direction against phase difference. Also shown is the efficiency of the most powerful higher order mode with respect to the main lobe.

7.1.3 Phase Control within a Coupled VCSEL

To alter the phase of a VCSEL, there are two principal methods. Firstly, carrier injection; by increasing the drive current of a VCSEL the number of charge carriers within the device increases. With this increase a change in refractive index is observed. This change alters the phase of the optical field. Since the two VCSELs involved are coupled, this phase change can cause the VCSELs to oscillate with a certain phase difference. Secondly, increasing the drive current of the VCSEL also heats the device substantially (proof of this can be seen in the thermal rollover of the light-current characteristics of almost any VCSEL), this heating also changes the local refractive index of the device altering the optical phase.

If thermal effects cause the largest refractive index change then can external micro-heaters be used to control the phase of the optical field? This approach has been used in other systems [53, 54, 55]. Unfortunately, the spreading of the heat within the device is of greater extent than the actual size of the coupled VCSEL. As such externally heating one coupled VCSEL without heating the other would be difficult, if not impossible.

One draw-back to this method of phase control is that, to change the phase relationship between two coupled VCSELs, it is necessary to drive one of the VCSELs harder. This, while producing a phase change, also changes the output power of the VCSEL. This causes coupling effects to become less evident as the mis-match in output power means that complete cancellation of parts of the far-field intensity

distribution is no longer possible.

7.2 The Coupled VCSEL Array

In order to investigate these properties, I decided to fabricate coupled VCSEL arrays. As mentioned above, two approaches were taken in parallel.

7.2.1 Photonic Crystal VCSEL Design

Much work has been carried out on photonic crystal (PhC) cavity coupled VCSELS [56, 57, 58, 52]. A PhC VCSEL makes use of one single relatively broad-area mesa. The emitting surface of this VCSEL is patterned with a PhC and defects within this crystal are used to delineate the VCSEL array. The crystals used in this technique are not relied upon to create an in-plane photonic-band-gap (PBG); instead they are used more like their photonic crystal fibre counterparts [59], forming a waveguide at each defect. The interaction between the two waveguides can then be controlled by the design parameters of the crystal.

A. J. Danner et al., in [56], show a 2x1 PhC-cavity coupled VCSEL built into an 25 μm oxide aperture VCSEL. An oxide aperture of 25 μm would normally produce multi-mode output, but, by using the PhC to define the lasing cavities, single mode operation is observed. The emission from both cavities is also out-of-phase coupled, as evidenced by the double-lobe observed in the far-field measurements. When the emissions are not coupled a superposition of the two VCSELS is observed (see figure 7.5). Figure 7.5 is also in good agreement with figure 7.2, confirming the multiple slit/diffraction pattern analogy discussed previously. Out-of-phase operation, is of course, very useful when designing large high-output power devices. In these cases the far-field pattern is not as important as the spectral purity of the emission. By providing coupling between multiple emitters, spectral purity can be preserved over the entire array. However, for beam control, in-phase emission and continuous phase control is important.

In 2006, K. D. Choquette et al., [60], presented work on in-phase PhC-cavity VCSEL arrays. By adjusting the cavity interaction, by altering the PhC properties between the two defects (in this case the size of the air-hole between the two defects was adjusted), in-phase operation was observed. This is believed to arise from the lower optical losses experienced by the in-phase mode, compared to the losses from the more conventional crystal design presented in [56].

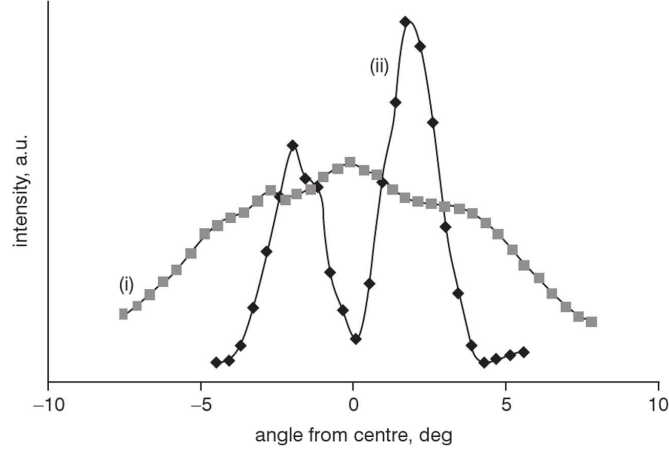


Figure 7.5: Graph taken from [56], (i) shows emission from two un-coupled PhC defects, while (ii) shows the emission from two coupled defects.

K.D. Choquette et al. [60] also presented results showing a relationship between the phase (of the two VCSELs) and the drive current. By increasing the current a shift in the far-field pattern is observed. To investigate which phase control mechanism is dominant (i.e. thermal or carrier density) the VCSEL arrays presented in [60] were driven with a modulated current source. By modulating the drive current, thermal effects, but not carrier effects, can be neglected. Results obtained with both continuous wave (CW) and pulsed operation show similar phase relationships. Although this result points to carrier density modulation as a phase control parameter it does not completely discount thermal effects. The results were taken with a current modulation period of $1 \mu\text{s}$ and a 50% duty cycle — this cannot eliminate thermal effects completely as mentioned in [60]. As such, the mechanisms behind phase control in these and similar systems is still unclear.

7.2.2 Photonic Crystal VCSEL Fabrication

To start, top emitting VCSELs were fabricated as outlined in previous chapters. Once this was complete, the VCSELs were spun with undiluted ZEP (an electron sensitive resist) at 3000 rpm for 60 seconds. After baking the resist at 180°C for 5 minutes electron beam lithography (EBL) was used to define the PhC pattern. The crystal had a lattice constant (a) of approximately $7 \mu\text{m}$ with a hole radius (r) of $2 \mu\text{m}$, giving a hole diameter-to-lattice constant of 0.3 similar to the designs presented in [57] (see figure 7.6a). Using a 3-point alignment process, the patterns were located on the emitting surface of each VCSEL. After developing the resist,

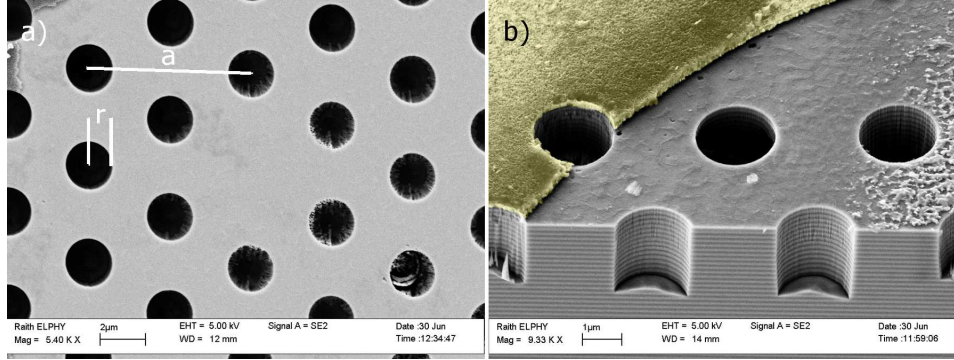


Figure 7.6: SEM images of integrated photonic crystal VCSEL. a) top down image with lattice parameters outlined and b) cross-sectional image with etch depth and VCSEL top ring-contact highlighted in yellow

using Xylene for 45 seconds, the pattern was transferred into the VCSEL mesa. The PhC was etched to a depth of approximately $1.6 \mu\text{m}$ (approximately 15 distributed Bragg reflector (DBR) mirror pairs) using chemically assisted ion beam etching and a similar etch recipe to that used for VCSEL mesa definition. The acceleration voltage was lowered to 350 V and the etch was carried out for 6 minutes (see figure 7.6b).

7.2.3 Photonic Crystal VCSEL Preliminary Results

The first set of devices were etched with a combination of single and double PhC defects (see figure 7.7). However, the VCSELs that were used did not operate correctly. Figure 7.7 shows near-field results for the device operating below threshold. Above threshold operation was not achieved. However, the required etching depths and resolutions were accomplished and it is believed that subsequent devices will work. Subsequent devices should then show single mode, out-of-phase operation. At this point the coupling interaction will be investigated. This will be achieved in a similar manner to [60] by changing the in-between defect hole radius. After this has been achieved a method for controlling the phase will be investigated, this will be achieved by “breaking” the top contact of the VCSEL. By electrically isolating the two defects continual phase control over the array should be achieved by differentially driving one defect over the other. Individual control over cavities in a coupled VCSEL design has been demonstrated by A.C. Lehman et al. in [61]. Using a proton implanted VCSEL design with three coupled cavities, individual cavity control has been shown. Direct control over steering direction has not been demonstrated, but control over cavity phase has.

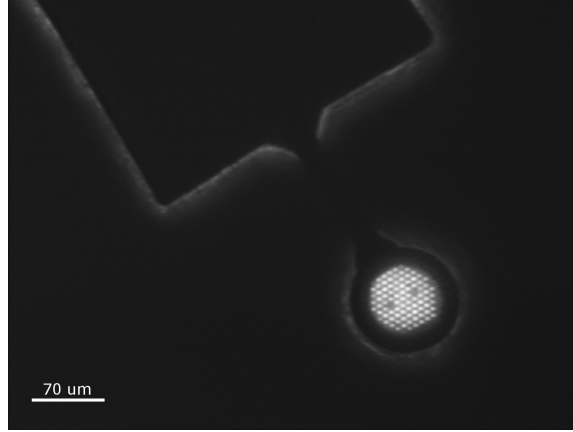


Figure 7.7: Microscope image of double-cavity photonic crystal VCSEL operating below laser threshold.

7.2.4 Macro Double-VCSEL Mesa Design

Nano-fabrication is not the only method to achieve coupling between VCSELs. Evanescent optical coupling is observed over a relatively large distance ($> 3 \mu\text{m}$ [61]). Therefore I have also designed a macro VCSEL array. To decrease the spacing between the VCSELs it is necessary to bring the mesas into physical contact. This meant that making the VCSELs into separate devices was difficult. To overcome this I used the selective oxidation process to shape the now larger double-VCSEL mesa's current/optical aperture. Oxidation proceeds roughly uniformly from all exposed side-walls, therefore to create two devices a VCSEL mesa with a thinner central region was designed.

Using this design the central region oxidised completely while the regions around it did not. This creates two separate un-oxidised regions within the one double-VCSEL mesa. These two un-oxidised regions form the two separate VCSELs. By changing the initial shape of the double-VCSEL mesa, control over the spacing between the two VCSELs can be achieved. A photomask with a number of double-VCSEL mesa designs was fabricated (figure 7.8a).

After a number of devices were built with these patterns, the “bow-tie” design was picked as the final shape. This shape allows better control over the coupling region than the other designs considered. A second mask with the “bow-tie” design was fabricated — figure 7.8b shows the core design of the mask. Each mesa pattern has a different coupling region. Horizontally the angle between the “bow-tie” wings is increased from 45° to 80° . This brings the two eventual oxide apertures closer together. Vertically the overlap between the two wings is increased from $5 \mu\text{m}$ to $30 \mu\text{m}$ giving a tolerance for oxidation purposes. Using this technique a standard ox-

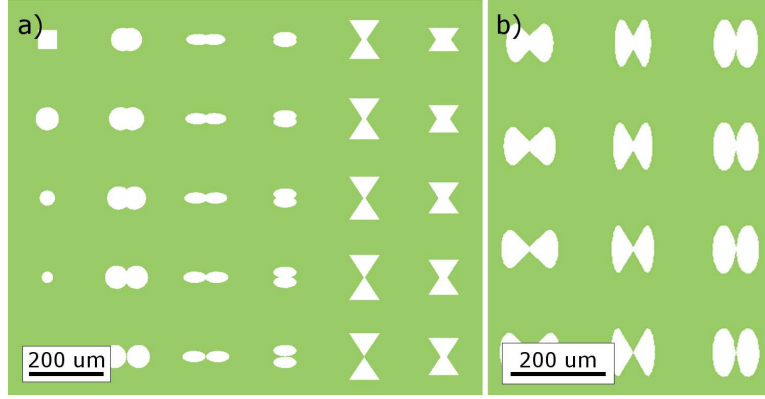


Figure 7.8: Graphical representation of the coupled VCSEL photomasks. The double-VCSEL mesa shape is designed to allow the oxidation process to create two separate but physically close VCSEL apertures.

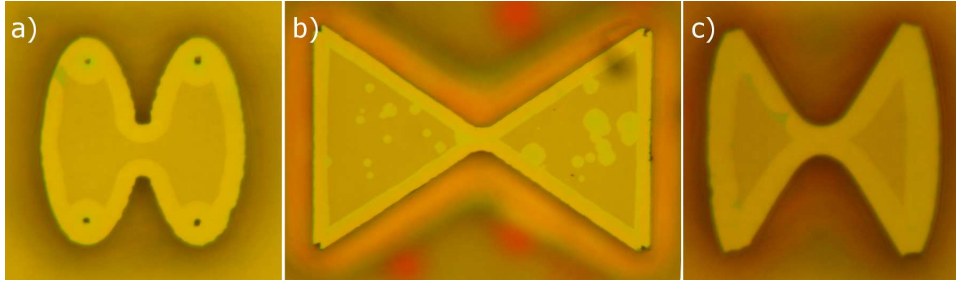


Figure 7.9: Three microscope images of oxidised double-VCSEL mesas, the aperture separation distance is seen to change with the mesa shape.

oxidation process produces coupled VCSELs that have completely separated apertures (small mesa overlap) and possible linked apertures (large overlap). This core pattern was then repeated over the mask with differing sizes of the double-mesa (largest mesas approximately $50 \times 50 \mu\text{m}$ and smallest approximately $20 \times 20 \mu\text{m}$). This allowed further control over the oxidation process, and allowed in one fabrication run the testing of a number of different coupling parameters.

7.2.5 Macro Double-VCSEL Mesa Fabrication

The coupled VCSELs were built using bottom emitting VCSEL wafers. This was done to allow for both a greater interaction distance for the VCSEL emission and for contacting the final devices. By varying the size of the double-VCSEL mesa the distance between the individual coupled VCSELs was also varied — this changes the coupling between the VCSELs and can eventually result in two separate (not coupled) devices.

Fabrication of a bottom emitting VCSEL is essentially the same as for a top emitting VCSEL. The ring contact is moved from the top to the bottom of the chip. Alignment of the bottom ring contact was alleviated by making one single large ring contact, surrounding the bottom of the whole chip. At first a single top contact was created across each double-VCSEL mesa. As such the coupled VCSELs were driven with a common current source. Once testing of these single-contact devices was completed, a second etch was performed to ‘break’ the top contact, making the individual VCSELs electrically separate. To separate the individual VCSELs an etch depth of over $1\text{ }\mu\text{m}$ was made into the top surface of the double-VCSEL mesa. By increasing this etch depth the resistance between the two VCSELs was increased, a resistance of $15\text{ k}\Omega$ being achieved.

The coupled VCSELs are probed using needle-probes. Owing to the size of the VCSELs, the top contacts can be damaged by the needle probes. This meant that once a device was tested it was sometimes impossible to use the device again. To alleviate this problem SU8 could be used to insulate the VCSEL mesas, by using SU8, larger contact pads could be used, allowing wire-bonding. This should make each device far more robust.

7.2.6 Macro Double-VCSEL Preliminary Results

To measure the coupled VCSELs, a horizontal probing station was set-up (see figure 7.10). The VCSEL chips were mounted vertically against a copper plate, which acted as a ground plane for the chips. The chips were placed at the focal point of a microscope objective lens for light collection. The emitted light was directed onto a silicon CCD camera and the images were recorded by computer. In order to probe the individual VCSELs, a 45° mirror was set-up beneath a stereoscope.

Common Top Contact Coupled VCSELs

The first set of coupled VCSELs employed a common top contact — this was used to replicate the work carried out in [52]. Although in [52] photonic crystal defects were used, coupling in the macro-VCSEL design should still be evident. The VCSELs were driven at differing drive currents and their far-field intensity patterns were recorded. At lower drive currents (just above laser threshold) in-phase operation was observed for some of the smaller devices (of the order $20\times 20\text{ }\mu\text{m}$ size) (see figure 7.11c). Figure 7.11 also shows results from the model discussed previously. The model shows that two in-phase coupled single-mode VCSELs, with apertures approximately $10\text{ }\mu\text{m}$ apart, produce a far-field pattern of similar extent to that

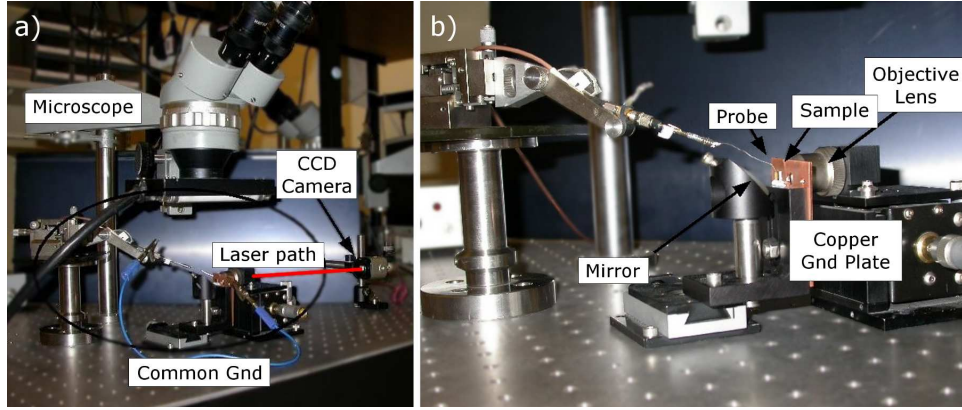


Figure 7.10: Photograph of experimental set-up for testing coupled VCSELs. a) the whole set-up including CCD camera, and b) close-up view of sample mounting stage and objective lens.

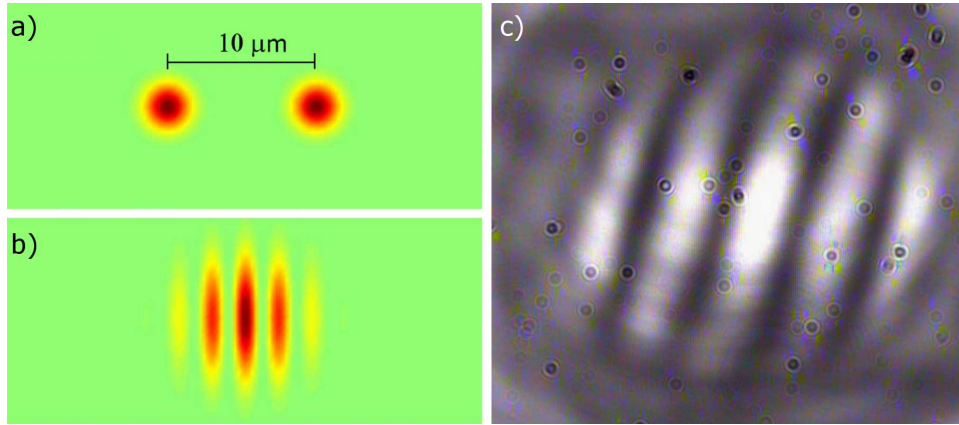


Figure 7.11: a) Near-field simulation results of two coupled VCSELs with an aperture-separation of $10\ \mu\text{m}$, b) Far-field simulation calculated from a) and c) CCD image of far-field from a fabricated double-VCSEL mesa.

shown by experiment. These experimental results only occurred at certain drive current configurations — leading me to believe that the coupled VCSEL was coming in and out of phase, as the drive current was increased. The fringe pattern observed in the far-field also changed with drive current — therefore I believe that the coupled-VCSEL moved from single-mode to multi-modal operation. These results were very promising. In-phase coupled operation had been observed, the next step was to control the phase of each VCSEL independently as such the next set of samples were given separate top contacts as described earlier.

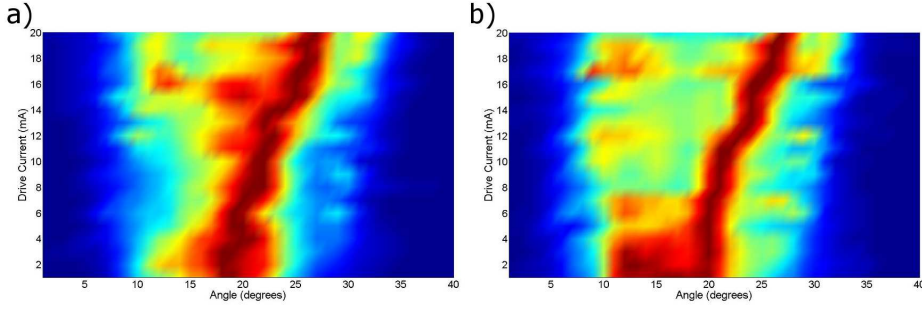


Figure 7.12: 2-Dimensional representation of far-field intensity distribution from coupled VCSEL with 10 μm mesa overlap (data taken using scanning photodetector set-up). The x-axis show angular information from 0° to 40° . The y-axis show second VCSEL drive current varied from 0 mA to 40 mA. Colour coding represents emitted intensity increasing from blue to red, a) first VCSEL held constant at 25 mA, b) first VCSEL held constant at 30 mA

Separate Top Contact Coupled VCSELs

In wanting to measure the angular extent of the far-field intensity distributions produced by the coupled VCSELs, I redesigned the experimental set-up. I removed the microscope objective and CCD camera and replaced them with a silicon photodetector mounted to a rotation arm. The axis of the rotation stage was centred below the emitting VCSEL, meaning the photodetector could be scanned in an arc around the emitting VCSEL. Figures 7.12 and 7.13 show some of the first results from this set-up. The graph shows the angle of the detector (about the optical axis of the VCSEL chip) against the drive current of one of the coupled VCSELs. In this experiment one VCSEL was kept at a constant drive current while the second VCSEL's drive current was increased. From these data, coupling and hence steering of the principal emission lobe is seen. From figure 7.12, as the drive current of the second VCSEL is increased from below threshold the phase difference between the two coupled VCSELs changes causing the emission lobe to shift in the positive angular direction. The first VCSEL is held constant above threshold at 25 mA (figure 7.12a) and 30 mA (figure 7.12b). Above and below these drive parameters the far-field is still seen to change with drive current, but not in such a prescribed manner. This experiment was also repeated while decreasing the drive current of VCSEL two — no hysteresis was observed and the far-field followed the same trend.

Figure 7.12 shows results from a $30 \times 30 \mu\text{m}$ double-VCSEL with a mesa overlap of 10 μm and a “bow-tie” wing angle of 45° . Figure 7.13 shows similar results to figure 7.12. These data were taken from a double-VCSEL with a mesa overlap of 20 μm and a “bow-tie” wing angle of 80° . Between these two VCSELs the coupling distance is expected to have increased and as such weaker coupling would be experienced.

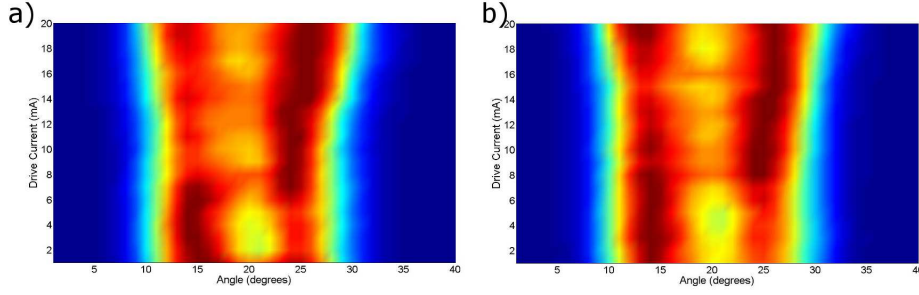


Figure 7.13: 2-Dimensional representation of far-field intensity distribution from coupled VCSEL with 20 μm mesa overlap (data taken using scanning photodetector set-up). Axial set-up as in figure 7.12 a) first VCSEL held constant at 25 mA, b) first VCSEL held constant at 30 mA

This seems to correspond to the results presented. Figure 7.13 shows coupling but the results are a lot more “washed-out” — the zero-intensities in the pattern are less defined.

This experiment looked very promising and coupling had been seen. However, the angular steering of the coupling did not match to what was expected. The two VCSELS involved in the experiment were approximately 5–10 μm apart. As mentioned at the start of this chapter the steering angle of a coupled VCSEL system is linked directly to the separation of the two emitters. The closer the emitters, the larger the steering angle. In a photonic crystal coupled VCSEL system, the greatest steering angle presented is approximately 5° [61]. This is possible with emitting apertures approximately 4 μm apart. In the experiment outlined above a steering angle of nearly 10° was seen. To confirm this I decided to take a series of 2-dimensional far-field patterns. I did this by reverting to the previous experimental set-up. However, instead of using a microscope objective, the CCD camera was placed as close as possible to the emitting surface of the VCSEL. Figure 7.14 shows preliminary results from this experimental set-up.

Figure 7.14a shows a number of cross-sectional cuts through the far-field pattern as the drive current of the second VCSEL is increased. From these data it became clear that what was thought to be pure 2-dimensional steering was in fact a far more complex multi-modal coupling property. Figure 7.14b shows a composite graph taken from the 2-dimensional far-field images. The sections are taken through the centre of the far-field in both the x- and y-direction. As can be seen from figure 7.14b this is in fact what was being seen in the first experiment. The scanning photodetector was sampling only a small section of the far-field pattern.

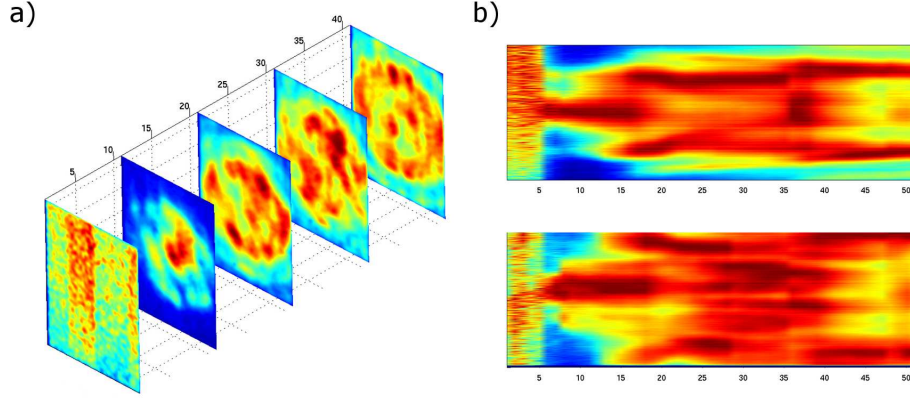


Figure 7.14: a) Far-field intensity distribution images from a coupled VCSEL (taken using a silicon CCD camera). VCSEL 1 driven at 2 mA, VCSEL 2 driven from 12–22 mA in steps of 0.2 mA, and b) 2-dimensional interpretation of data from a), showing comparable results to previous experiments.

7.2.7 Conclusions

In conclusion, photonic crystal coupled VCSELs are very interesting and can be taken to results quite straight-forwardly. Unfortunately the time allocated for this work ran out and further results could not be achieved. However, I believe that there is a lot that could be done with this approach. The investigation of multiple cavities should achieve steering and beam divergence control. Looking at asymmetric coupled cavities could also be interesting. By making one cavity larger than the other, far-field intensity distributions with a single lobe should be achieved along with steering. Asymmetric cavities could solve the differential intensity challenge. This arises from the phase control mechanism — to change the phase of a cavity it is necessary to drive the cavity harder, however, this results in one cavity emitting more light than the other. This tends to diminish the resulting steered far-field pattern. By making the cavities different sizes this intensity mis-match could be circumvented. It can be imagined that “daisy” configurations of cavities could be used — the central large cavity providing most of the emitted power while the surrounding smaller cavities providing steering and beam divergence control. Photonic crystal cavities could also be used to look at the multi-modal behaviour of coupled cavities. Single mode operation in a photonic crystal is relatively easy to engineer as would be double- or higher-modal operation.

The macro-mesa coupled VCSEL design as mentioned is far more complex than first thought. However, this is certainly not a negative, although the work could not be completed within the frame-work of this thesis, the results from the 2-dimensional far-field measurements pointed to looking at this system in terms of its multi-modal

properties. Many people have begun to look at this area (i.e. multi-transverse mode dynamics within VCSELs under drive current modulation) [62, 63, 64, 65, 66, 67, 68]. The future aim would, therefore, be to link the known shape of the VCSEL mesa to its far-field emission pattern. As mentioned above, the coupled multi-modal system does not suffer from hysteresis and the results are repeatable (i.e. the mode shapes and directions are the same each time the device is driven). Therefore when the modal shape can be predicted, tailoring of the VCSEL mesa shape will yield a steerable emitter array.

Chapter 8

SpeckNet Optical Transceiver Integration

8.1 Introduction

This chapter outlines the work carried out on integrating the Speck's optical transmitter with the SpeckNet platform.

8.2 The Photodetector

The basic semiconductor photodetector is based on a p-n junction operated in either reverse bias (i.e. photoconductive) or more like a solar cell without bias (i.e. photovoltaic). The key properties of a detector are:

- Responsivity — this is a measure of a detector's ability to convert incoming light into outgoing photocurrent. It is measured in A/W and varies with incident wavelength.
- Shunt Resistance — this is the internal resistance of a detector. The larger this resistance the more photocurrent is seen across the photodetectors load resistance. Therefore the shunt resistance is linked to the efficiency of a detector.
- Capacitance — the internal capacitance of a detector along with any circuit capacitances effectively determines the detector's speed. The lower the capacitance the quicker the detector can respond to a signal change. This can be reduced by using a reverse bias.

Properties	Hamamatsu S2387-66R	Osram (LED form) SFH 203 FA	Osram (flat) BPW 34 FA	Sharp PD410PI
Responsivity (A.W ⁻¹)	0.58 at 960 nm	0.59 at 850 nm	0.65 at 880 nm	1.00 at 1000 nm
Capacitance (pF)	4300 at 10 kHz	11 at 1 MHz	72 at 1 MHz	20 at 1 M Hz
Shunt Resistance (GΩ)	10	4	0.33	1
Acceptance Angle (degrees)	≈120	40	120	90
Effective Area (mm ²)	33	1	7	-

Table 8.1: Table of off-the-shelf silicon detectors and their characteristic properties.

- Effective area — the effective area of a detector is a measure of its light capturing capabilities. It is not necessarily a measure of the physical size of the device. Lenses can be used to increase a detector's effective area.
- Acceptance angle — although this is not as important as the previous properties, within a Speck it would be. By increasing the acceptance angle of a detector, the number of detectors required is minimised, making the overall Speck size smaller and less complex.

For the Speck, a detector with a high response, low capacitance, high shunt resistance and small physical area is desirable. A number of silicon based photodetectors were investigated for integration with the Speck. The properties of these are outlined in table 8.1.

The Hamamatsu detector [69] has a good responsivity and a good shunt resistance. It is also placed in a flat package giving it a good acceptance angle. However, its capacitance is quite large (rise-time of 10 μ s i.e. 0.1 MHz response). Both of the Osram detectors [70, 71] have equally good responsivities and are much smaller devices, making their capacitances lower and as such they are fast (both quoted with a rise- and fall-time of less than 20 ns i.e. greater than 50 MHz response). The Osram BPW 34 FA has an acceptance angle of 120 degrees — this detector seems a good choice. Unfortunately the Osram devices have low shunt resistances making them inefficient compared to the Hamamatsu detector. The Sharp detector [72], has the best quoted responsivity (quoted at the detector's peak sensitivity of 1000 nm (see figure 8.3)), one of the lowest capacitances and a good acceptance angle. Its shunt resistance is low, however, due to its other properties it was chosen as the first integrated silicon detector (see figure 8.8b).

Silicon has a band-gap energy of 1.1 eV, which means that light with an energy greater than this (i.e. below a wavelength of 1.11 μ m) is detected. This is a good thing for devices such as solar cells, where as much light as possible can be collected.

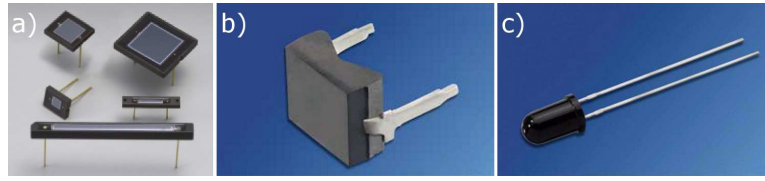


Figure 8.1: Photographs of the silicon detectors evaluated, a) Hamamatsu [69], b) Osram (flat) [70] and c) Osram (LED) [71].

However, the signal produced by my VCSELs is only at a wavelength of 980 nm. This means that all other wavelengths of light contribute to the background-light level. Therefore, one method to improve the efficiency of a SpeckNet detector is to use an optical filter. By limiting the light falling on to the detector the background-light level can be reduced.

The Osram and Sharp detectors include integrated “day-filters”, made from a semi-opaque polymer (see figure 8.1). The polymer is designed to block shorter wavelength radiation. Figure 8.3 shows the normalised spectral response of the silicon detectors presented. Included in the figure is the spectral response of our VCSELs. Each detector has a good response for our VCSEL emission, but their response is a lot broader. Figure 8.2 shows the typical background-light spectrum that these detectors will have to contend with. Light from the sun and fluorescent tubes is prevalent at the shorter wavelengths, and as the day filtered detectors will have a better background-light suppression ratio than the non-filtered Hamamatsu device. The background-light suppression ratio is the ratio between the wanted signal and any form of noise that corrupts the signal. Signals seen in a circuit connected to a photodetector include: photocurrent, thermal (Johnson-Nyquist) noise of the load resistor, shot noise of dark current and shot noise of the photocurrent. Of these signals the only one of interest is the photocurrent. All others are sources of noise reducing the detectors background-light suppression ratio. The photocurrent shot noise can be limited by limiting the amount of light incident on the detector. The “day-filters” of the Osram and Sharp detectors do this by limiting un-wanted light from generating photocurrent. The dark current and hence the dark current shot noise can be reduced by lowering the reverse bias or running the detector photovoltaic (i.e. with no reverse bias). The thermal noise can be limited by reducing the size of the load resistors used in the detection circuitry.

Figure 8.6 shows the response of the Hamamatsu and Osram detectors to a VCSEL signal as the signal strength is reduced by moving the detector away. The graph also highlights the background-light levels. Once the signal is below this level it becomes far more difficult to recover. The data shown in figure 8.6 was taken using three of

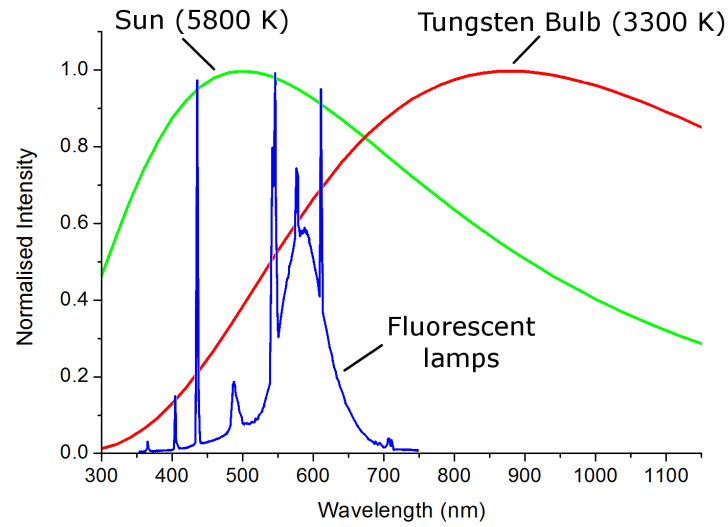


Figure 8.2: Normalised (to maximum of each spectrum) graph of background-light affecting detectors placed outside and inside under typical office lighting.

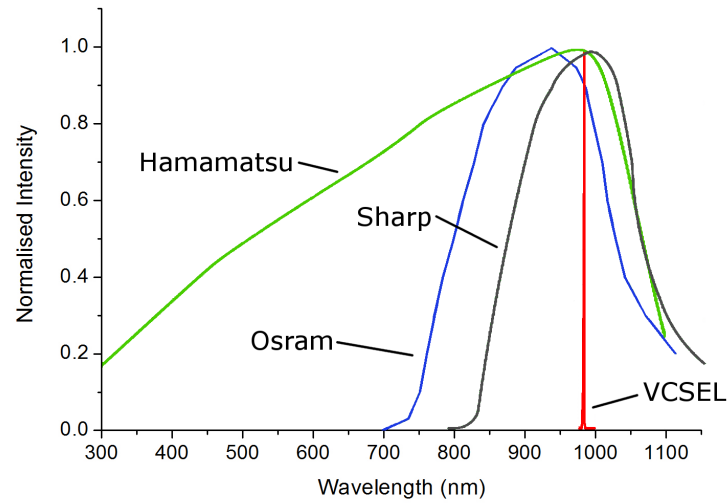


Figure 8.3: Normalised (to each detector's maximum response) graph of the silicon detectors' responsivity. Included is the spectrum of our VCSEL.

the detectors. To remove the influence the size of the detector has, a fixed aperture was placed on top of each detector. It is important to not saturate the detector. Saturation occurs when the detector is at its photocurrent producing limit. Once this point has been reached any additional signal is completely and irretrievably lost. To keep the detectors below saturation it is important to use good optical filtering. As can be seen in figure 8.3 the “day-filters” block a lot of light, however, the detectors could be further filtered. To accomplish this I investigated the use of the VCSEL material as a detector.

8.3 The Resonant Cavity Detector

Because the VCSEL material emits at 980 nm, it will also absorb at 980 nm. By building a suitable device it was possible to use the VCSEL material as a perfectly matched photodetector for the optical transceiver. To increase the light absorbing area of the resonant cavity detector, the mesa size was increased to a range of 200x200 μm to 1000x1000 μm . In order to isolate each detector from the bulk VCSEL material a 6 μm deep channel was etched around each detector mesa (using the same etching protocol as for VCSEL fabrication). The samples were then contacted with a common bottom contact and a grid-configuration top contact (see figure 8.4).

As the top of the VCSEL wafer consists of a DBR mirror, the acceptance angle of the first resonant cavity detectors was limited to approximately 20 degrees. To increase this angle the top surface of the resonant cavity detectors was etched, removing approximately 10 mirror pairs. This increased the acceptance angle to 40 degrees.

By using multiple detectors made in this fashion and integrating beam control devices onto the receiving surface, this detector looked like a good choice for the final design. Figure 8.5 shows the spectral response of the integrated resonant cavity detector along with the emission line of the VCSEL. The two spectra match and, due to the shape of the detector’s response, the background-light levels (from other wavelengths) are very low. Figure 8.6 shows the performance of the resonant cavity detector compared to the silicon detectors, although the photocurrent signal from the resonant cavity detector is lower than the silicon, the background light saturation point is much lower. This is due to the filtering properties of the VCSEL material. Figure 8.7 shows the acceptance angle of the integrated resonant cavity detector as the top surface is etched away. The acceptance angle is increased to 44 degrees with an etch depth of 1.2 μm — after this point little improvement is seen with increased etch depth.

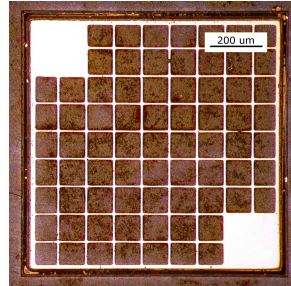


Figure 8.4: Microscope photograph of the resonant cavity detector, with a grid top contact.

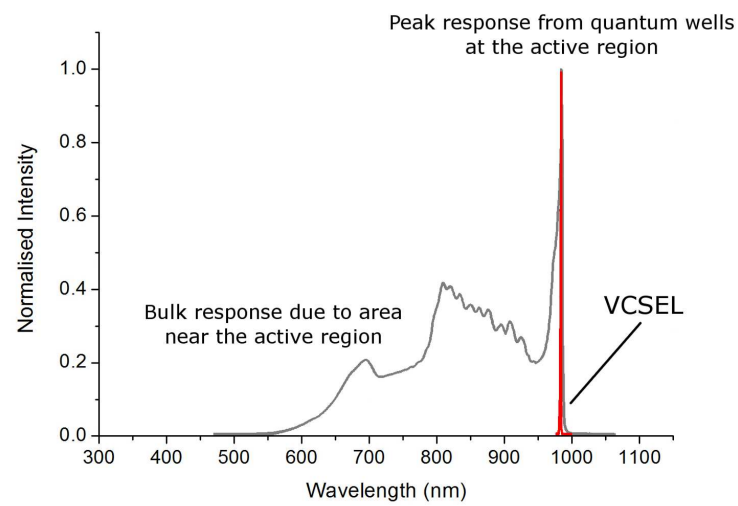


Figure 8.5: Normalised (to each detectors maximum response) graph of the resonant cavity detector sensitivity, included is the spectral response of the VCSEL.

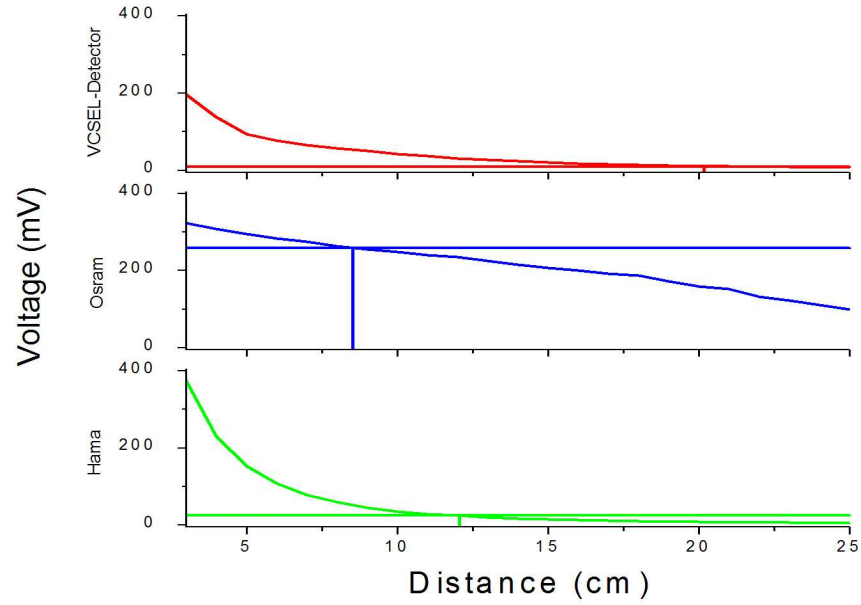


Figure 8.6: Graphs of silicon and resonant cavity detector response with increasing emitter-detector distance. Highlighted is the detector background light saturation point.

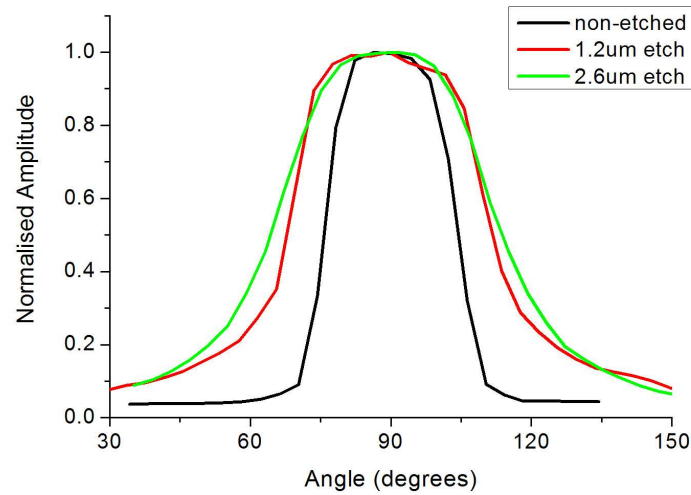


Figure 8.7: Graph of angular response of the resonant cavity detector. By etching away the top DBR, the reception angle of the detector is increased to a maximum of 50 degrees.

Properties	Hamamatsu S2387-66R	Osram (LED form) SFH 203 FA	Osram (flat) BPW 34 FA	Sharp PD410PI	Resonant Cavity Detector
Responsivity (A.W^{-1})	0.58	0.59	0.65	1.00	0.08
Capacitance (pF)	4300	11	72	20	400
Shunt Resistance ($\text{G}\Omega$)	10	4	0.33	1	0.008
Acceptance Angle (degrees)	-	40	120	90	45
Effective Area (mm^2)	33	1	7	-	1

Table 8.2: Reproduction of table 8.1 with integrated resonant cavity detector added for comparison.

The resonant cavity detector was a good choice for the final integrated optical transceiver. As it is made from the same material as the VCSELs themselves, arrays of both emitters and detectors can be built on the same chip. The fabrication process for the detector is also very similar to the VCSEL, the full transceiver array can be made in one run. This all aids in achieving the final goal — an all optical ultra-compact communication system for the SpeckNet platform.

The VCSEL material has a very small gain volume, made of a few quantum wells. This gain volume is responsible for the absorption of light when used as a detector. As such the responsivity of the resonant cavity detectors is quite low (see table 8.2). Because the VCSEL material was designed as an emitter rather than a detector the internal resistances and capacitances were not optimised, therefore the resonant cavity detector is also quite slow. All this said the resonant cavity detectors, because of their matched nature, suffered from very little background-light, therefore the final optical transceiver included both VCSELs and resonant cavity detectors, in one chip.

8.4 Packaging

Packaging is essential as a first step towards an integrated SpeckNet platform. There were a few things that a package has to achieve. The contacts of the package had to be relatively large and their position had to be standardised. It also had to make the transceivers robust. The first form of packaging investigated was a simple bread-board circuit, which did not provide protection to the VCSEL chip but allowed the sample to be tested using macro-components such as crocodile-clips. The second type of packaging used was the dual in-line package (DIP). I chose a 16-pin version as this allowed enough connections for both the VCSEL array and detectors (figure 8.8).

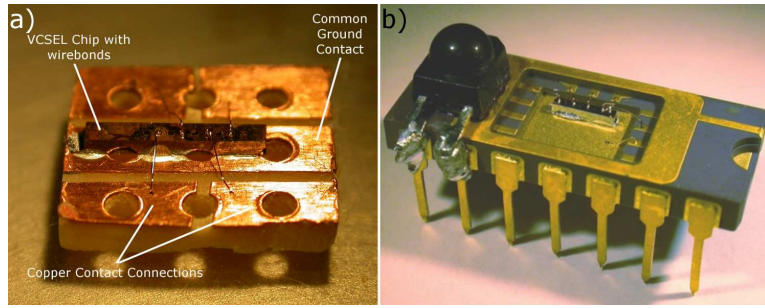


Figure 8.8: a) Photograph of first packaging solution using breadboard circuit and b) DIP packaging solution with Sharp detector.

8.4.1 Wire-bonding

Wire-bonding was used to effectively replicate the needle probes used within the laboratory. Wire-bonding, in this case, uses very fine golden wire to make interconnections between integrated circuits and printed circuit boards. A Kulicke & Soffa Model 4124 Universal Ball Bonder was used during this work. This machine uses both ball and wedge bonding. The wire, during operation, is fed through a capillary and held in place with a clamp. The ball is made by melting the tip of the gold wire as it protrudes from the capillary. This ball is then brought into contact with the sample and mechanical force, heat and ultrasonic energy are applied to weld the ball in place. The armature of the wire-bonder is then moved to the second bond area (leaving a trail of gold wire) where the same welding process is performed. This part of the bond does not use a ball, instead a wedge is created at the second connection point. Once this procedure is complete the wire-bonder resets by lifting the armature away from the sample and making a new ball ready for the next wire-bond (see figures 8.9 and 8.10).

Each of the parts above can be controlled separately. The mechanical and ultrasonic force can be altered separately for each step (ball bond and wedge bond). Heating is accomplished by heating the sample mounting stage, and is the same for each step. A few things are needed from the sample in order to perform a good wire-bond. The contact pad material must be chosen to work with the wire-bond material. I used both gold wire and gold contact pads as it shows the greatest wire-bond reliability [73]. The substrate that the contact sits upon must also be mechanically stable and stiff. This caused a problem initially. The SU8 used as an insulator is not stiff (especially when heated to the wire-bond temperature of 150 °C, as such the ultrasonic energy applied during a wire-bond dissipates and the wire-bond fails.

To overcome this I began by removing the SU8 insulation layer. To stop the VCSEL short-circuiting through the bulk material, I etched the contact pad area to

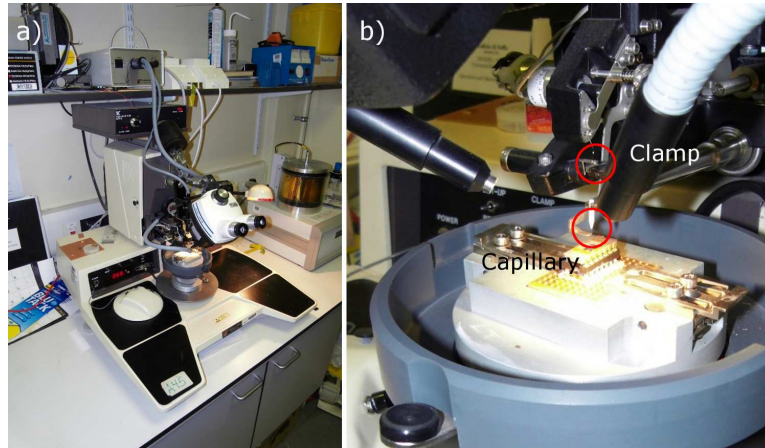


Figure 8.9: Photographs of the wire-bond machine used for this work, a) full image, b) close up of bonding armature (highlighted are the capillary and clamp).

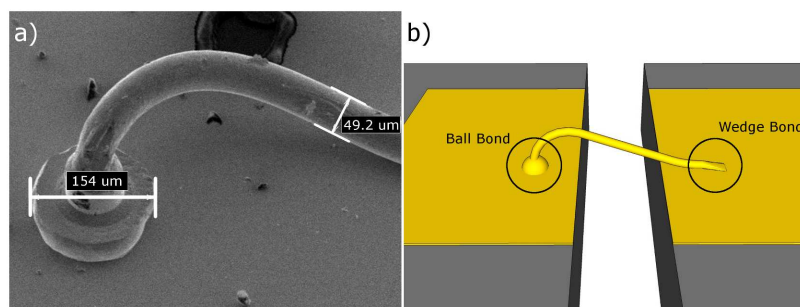


Figure 8.10: a) SEM image of wire-bond, b) Illustration of complete wire-bond including both ball and wedge.

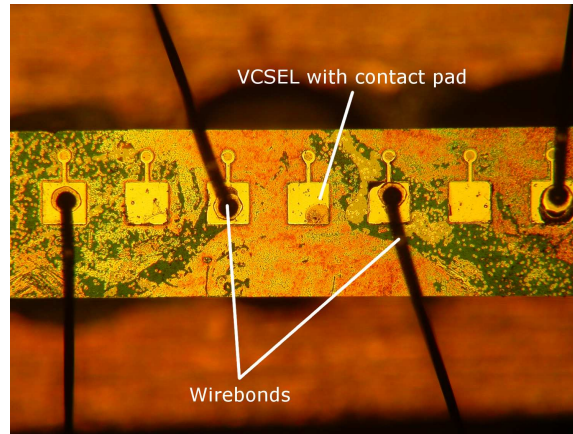


Figure 8.11: Microscope image of first wire-bonded VCSEL arrays, highlighted are the wire-bonds and the VCSEL contact pads.

the same depth as the VCSEL mesa (see figure 8.11). This created large extended mesas that could not lase (due to their size). These contact mesas were connected to the VCSEL via a thin ridge. During oxidation the ridge oxidised completely. This isolated the VCSEL mesa from the contact pad, allowing the VCSEL to lase. This was a far from ideal solution — due to the large mesas the resistance of the lasers increased making the first fully integrated VCSEL chips inefficient (see figure 8.11). Even though these lasers were inefficient they served as good prototype devices for use by Edinburgh University. This allowed Edinburgh to design and start building circuitry that would be reused with newer devices.

After further investigation a technique for wire-bonding to SU8 was found [73]. First the hard-bake time and temperature for the SU8 were increased to 30 minutes at 200 °C. The SU8 was then etched to roughen the surface. This is done in an oxygen plasma at a power of 80 watts. This is performed for at least 10 minutes, however, longer can be used if thinning of the SU8 is also required. The top contact material is also altered from nickel and gold, to chromium and gold (i.e. 50 nm Cr, 200 nm Au). The chromium is used for its adhesive properties. It remains attached to the SU8 at much higher strain levels than nickel. This technique allowed wire-bonding to contacts placed on top of SU8 (see figure 8.12a). Figure 8.12b shows one of the final design transceivers that were given to Edinburgh for integration purposes.

8.5 Integration with the Speck

Once packaging had been arranged along with the wire-bonding, the transceiver arrays (VCSELs including detectors) were given to Edinburgh University for use

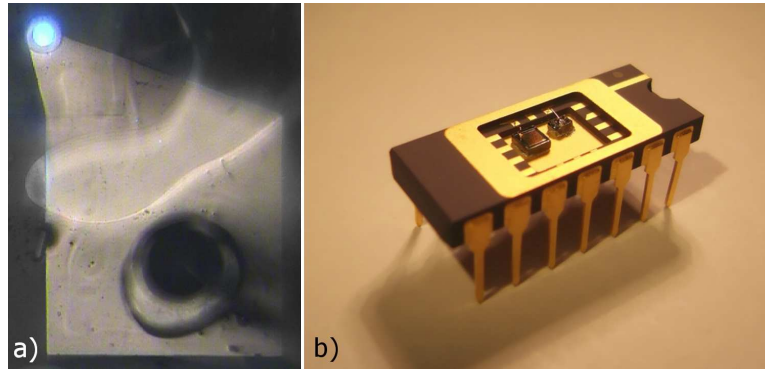


Figure 8.12: a) Microscope image of second generation wire-bonded VCSEL and b) All optical transceiver array including VCSEL array and resonant cavity detector.

in the SpeckNet platform. The group at Edinburgh include both computer scientists and electronic engineers. They began by designing circuits for driving and detecting optical signals. Driving of the VCSELs is straight-forward as the VCSELs have low thresholds and operating voltages below 5 volts. Therefore the VCSELs are driven directly by the Speck digital output ports. The detecting circuitry is more complicated. Due to the low signal level received from the VCSEL, amplification, as well as frequency filtering, is employed. To communicate information the Speck modulates its signals at a rate of approximately 4 kHz (at 4 kiloBaud). This signal has to be far away from the noisy 50–200 Hz area where AC signals are found.

Following figure 8.13, the low level signal (photocurrent) from the detector (PD) is first amplified (including any DC signals). This is then buffered using a voltage follower and split into two. One part is low pass filtered to select the DC component — this part and the un-filtered second part are applied to an operational amplifier (op-amp). The op-amp outputs an amplified version of the difference between the two inputs, effectively removing the DC signal. This AC-coupled signal is then chopped to produce a square-wave signal for digital processing. This is achieved by low pass filtering one part of the AC signal to find the average DC level. This level is then used in a comparison operation with the original amplified AC signal using a further op-amp. The receiving circuitry consists of three stages, a pre-amplification stage, an AC-coupling and further amplification stage and a final chopper stage.

In optimising this design, it was found that the receiving circuitry could be made very low power 40–60 μA when amplifying a 1 kHz signal and 30 μA when static (at a voltage of 2.7 V). This in turn means that the detector can be left “on” permanently, without overly draining the Specks’ power reserves. This is a very useful fact. In standard receiving circuitry (such as used by a radio based solution) the detector consumes far too much power to be left “on”. As such the receiver is

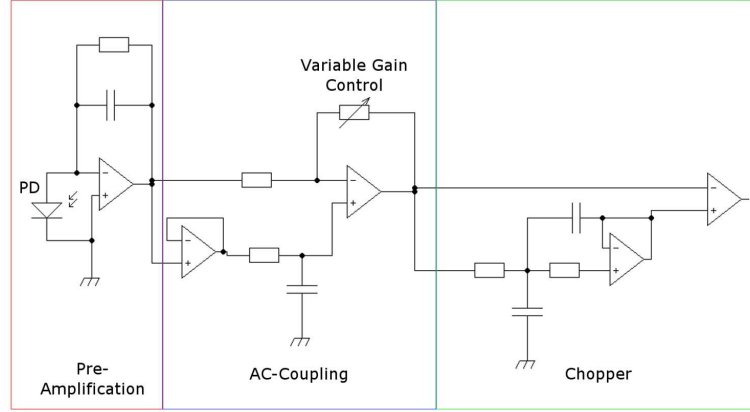


Figure 8.13: Schematic of the detector circuitry, highlighted are the pre-amplifier stage, the AC-coupling and chopper stage.

only powered up when a signal is expected to be received. This causes overheads within the system. Knowing when to turn a receiver on is a difficult task to achieve. Synchronisation between the sender and receiver costs a relatively large amount of power. Either a signal has to be repeated until a confirmation reply is received. Or a more centralised system must attempt to synchronise the network. By removing the synchronisation requirement, more power is freed for the transmission side of communication. This in turn increases the communication distance achievable.

It was found that, using the detector circuitry (see figure 8.13) along with the resonant cavity detector, an optical signal measuring -80 dBm at the detector could be amplified and used within the Speck. Assuming that a single-mode VCSEL (i.e. emitting a Gaussian beam) can be employed in the optical emitter array (this is possible with the VCSELs built during this work), the power at an aperture, of radius r , at a distance from the source z can be calculated using:

$$P(r, z) = P_0 \left[1 - e^{\frac{-2r^2}{\omega^2(z)}} \right] \quad (8.1)$$

Where P_0 is the power emitted and $\omega(z)$ is the beam width at a distance of z . $\omega(z)$ can be calculated using:

$$\omega(z) = \omega_0 \sqrt{1 + \left(\frac{z}{z_R} \right)^2} \quad (8.2)$$

Where ω_0 is the Gaussian beam waist size (minimum beam width) and z_R is the Rayleigh range of the beam. z_R can be calculated using:

$$z_R = \frac{\pi \omega_0^2}{\lambda} \quad (8.3)$$

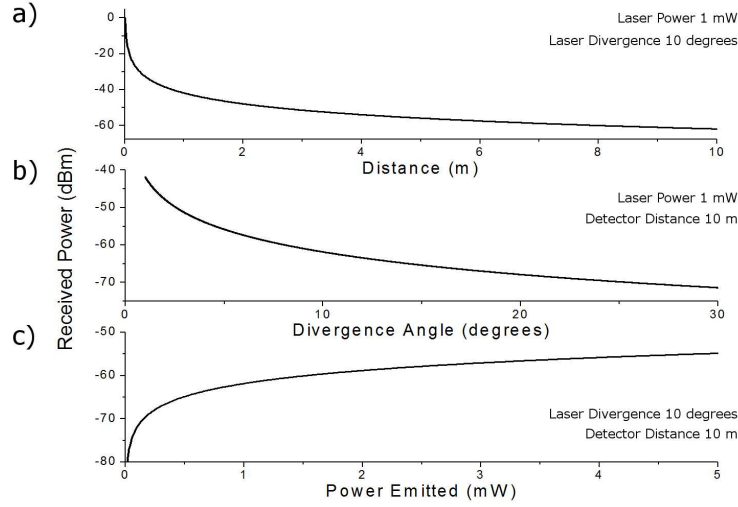


Figure 8.14: Graphs of power received at a 1 mm diameter detector from a source of varied power and divergence angle.

Where λ is the wavelength of the radiation under consideration. Because the beam waist is not important here, I have calculated ω_0 from the divergence angle (θ):

$$\omega_0 \simeq \frac{\lambda}{\pi\theta} \quad (8.4)$$

By modeling these equations a number of graphs can be produced that show how an optical communication system will work in a real world situation (see figure 8.14).

Figure 8.14a shows that a 1 mm diameter detector will receive greater than -60 dBm of optical power from a 1 mW source of 980 nm radiation (i.e. the VCSEL) with a divergence of 10 degrees, within a distance of 10 metres. The Speck detector and circuitry requires an optical signal strength of greater than -80 dBm. Figure 8.14b shows the relationship between the above emitter and receiver with a varying emitter divergence. With a divergence of 30 degrees the receiver picks-up greater than -70 dBm. A typical fabricated VCSEL has a divergence of less than 20 degrees. The third part of the figure, figure 8.14c shows the amount of emitted power required for a certain reception power for the above arrangement. This shows that, in theory, an emitter with a power of 20 μ W would supply enough energy to the detector at 10 metres distance.

To test the optical transceivers the Edinburgh group began by “breadboarding” an electronic circuit (figure 8.15). From this circuit power consumptions of the individual components could be measured, from figure 8.15a a current consumption of 43.5 μ A for the optical receiver circuitry is observed. Once low power amplifica-

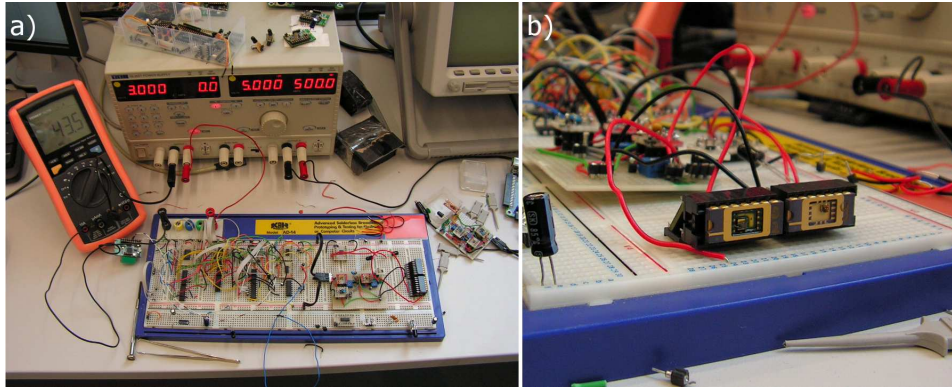


Figure 8.15: Photograph of “breadboard” electronics for control of the Speck optical transceiver. a) showing the current consumption of the optical receiver to be $43.5 \mu\text{A}$ and b) showing close-up image of packaged transceiver.

tion circuits had been designed and built they were ported onto the Speck platform (figure 8.16). Figure 8.16 shows two optical Specks transmitting and receiving data (the transmitted photo can be seen on the computer screen within the photo). The Specks are linked to the base computer for capturing and displaying the intended transmission data. Along side these tests, location discovery algorithms were implemented onto the Speck platform. To test optical location discovery the Edinburgh group made use of the PerSpeckz platform (figure 8.17). This platform consists of 64 individual Specks, each Speck is mounted in a grid formation and powered from a central source. Removing the need for battery replacement during testing. Initial optical location discovery tests were undertaken using off-the-shelf components (figure 8.18), however, once testing of my optical transceivers is complete they will be integrated into the location discovery test-bed.

8.6 Conclusions

In conclusion, a number of detectors were investigated for use in the SpeckNet platform. Silicon photodetectors were looked at and found to have fast response times and high responsivities. They can also be very efficient. However, silicon detectors are sensitive to a large spectral bandwidth which creates a lot of unnecessary noise. Silicon detectors with integrated “day-filters” were also investigated. These showed an improvement over the unfiltered detectors but still suffered from a relatively large spectral bandwidth.

The VCSEL material was investigated, for use as a detector. Detectors were built using the same processes as for VCSEL fabrication. It was found that the spectral

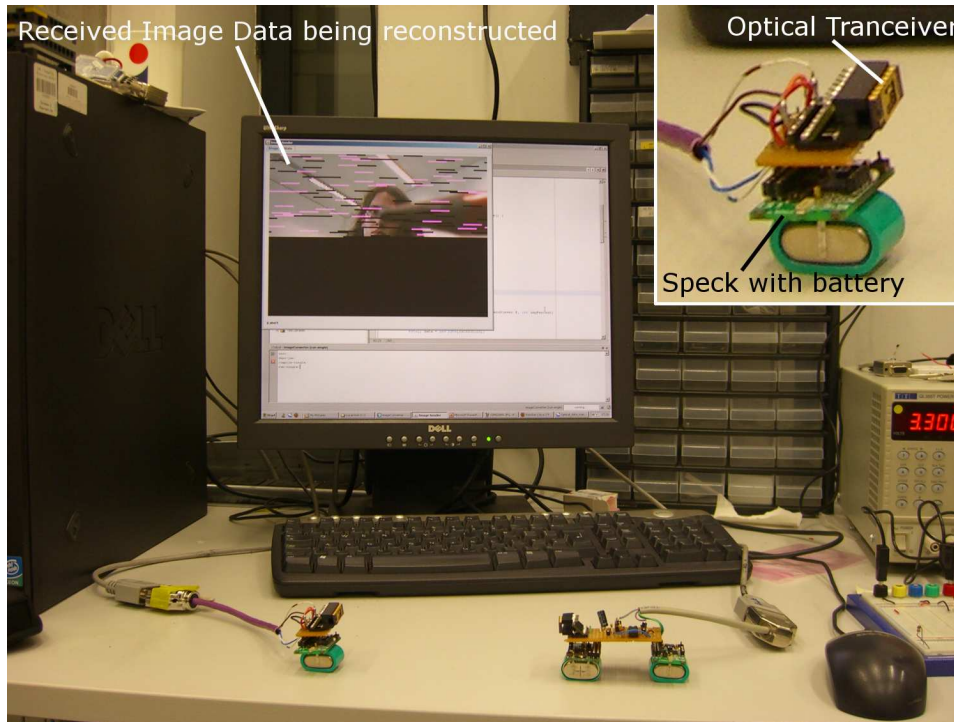


Figure 8.16: Photograph of two optical Specks transmitting a colour photograph taken from a web-cam. Inset shows close-up image of Speck with optical transceiver.

bandwidth of the resonant cavity detectors was very good. They almost completely rejected radiation away from the VCSEL emission line. However, the VCSEL material is not designed for detection, so the responsivity, speed and efficiency of the resonant cavity detectors was quite low. Fortunately, due to the nature of the Speck platform, the speed of the integrated detectors is not important.

It was found, after the transceivers were integrated with the Speck platform that due to the resonant cavity detectors ability to reject background light, the Specks employing the resonant cavity detector could operate with their detecting circuits permanently powered. This in turn lowered the complexity of the final Speck solution as there is no longer any requirement for synchronisation. Using a simple Gaussian beam propagation model it is estimated that an emitter (using less than 1 mW power) is capable of transmitting over 10 metres using the optical transceiver, designed during this work. The best emitters built during this project emit more than 2 mW, with the sub-optimal emitters still emitting 100s of μW . The initial aim of the project was to construct an all optical communication system for the SpeckNet platform, with these results this has been accomplished.

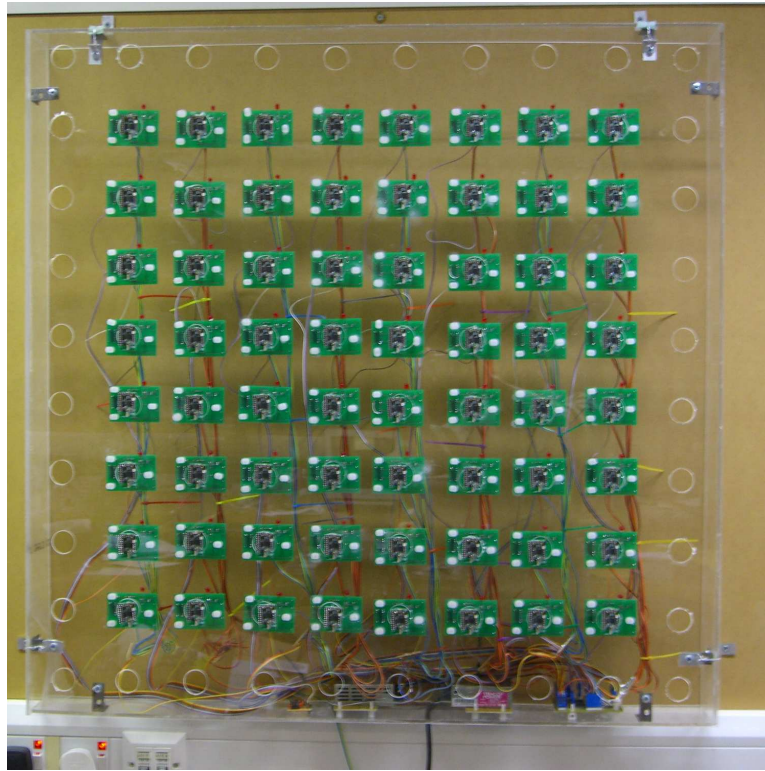


Figure 8.17: Photograph of the PerSpeckz test platform. PerSpeckz consists of 64 individual Specks each powered from a central source.

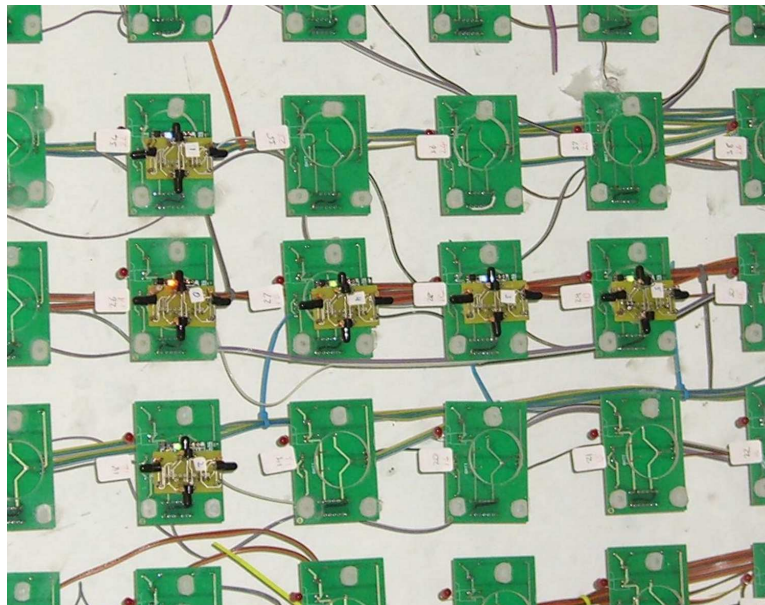


Figure 8.18: Photograph of the PerSpeckz test platform with 6 optical Specks. Each Speck uses 4 off-the-shelf LEDs and detectors in order to perform location discovery.

Chapter 9

Conclusions

When I began this work, the SpeckNet collaboration was only a number of months old. It had radio, electronics, systems/software and signal processing groups. With my joining the group, optical communications was added. At this time I was also new to the research group in St Andrews. This group worked in the micro-fabrication area and had a lot of background in semiconductor processing. This was very useful to me as I decided early on to work with the vertical-cavity top-emitting laser (VCSEL) as an emitting source. However, the group had little to no experience with top-emitting lasers. As this thesis has outlined, my project centred around free-space optical beam control. I chose to pursue a number of techniques to accomplish this, only some of which had been investigated by the research group before. The research group mainly worked with telecommunication devices, meaning that the wavelength of interest for me, namely 980 nm, had not been used before. This was of little consequence, however, as I had to set-up a new laboratory including equipment for this SpeckNet work. The final goal of my project was to fabricate, test and deliver an optical transceiver system for the SpeckNet collaboration. To accomplish this, packaging had to be looked at, which had not been looked at within the group before (although a wire-bonding system was available for use). Therefore the state of my project when I began this work was almost non-existent.

Now that I have worked on this project for a number of years, things are a lot different. I have developed a VCSEL fabrication protocol, including etching recipes and fabrication techniques that keep the sample viable right through to testing (i.e. top emitting devices must be kept clean as their top surface is optically polished, unlike edge emitters where a cleaved facet is used as an output coupler). VCSEL yield is also above 90%, which is important when arrays of emitters are required. VCSELs with output powers greater than 2 mW with thresholds below 400 μ A have been achieved. I have also developed a number of promising beam control techniques. Liquid crystals have been looked at as a solution (producing a steering angle of

1 degree) and although found not practical for this work could be used in other projects (i.e. the fabrication protocols have been optimised and will aid in further work). Micro-prisms, have been fabricated using greyscale lithography, a new technique (to the group). They have been shown to give a beam steering angle of 10 degrees over an array of VCSELs. This technique has been analysed and I believe can be extended by moving to a larger e-beam writing machine.

A number of different grating configurations have been investigated. Starting with an angled grating design, beam steering has been observed (to an angle of approximately 30 degrees into the first diffractive order, of the grating) with good efficiency. The approach was fabrication intensive and was not used further. However, a lot was learned from going through this investigation. Angled gratings were found to be an elegant solution to high-efficiency beam steering, leading me to the sub-wavelength grating. These have been simulated and should be extremely efficient. Sub-wavelength gratings have been fabricated and have allowed me to push the fabrication limits of the machines used in this work. Sub-wavelength gratings are at such a position that steerable VCSEL arrays could be realised (using this technique) in the very near future. The etching and EBL protocols that have been put together in this work are now finding use in other projects within the research group. Coupling of VCSELs using both photonic crystal (PhC) defects and macro-double-mesa designs have also been looked at. Photonic crystal defects were found to be very promising. The preliminary work I carried out in this area has made the realisation of fully-working PhC VCSELs imminent. The double-mesa work has shown that it is the multi-modal behaviour of the VCSELs more than the direct coupling of the optical fields, that can be used for beam control. Making this work very interesting for further investigation. This type of work is finding a lot of interest around the world at the moment. With what has already been accomplished within this project a contribution to this area of research could be made in the future.

I have also looked at detectors within this project. This was never a driving force behind the work but was necessary once an optical emitter array was achieved. I looked at a number of silicon devices and found that they were very good but that they suffered from background noise. Optical filtering did not help this situation enough to make silicon detectors viable for the SpeckNet platform. To improve VCSEL detection I looked at using the VCSEL material as a detector. By building suitable detection devices (i.e. of large areas, using grid-configuration contacts) I was able to integrate detectors along with emitters on the same semiconductor chip. Due to the DBR and material that the VCSEL is made from, it was found that the background noise levels when using a resonant cavity detector were almost non-existent. This allows the detectors (and their circuitry) to be left “on” while

the Speck operates. This is a big advantage over current radio technology employed on the Speck. By leaving the detectors on, it was found that no synchronisation was required between Specks within the network. This meant that messages relayed through the network required less repeating, saving energy across the SpeckNet. The optical transceiver is therefore to be employed in the SpeckNet energy neutral platform. This special Speck is aimed at the long-term low throughput application area. By placing Specks like these in offices they can perform a number of tasks — fire detection is being tested at the moment. They use solar cells optimised for the office environment. During the day the solar cell replenishes the Specks battery completely — this is only possible with the most energy efficient integrated devices. The optical transceiver is one of these devices.

For my devices to be included in the SpeckNet platforms, as just mentioned, packaging was also investigated. The dual-inline package was chosen for its robustness and easy integration into existing electrical circuits. To package the chips wire-bonding was chosen, after optimising the wire-bonding parameters and finding a solution to wire-bonding onto polymer this technique has become very useful throughout the rest of the research group.

Looking back over the project, I would have done a few things differently. I began by looking at bottom emitting VCSELs, these proved easier to fabricate but were not ideal for the packaging solutions eventually chosen. Therefore I should have begun by investigating top emitters and only moved to bottom emitters when they were required (i.e. for coupled VCSEL designs). The liquid crystal work, although providing steering, was far too large for the SpeckNet platform. This was realised quite quickly and I moved on from this work; however time was still spent investigating this technique that could have been spent elsewhere. By neglecting the liquid crystal technique, more time could have been spent on the micro-optics I developed. With more time I could have used a larger e-beam writing machine and could have got more results. Other optical elements could have also been investigated (such as spiral phase plates, for generating optical vortices; and axicon lenses for generating Bessel beams). Using micro-optics could have been useful for other groups within the department as well, especially the optical trapping group where the VCSELs and integrated optics could have been used in micro-fluidic experiments and Raman spectroscopy. As mentioned above, the grating and coupled VCSEL results are very close to realisation, with more time these could have been completed. They could have then been taken further in a number of ways for example by using the sub-wavelength gratings to generate surface-waves that could then be coupled to any direction. The sub-wavelength gratings could also have been used for polarisation control of the VCSELs. This would have been interesting for communication and

location discovery reasons. By employing polarised light and using a polarisation sensitive detector, it should be possible to know the orientation of the transmitting Speck. This allows the 2-dimensional location discovery algorithms to be ported to 3-dimensions far more easily. Polarised light could also be used to mimic radio transmissions. One of the first problems encountered by Strathclyde (the digital signal processing group) was that optical sources cannot produce negative signals (unlike radio) — this then required a re-design of the components. With polarised light, negative signals could be sent using a different polarisation of light. This in turn would mean that the optical and radio transceivers could be analogous and the best one for the task in hand could be chosen before deployment of the SpeckNet. By spending more time on the coupled VCSELs, I believe that dynamic beam steering could have been realised. I also believe that coupled micro-cavities (PhC approach) could have been used to increase the optical power emitted by the VCSELs while keeping their output single mode.

As an addition to the project I think it would have been useful to the SpeckNet collaboration if while looking at optical communications, I had also looked at optical sensors in general. The Speck is an integrated sensor platform and if I could have developed even the simplest optical sensors this would have been useful. The detectors that are used at the moment could be used to detect background light (i.e. day and night, shadows, etc.) but due to their filtering properties these signals would be very small. This may be an advantage for the use of silicon. By integrating wide reception bad detectors (i.e. silicon) with integrated gratings a possible spectrometer could have been fabricated, or at least direction sensing could have been employed. With encapsulation, the VCSEL chips could have been used for absorption measurements, be that in air or liquid, this would have been useful for channel estimation or sample analysis.

To finish I would like to set my project in context by talking a little about the collaboration as a research environment. The SpeckNet collaboration, for one, is quite large including five Universities. Each University brings their own talent to the group and this is a big advantage. Glasgow University contributed expertise in radio technology that allowed interesting discussion about fabrication techniques and a healthy form of competition for the group that achieved the first integrated transceiver array (the optical transceiver with the energy neutral and PerSpeckz platforms were the first fully SpeckNet developed systems). Having a group in Strathclyde who worked on digital signal processing meant that this work did not have to be carried out by myself (even testing of chips can now be farmed out to Strathclyde via Edinburgh). Edinburgh with both their electronics and systems knowledge were extremely useful. The location discovery algorithms that I worked

on at the beginning of my project were passed onto Edinburgh who took them far further than I could ever have, and a close relationship between Edinburgh's electronics experts and myself has been built up over the years.

With the good points to working within a collaboration there come some less than good points as well. Firstly, the project and collaboration existed for a number of years. Over this time the driving forces within the collaboration naturally changed. In my first year, integration and miniaturisation were big issues. As such the VCSEL with as low as possible threshold was chosen as an emitter solution. This limits the eventual power that the VCSEL can emit. However, this didn't matter because total energy use was the concern. The second year brought a shift — miniaturisation was now seen as a future goal and a fully working off-the-shelf platform was put forward. This now meant that power wasn't an issue and other metrics became important such as, for the transceiver, communication distance. With the already developed low power VCSELs this was difficult to achieve. As such these first few years saw a focus on the radio rather than optical systems. This made things more difficult than they had to be. I had to fight, at times, to have my devices considered and having circuitry designed for them was not a choice. However, the third year saw yet another change, to that of the energy neutral platform. Now the low-power optical source was again useful and because I had developed it to an already good standard, integration began to be looked at seriously. I like to summarise these problems with a simple term, that of inertia. I believe that the larger a collaboration the longer it takes as a whole to change its research direction. I believe that if research direction changes had happened more quickly, far more devices and improvements could have already been made to the transceiver arrays.

One other problem that exists within a large collaboration like this is the turn-over seen with the people involved. Naturally PhD students begin projects and when finished move on. However, I found that this turn-over caused some problems with total progress. It took time for a new member of a group to be brought up to speed. Sometimes people weren't brought in to replace leaving members, this then left other people with incomplete projects. Another issue was that of people in different research areas having different research interests. The work I was doing was of great interest to me and my group, however, this was not necessarily true of other people in the collaboration. This meant that work that was required by us, from another group was sometimes held up as they worked on something more interesting to themselves. This is a two-way street and I'm sure that I was as guilty as anyone else of doing this.

This all said, I found working in a collaboration an interesting experience. I can see

Chip Designation	Tx Current mA	Rx Current mA	Frequency GHz
CC1101	15	14	0.3
CC2500 (ZigBee)	12.8	21.6	2.4
CC2420 (ZigBee)	17.4	19.7	2.4

Table 9.1: Table of off-the-shelf radio chips and their key parameters.

that the good points far out-weigh the less than good and would welcome working in another collaboration some day.

To summarise the accomplishments from this project I would like to compare the current SpeckNet transceiver system (i.e. off-the-shelf radio based) with the system I have developed. The radio system uses a number of ChipCom radios (two of which use the ZigBee[®] protocols) their key parameters are listed in table 9.1.

For the comparison of the current radio and optical transceivers a number of factors can be looked at:

- Sensitivity — a typical radio can receive -90 to -100 dBm of power, the optical receiver is sensitive to -50 to -60 dBm.
- Reception power — each radio is driven by a 3 volt supply, so to power a radio receiver requires 40–65 mW. The optical receiver, that I developed, requires only 100 μ W.
- Transmitter power — radios require 45–60 mW for transmission, however, the optical transmitters require less than 15 mW (i.e. 1 mW optical power at a wall-plug efficiency of 7%).

Therefore, the optical system is better than the radio in most of these aspects. However, to achieve such parameters a few tradeoffs have been made. The photodetector is run in photovoltaic mode. This makes the system very low power but limits the systems data rate (currently the optical transceiver is run at approximately 4 kiloBaud, while the radios work at 250 kiloBaud). The detectors also have a relatively low responsivity, i.e. they do not produce a large photocurrent when illuminated. However, they outperform silicon detectors because of their higher background-light rejection ratios (due to their inherent optical filtering).

The next step in the project would be to address these points. The detectors speed is primarily limited by its internal capacitance (this can be lowered by biasing). However, I am currently using VCSEL material to construct the detectors. As such the material is not ideal for detection. Investigation of tailored detector material, with the same filtering properties of the VCSEL material would overcome this issue.

A hybrid wafer design could also be looked at, where the VCSEL is grown on top of the detector wafer — making a detector would then require removal of the top layers of the wafer. By using tailored detector wafers the detectors responsivity would be increased to approximately the same level as the current silicon detectors. This would make the background-light rejection ratio of the new detectors even higher.

The overall focus of this project was to design and fabricate integrate-able components for use within the SpeckNet platform. This has been accomplished. The next steps in the project would be to take these components and develop them further making them more efficient (beam control elements), lower power (optical transmitters) and more sensitive (optical detectors).

Bibliography

- [1] J. Landt and B. Catlin. “Shrouds of Time History of RFID”. Technical report, The Association for Automatic Identification and Data Capture Technologies, <https://www.aimglobal.org>, October 2001. Retrieved January 2009.
- [2] A. Coombs. “The Making of Colossus”. *IEEE Annals of the History of Computing*, 5(3):253, 1983.
- [3] Arthur W. Burks and Alice R. Burks. “First General-Purpose Electronic Computer”. *IEEE Annals of the History of Computing*, 3(4):310–389, 1981.
- [4] Loukas V. Hadellis and Vassilios D. Kapsalis. “Distributed Control Network for Agricultural Applications”. In *Control Applications and Ergonomics in Agriculture IFAC - CAEA 98 Workshop*, pages 14–17, 1998.
- [5] R. Morais and J. Boaventura Cunha. “Agritronics: A Distributed Data Acquisition and Control Network for Agriculture Environments”. In *ISHS Acta Horticulturae 534: International Conference and British-Israeli Workshop on Greenhouse Techniques towards the 3rd Millennium*, pages 319–326, 2000.
- [6] M. Srivastava, R. Muntz, and M. Potkonjak. “Smart kindergarten: sensor-based wireless networks for smart developmental problem-solving environments”. In *MobiCom '01: Proceedings of the 7th annual international conference on Mobile computing and networking*, pages 132–138, New York, NY, USA, 2001. ACM.
- [7] J. Cares, R. Christian, and R. Manke. “Fundamentals of Distributed Networked Military Forces and the Engineering of Distributed Systems”. Technical report, NUWC-NPT Technical Report 11, 366, <http://www.alidade.net>, May 2002. Retrieved January 2009.
- [8] L.Q. Zhuang, W. Liu, J.B. Zhang, D.H. Zhang, and I. Kamajaya. “Distributed asset tracking using wireless sensor network”. In *IEEE International Conference on Emerging Technologies and Factory Automation*, pages 1165–1168, 2008.
- [9] R. Twitchell, Jr. “Network formation in asset-tracking system based on asset class”. US Patent 6934540, August 2005.

- [10] S. Jia, W. Lin, K. Wang, and K. Takase. “Network Distributed Multi-Functional Robotic System Supporting the Elderly and Disabled People”. *J. Intell. Robotics Syst.*, 45(1):53–76, 2006.
- [11] V. Hsu, J. Kahn, and K. Pister. “Wireless Communications for Smart Dust”. Memorandum M98/2, Electronics Research Laboratory, 1998.
- [12] B. Warneke, M. Last, B. Liebowitz, and K.S.J. Pister. “Smart Dust: communicating with a cubic-millimeter computer”. *Computer*, 34(1):44–51, Jan 2001.
- [13] A. Cunha. “The Millibots Project”. Website URL - <http://www.cs.cmu.edu/~cyberscout/new-www/localization.html>, October 1999. Retrieved January 2009.
- [14] Sun Microsystems, Inc. “Sun™ Small Programmable Object Technology (Sun SPOT) Theory of Operation”. Operation manual, Sun Labs, August 2008.
- [15] “SunSpotWorld - Home of Project Sun SPOT”. Website URL - <http://www.sunspotworld.com/>. Retrieved January 2009.
- [16] E. Farella, A. Pieracci, D. Brunelli, L. Benini, B. Riccò, and A. Acquaviva. “Design and Implementation of WiMoCA Node for a Body Area Wireless Sensor Network”. In *ICW/ICHSN/ICMCS/SENET*, pages 342–347, 2005.
- [17] J. Romero. “How Do Motion-Sensing Video Game Controllers Work?”. Website URL - <http://scienceline.org/2006/12/18/motioncontrollers/>, December 2006. Retrieved January 2009.
- [18] D. A. Marx. “Graph coloring problems and their applications in scheduling, Periodica Polytechnica”. In *in Proc. John von Neumann PhD Students Conference*, pages 1–2, 2004.
- [19] Inc. Bluetooth SIG. “Bluetooth.com - The Official Bluetooth®; Technology Info Site”. Website URL - <http://www.bluetooth.com/bluetooth/>. Retrieved March 2009.
- [20] “Wi-Fi Alliance”. Website URL - <http://www.wi-fi.org/>. Retrieved March 2009.
- [21] “Z-Wave - Wireless Home Control Solutions for Your Lighting, Home Entertainment, Energy Management”. Website URL - <http://www.z-wave.com/>. Retrieved March 2009.
- [22] “WiMAX Forum”. Website URL - <http://www.wimaxforum.org/>. Retrieved March 2009.

- [23] “GSM World : Home of the GSM Association”. Website URL - <http://www.gsmworld.com/>. Retrieved March 2009.
- [24] “Infrared Data Association®”. Website URL - <http://www.irda.org/>. Retrieved March 2009.
- [25] “Free Space Optics, FSO, Lasercom informational resource website”. Website URL - <http://www.systemsupportolutions.com/terescope.htm>. Retrieved March 2009.
- [26] “fSONA: free Space Optical Networking Architecture”. Website URL - <http://www.fsona.com/>. Retrieved March 2009.
- [27] “Products for the GSM/Telecom markets - PAVLight Facts”. Website URL - <http://www.pavdata.com/>. Retrieved March 2009.
- [28] “CableFree Solutions - Broadband Wireless - Free Space Optics - High Performance Wireless Networks”. Website URL - <http://www.cablefreesolutions.com/>. Retrieved March 2009.
- [29] S. Haruhisa, K. Iga, C. Kitahara, and Y Suematsu. “GaInAsP/InP Surface Emitting Injection Lasers”. *Japanese Journal of Applied Physics*, 18:2329–2330, aug 1979.
- [30] H. Li and K. Iga, editors. “*Vertical-Cavity Surface-Emitting Laser Devices*”, volume 6 of *Springer Series in Photonics*. Springer, 2002.
- [31] A Miller, M. Ebrahimzadeh, and D. Finlayson, editors. “*Semiconductor Quantum Optoelectronics — from Quantum Physics to Smart Devices*”. Proceedings of the Fiftieth Scottish Universities Summer School in Physics, 1998.
- [32] K.D. Choquette, K.M. Geib, C.I.H. Ashby, R.D. Twisten, O. Blum, H.Q. Hou, D.M. Follstaedt, B.E. Hammons, D. Mathes, and R. Hull. “Advances in selective wet oxidation of AlGaAs alloys”. *Selected Topics in Quantum Electronics, IEEE Journal of*, 3(3):916–926, Jun 1997.
- [33] B. E. Deal and A. S. Grove. “General Relationship for the Thermal Oxidation of Silicon”. *Journal of Applied Physics*, 36(12):3770–3778, 1965.
- [34] M. Ochiai, G. E. Giudice, H. Temkin, J. W. Scott, and T. M. Cockerill. “Kinetics of thermal oxidation of AlAs in water vapor”. *Applied Physics Letters*, 68(14):1898–1900, 1996.
- [35] H Nickel. “A detailed experimental study of the wet oxidation kinetics of $\text{Al}_x\text{Ga}_{1-x}\text{As}$ layers”. *Journal of Applied Physics*, 78(8):5201–5203, 1995.

- [36] P.-C. Ku and C.J. Chang-Hasnain. “Thermal oxidation of AlGaAs: modeling and process control”. *Quantum Electronics, IEEE Journal of*, 39(4):577–585, Apr 2003.
- [37] V. Kudryashov, X. C. Yuan, W. C. Cheong, and K. Radhakrishnan. “Grey scale structures formation in SU-8 with e-beam and UV”. *Microelectronic Engineering*, 67–68:306–311, 2003. Proceedings of the 28th International Conference on Micro- and Nano-Engineering.
- [38] P. Mali, A Sarkar, and R. Lal. “Facile fabrication of microfluidic systems using electron beam lithography”. *Lab Chip*, 6:310–315, 2006.
- [39] D. Daly, R. F. Stevens, M. C. Hutley, and N. Davies. “The manufacture of microlenses by melting photoresist”. *Measurement Science & Technology*, 1(8):759–766, AUG 1990.
- [40] J. Yang, X. Su, P. Xu, and Z. Gu. “Beam steering and deflecting device using step-based micro-blazed grating”. *Optics Communications*, 281(15-16):3969–3976, 2008.
- [41] I.-H. Song, K.-N. Kang, D. S.-W. Park, and P.K. Ajmera. “Microlens array fabrication by backside exposure using Fraunhofer diffraction”. *Microsystem Technologies*, 14:1285–1290, 2008.
- [42] Y. Lu and S. Chen. “Direct write of microlens array using digital projection photopolymerization”. *Applied Physics Letters*, 92(4):041109, 2008.
- [43] V. Garces-Chavez, D. McGloin, H. Melville, W. Sibbett, and K. Dholakia. “Simultaneous micromanipulation in multiple planes using a self-reconstructing light beam”. *Nature*, 419:145–147, 2002.
- [44] Chih-Jen Yang, Su-Hao Liu, Hsing-Hung Hsieh, Chih-Che Liu, Ting-Yi Cho, and Chung-Chih Wu. “Microcavity top-emitting organic light-emitting devices integrated with microlens arrays: Simultaneous enhancement of quantum efficiency, cd/A efficiency, color performances, and image resolution”. *Applied Physics Letters*, 91(25):253508, 2007.
- [45] A. Braeuer, P. Dannberg, U. Zeitner, G. Mann, and W. Karthe. “Application oriented complex polymer microoptics”. *Microsystem Technologies*, 9:304–307, 2003.
- [46] Christopher Reardon, Andrea Di Falco, Karl Welna, and Thomas Krauss. “Integrated polymer micropisms for free spaceoptical beam deflecting”. *Opt. Express*, 17(5):3424–3428, 2009.

- [47] E. Hecht. “*Optics*”. Addison Wesley, fourth edition, 2002.
- [48] M. E. Warren, R. E. Smith, G. A. Vawter, and J. R. Wendt. “High-efficiency subwavelength diffractive optical element in GaAs for 975 nm”. *Opt. Lett.*, 20(12):1441–1443, 1995.
- [49] M. G Moharam, E. B. Grann, D. A. Pommet, and T. K. Gaylord. “Formulation for stable and efficient implementation of the rigorous coupled-wave analysis of binary gratings”. *J. Opt. Soc. Am. A*, 12(5):1068–1076, 1995.
- [50] P Yeh and C Gu. “*Optics of Liquid Crystal Displays*”. Pure and Applied Optics. John Wiley & Sons, Inc., 1999.
- [51] R.A. Morgan, K. Kojima, T. Mullally, G.D. Guth, M.W. Focht, R.E. Leibenguth, and M. Asom. “High-power coherently coupled 8 x 8 vertical cavity surface emitting laser array”. *Applied Physics Letters*, 61(10):1160–1162, 1992.
- [52] A.C. Lehman, J.J. Raftery, Jr., A.J. Danner, P.O. Leisher, and K.D. Choquette. “Relative phase tuning of coupled defects in photonic crystal vertical-cavity surface-emitting lasers”. *Applied Physics Letters*, 88(2):021102, 2006.
- [53] G.V. Treyz. “Silicon Mach-Zehnder waveguide interferometers operating at 1.3 μ m”. *Electronics Letters*, 27(2):118–120, Jan. 1991.
- [54] U. Fischer, T. Zinke, B. Schuppert, and K. Petermann. “Singlemode optical switches based on SOI waveguides with large cross-section”. *Electronics Letters*, 30(5):406–408, Mar 1994.
- [55] D.M. Beggs, T.P. White, L. Cairns, L. O’Faolain, and T.F. Krauss. “Ultra-short Photonic Crystal Optical Switch Actuated by a Microheater”. *Photonics Technology Letters, IEEE*, 21(1):24–26, Jan.1, 2009.
- [56] A.J. Danner, J.C. Lee, J.J. Raftery, N. Yokouchi, and K.D. Choquette. “Coupled-defect photonic crystal vertical cavity surface emitting lasers”. *Electronics Letters*, 39(18):1323–1324, Sept. 2003.
- [57] N. Yokouchi, A.J. Danner, and K.D. Choquette. “Two-dimensional photonic crystal confined vertical-cavity surface-emitting lasers”. *Selected Topics in Quantum Electronics, IEEE Journal of*, 9(5):1439–1445, Sept.-Oct. 2003.
- [58] J.J Raftery, Jr., A.J. Danner, J.C. Lee, and K.D. Choquette. “Coherent coupling of two-dimensional arrays of defect cavities in photonic crystal vertical cavity surface-emitting lasers”. *Applied Physics Letters*, 86(20):201104, 2005.
- [59] P. Russell. “Photonic Crystal Fibers”. *Science*, 299(5605):358–362, 2003.

- [60] K.D. Choquette, J.J. Raftery, and A.C. Lehman. “Beam steering in photonic crystal vertical cavity semiconductor laser arrays”. *Aerospace Conference, 2006 IEEE*, pages 7 pp.–, 2006.
- [61] A.C. Lehman, D.F. Siriani, and K.D. Choquette. “Two-dimensional electronic beam-steering with implant-defined coherent VCSEL arrays”. *Electronics Letters*, 43(22):–, 25 2007.
- [62] T.-C. Lee, C.-Y. Chen, Y.Y. Lin, M.-C. Chou, T.-H. Wu, and R.-K. Lee. “Surface-Structure-Assisted Chaotic Mode Lasing in Vertical Cavity Surface Emitting Lasers”. *Physical Review Letters*, 101(8):084101, 2008.
- [63] N. Fujiwara, Y. Takiguchi, and J. Ohtsubo. “Observation of the synchronization of chaos in mutually injected vertical-cavity surface-emitting semiconductor lasers”. *Opt. Lett.*, 28(18):1677–1679, 2003.
- [64] I.V. Babushkin, M. Schulz-Ruhtenberg, N.A. Loiko, K.F. Huang, and T. Ackemann. “Coupling of Polarization and Spatial Degrees of Freedom of Highly Divergent Emission in Broad-Area Square Vertical-Cavity Surface-Emitting Lasers”. *Physical Review Letters*, 100(21):213901, 2008.
- [65] J. Wiersig and M. Hentschel. “Combining Directional Light Output and Ultralow Loss in Deformed Microdisks”. *Physical Review Letters*, 100(3):033901, 2008.
- [66] L.D.A. Lundberg and E. Kapon. “Mode switching and beam steering in photonic crystal heterostructures implemented with vertical-cavity surface-emitting lasers”. *Applied Physics Letters*, 90(24):241115, 2007.
- [67] A. Valle, M. Arizaleta, H. Thienpont, K. Panajotov, and M. Sciamanna. “Transverse mode competition effects on the dynamics of gain-switched vertical-cavity surface-emitting lasers”. *Applied Physics Letters*, 93(13):131103, 2008.
- [68] A. Valle, M. Sciamanna, and K. Panajotov. “Nonlinear dynamics of the polarization of multitransverse mode vertical-cavity surface-emitting lasers under current modulation”. *Physical Review E (Statistical, Nonlinear, and Soft Matter Physics)*, 76(4):046206, 2007.
- [69] Hamamatsu, Solid State Division. “*Si photodiode S2387 series*”. Device - S2387-66R, Datasheet Retrieved - February 2009.
- [70] OSRAM Opto Semiconductors GmbH. “*Silicon PIN Photodiode with Very Short Switching Time*”. Device - SFH 203 FA, Datasheet Retrieved - February 2009.

- [71] “*Silicon PIN Photodiode with Daylight Filter; in SMT and as Reverse Gull-wing*”. Device - BPW 34 FA, Datasheet Retrieved - February 2009.
- [72] “*PD410PI High Speed Photodiode*”. Device - PD410PI, Datasheet Retrieved - February 2009.
- [73] D. Sameoto, S.-W. Lee, and M. Parameswaran. “Electrical interconnection through optimized wirebonding onto SU-8 structures and actuators”. *Journal of Micromechanics and Microengineering*, 18(7), July 2008.

Appendix

Connectivity Test taking into account number of VCSELS

```
<<Graphics'Arrow'
DrawSpeck[coord_]:=
  Graphics[{Arrow[{coord\[LeftDoubleBracket]1\[RightDoubleBracket],
    coord\[LeftDoubleBracket]2\[RightDoubleBracket]}},{coord\
\[LeftDoubleBracket]1\[RightDoubleBracket]+2 Cos[
    coord\[LeftDoubleBracket]3\[RightDoubleBracket]Degree],
    coord\[LeftDoubleBracket]2\[RightDoubleBracket]+2 Sin[
    coord\[LeftDoubleBracket]3\[RightDoubleBracket]Degree]}],
  HeadScaling\[Rule]Relative],
  Disk[{coord\[LeftDoubleBracket]1\[RightDoubleBracket],
    coord\[LeftDoubleBracket]2\[RightDoubleBracket]},0.3]
}]

dim=10;
Num=100;
Leds=1;
exp=1;
threshold=2;

randomPositionListxy=
  Table[{Round[Random[Real,{-dim,dim}]],Round[Random[Real,{-dim,dim}]]},
    Round[Random[Real,{0,360}]]},{i,Num}];

(*This section takes each Speck in turn and transforms its position along \
with all other Specks in-order to place the first Speck at (0,0,0)*)
transX[a_,
  b_]:= (a\[LeftDoubleBracket]1\[RightDoubleBracket]-
    b\[LeftDoubleBracket]1\[RightDoubleBracket])Cos[
    b\[LeftDoubleBracket]3\[RightDoubleBracket] Degree]+(a\
\[LeftDoubleBracket]2\[RightDoubleBracket]-
    b\[LeftDoubleBracket]2\[RightDoubleBracket])Sin[
    b\[LeftDoubleBracket]3\[RightDoubleBracket]Degree];
transY[a_,
  b_]:= -(a\[LeftDoubleBracket]1\[RightDoubleBracket]-
    b\[LeftDoubleBracket]1\[RightDoubleBracket])Sin[
    b\[LeftDoubleBracket]3\[RightDoubleBracket]Degree]+(a\
```

```

\[LeftDoubleBracket]2\[RightDoubleBracket]-
    b\[LeftDoubleBracket]2\[RightDoubleBracket])Cos[
    b\[LeftDoubleBracket]3\[RightDoubleBracket]Degree];
trans\[Theta][a_,b_]:=
    a\[LeftDoubleBracket]3\[RightDoubleBracket]-
    b\[LeftDoubleBracket]3\[RightDoubleBracket];

transformXYTable=
    Table[Table[{transX[
        randomPositionListxy\[LeftDoubleBracket]i\[RightDoubleBracket],
        randomPositionListxy\[LeftDoubleBracket]n\[RightDoubleBracket]]//
    N,transY[
        randomPositionListxy\[LeftDoubleBracket]i\[RightDoubleBracket],
        randomPositionListxy\[LeftDoubleBracket]n\[RightDoubleBracket]]//
    N,
    trans\[Theta][
        randomPositionListxy\[LeftDoubleBracket]i\[RightDoubleBracket],
        randomPositionListxy\[LeftDoubleBracket]n\[RightDoubleBracket]]//
    N},{i,1,Length[randomPositionListxy]},{n,1,Num}];

r[x_,y_]=Sqrt[x^2+y^2];
\[Theta][x_,y_]=(ArcTan[x,y]);

(*This part calculates the radius for each LED on one Speck in order to talk \
to each other Speck within the field*)
rule = Table[
    Table[Flatten[
        Table[If[
            transformXYTable\[LeftDoubleBracket]j,i,
            1\[RightDoubleBracket]\[Equal]0&&
            transformXYTable\[LeftDoubleBracket]j,i,
            2\[RightDoubleBracket]\[Equal]0,{r\[Rule]0},
            NSolve[{r Cos\[Theta][
                transformXYTable\[LeftDoubleBracket]j,i,
                1\[RightDoubleBracket],
                transformXYTable\[LeftDoubleBracket]j,i,
                2\[RightDoubleBracket]] + n^2\[Pi]/Leds ]^
                exp\[Equal]r[
                transformXYTable\[LeftDoubleBracket]j,i,
                1\[RightDoubleBracket],
                transformXYTable\[LeftDoubleBracket]j,i,
                2\[RightDoubleBracket]]},{r}],{n,0,(Leds-1)}}],{i,
            1,Length[
                transformXYTable\[LeftDoubleBracket]j\[RightDoubleBracket]]},{j,
            1,Length[transformXYTable]}}];

(*This section takes the radius data and removes the non-
sensical ones i.e.

```



```

        negative and zero (zero means the specks either coincide or its \
trying to calculate radius data for itself)*)
rspeck=Table[
  Table[Table[
    r/.rule\[LeftDoubleBracket]j,i,n\[RightDoubleBracket],{n,1,
      Leds}],{i,1,
    Length[transformXYTable\[LeftDoubleBracket]j\[RightDoubleBracket]]]\
,{j,1,Length[transformXYTable]}];
rspeck=Table[
  Table[Table[
    If[rspeck\[LeftDoubleBracket]k,j,i\[RightDoubleBracket]<0,0,
      rspeck\[LeftDoubleBracket]k,j,i\[RightDoubleBracket]],{i,1,
      Length[rspeck\[LeftDoubleBracket]1,1\[RightDoubleBracket]]}],{j,1,
      Length[rspeck\[LeftDoubleBracket]1\[RightDoubleBracket]]}],{k,1,
      Length[rspeck\[LeftDoubleBracket]\[RightDoubleBracket]]];
rspeck=Table[
  Table[Select[
    rspeck\[LeftDoubleBracket]j,i\[RightDoubleBracket],#>0&],{i,1,
    Length[rspeck\[LeftDoubleBracket]1\[RightDoubleBracket]]}],{j,1,
    Length[rspeck]}];

(*This section takes radius data and calculates,
using minimum from radius table, the connectivity for each Speck*)
connectivityTable=
  Table[Select[
    Select[Table[
      If[Length[rspeck\[LeftDoubleBracket]j,i\[RightDoubleBracket]]>0,
        Min[rspeck\[LeftDoubleBracket]j,i\[RightDoubleBracket]],0],{i,
        1,Length[
          rspeck\[LeftDoubleBracket]j\[RightDoubleBracket]]],#>0&],#<
        threshold&]//Length,{j,1,Length[rspeck]}];

averageCon=Mean[connectivityTable]//N

SpeckNet:=Table[
  DrawSpeck[{randomPositionListxy\[LeftDoubleBracket]i,
    1\[RightDoubleBracket],
    randomPositionListxy\[LeftDoubleBracket]i,2\[RightDoubleBracket],
    randomPositionListxy\[LeftDoubleBracket]i,
    3\[RightDoubleBracket]}],{i,1,Length[randomPositionListxy]}];
Show[
  SpeckNet,
  PlotRange\[Rule]{{-dim,dim},{-dim,dim}}, Axes\[Rule]False,Frame\[Rule]True,
  FrameTicks \[Rule]True, AspectRatio\[Rule]1]

a1=Table[Table[
  Leds=1;exp=21;

  xStart=-0.5;xEnd=0.5;

```

```

yStart=-0.5;yEnd=0.5;
radius=0.3;

Density=1*j;

SpeckNum=(xEnd-xStart)*(yEnd-yStart)*Density;
randomPositionListxy=
  Table[{Random[Real,{xStart,xEnd}],Random[Real,{yStart,yEnd}],
    Random[Real,{0,360}]},{i,SpeckNum}];

(*This section takes each Speck in turn and transforms its position \
along with all other Specks in-order to place the first Speck at (0,0,0)*)
transX[a_,
  b_]:= (a\[LeftDoubleBracket]1\[RightDoubleBracket]-
    b\[LeftDoubleBracket]1\[RightDoubleBracket])Cos[
    b\[LeftDoubleBracket]3\[RightDoubleBracket] Degree]+(a\
\[LeftDoubleBracket]2\[RightDoubleBracket]-
    b\[LeftDoubleBracket]2\[RightDoubleBracket])Sin[
    b\[LeftDoubleBracket]3\[RightDoubleBracket]Degree];
transY[a_,
  b_]:= -(a\[LeftDoubleBracket]1\[RightDoubleBracket]-
    b\[LeftDoubleBracket]1\[RightDoubleBracket])Sin[
    b\[LeftDoubleBracket]3\[RightDoubleBracket]Degree]+(a\
\[LeftDoubleBracket]2\[RightDoubleBracket]-
    b\[LeftDoubleBracket]2\[RightDoubleBracket])Cos[
    b\[LeftDoubleBracket]3\[RightDoubleBracket]Degree];
trans\[Theta][a_,b_]:=
  a\[LeftDoubleBracket]3\[RightDoubleBracket]-
  b\[LeftDoubleBracket]3\[RightDoubleBracket];

transformXYTable=
  Table[Table[{transX[
    randomPositionListxy\[LeftDoubleBracket]
    i\[RightDoubleBracket],
    randomPositionListxy\[LeftDoubleBracket]
    n\[RightDoubleBracket]]//N,
  transY[randomPositionListxy\[LeftDoubleBracket]
    i\[RightDoubleBracket],
    randomPositionListxy\[LeftDoubleBracket]
    n\[RightDoubleBracket]]//N,
  trans\[Theta][
    randomPositionListxy\[LeftDoubleBracket]
    i\[RightDoubleBracket],
    randomPositionListxy\[LeftDoubleBracket]
    n\[RightDoubleBracket]]//N},{i,1,
  Length[randomPositionListxy]}],{n,1,SpeckNum}];

r[x_,y_]=Sqrt[x^2+y^2];
\[Theta][x_,y_]=(ArcTan[x,y]);

```

```

(*This part calculates the radius for each LED on one Speck in order \
to talk to each other Speck within the field*)
rule =
Table[Table[
  Flatten[Table[
    If[transformXYTable\[LeftDoubleBracket]j,i,
      1\[RightDoubleBracket]\[Equal]0&&
      transformXYTable\[LeftDoubleBracket]j,i,
      2\[RightDoubleBracket]\[Equal]0,{r\[Rule]0},
    NSolve[{r Cos\[Theta][
      transformXYTable\[LeftDoubleBracket]j,i,
      1\[RightDoubleBracket],
      transformXYTable\[LeftDoubleBracket]j,i,
      2\[RightDoubleBracket]] +
      n 2\[Pi]/Leds ]^exp\[Equal]r[
      transformXYTable\[LeftDoubleBracket]j,i,
      1\[RightDoubleBracket],
      transformXYTable\[LeftDoubleBracket]j,i,
      2\[RightDoubleBracket]] },{r}]], {n,
    0,(Leds-1)}]],{i,1,
  Length[transformXYTable\[LeftDoubleBracket]j\
\[RightDoubleBracket]]}],{j,1,Length[transformXYTable]}];

(*This section takes the radius data and removes the non-
sensical ones i.e.
negative and zero (zero means the specks either coincide or \
its trying to calculate radius data for itself)*)
rspeck=
Table[Table[
  Table[r/.rule\[LeftDoubleBracket]j,i,n\[RightDoubleBracket],{n,
    1,Leds}],{i,1,
  Length[transformXYTable\[LeftDoubleBracket]j\
\[RightDoubleBracket]]}],{j,1,Length[transformXYTable]}];
rspeck=
Table[Table[
  Table[If[rspeck\[LeftDoubleBracket]k,j,i\[RightDoubleBracket]<0,
    0,rspeck\[LeftDoubleBracket]k,j,i\[RightDoubleBracket]],{i,
    1,Length[
      rspeck\[LeftDoubleBracket]1,1\[RightDoubleBracket]]}],{j,
    1,Length[
      rspeck\[LeftDoubleBracket]1\[RightDoubleBracket]]}],{k,1,
  Length[rspeck\[LeftDoubleBracket]1\[RightDoubleBracket]]}];
rspeck=
Table[Table[
  Select[rspeck\[LeftDoubleBracket]j,
    i\[RightDoubleBracket],#>0&],{i,1,
  Length[rspeck\[LeftDoubleBracket]1\[RightDoubleBracket]]}],{j,
    1,Length[rspeck]}];

```

```

(*This section takes radius data and calculates,
  using minimum from radius table, the connectivity for each Speck*)
connectivityTable=
Table[
  Select[Select[
    Table[If[
      Length[rspeck\[LeftDoubleBracket]j,
        i\[RightDoubleBracket]]>0,
      Min[rspeck\[LeftDoubleBracket]j,i\[RightDoubleBracket]],
      0],{i,1,
        Length[rspeck\[LeftDoubleBracket]
          j\[RightDoubleBracket]]},#>0&],#<radius&]//
    Length,{j,1,Length[rspeck]}}];

averageCon=Mean[connectivityTable]//N
,{i,10},{j,1,6000,100}}];

Export["C:\Documents and Settings\Christopher Reardon\Desktop\Mathematica \
Data\VCSEL Config\VCSELS1Radius03vDens",a1]

mean=Table[
  Mean[a1\[LeftDoubleBracket]i\[RightDoubleBracket]],{i,Length[a1]}}];
ListPlot[mean,PlotLabel\[Rule]"SpeckNet Connectivity Standard Deviation",
  PlotJoined\[Rule]True,
  PlotRange\[Rule]{Min[mean]-((Max[mean]-Min[mean])/4),
    Max[mean]+((Max[mean]-Min[mean])/4)}}];

b1=Table[Table[
  Leds=2;exp=21;

  xStart=-0.5;xEnd=0.5;
  yStart=-0.5;yEnd=0.5;
  radius=0.3;

  Density=1*j;

  SpeckNum=(xEnd-xStart)*(yEnd-yStart)*Density;
  randomPositionListxy=
    Table[{Random[Real,{xStart,xEnd}],Random[Real,{yStart,yEnd}],
      Random[Real,{0,360}]}],{i,SpeckNum}];

  (*This section takes each Speck in turn and transforms its position \
  along with all other Specks in-order to place the first Speck at (0,0,0)*)
  transX[a_,
    b_]:= (a\[LeftDoubleBracket]1\[RightDoubleBracket]-
      b\[LeftDoubleBracket]1\[RightDoubleBracket])Cos[
      b\[LeftDoubleBracket]3\[RightDoubleBracket] Degree]+(a\

```

```

\[LeftDoubleBracket]2\[RightDoubleBracket]-
    b\[LeftDoubleBracket]2\[RightDoubleBracket])Sin[
    b\[LeftDoubleBracket]3\[RightDoubleBracket]Degree];
transY[a_,
    b_]:=-(a\[LeftDoubleBracket]1\[RightDoubleBracket]-
    b\[LeftDoubleBracket]1\[RightDoubleBracket])Sin[
    b\[LeftDoubleBracket]3\[RightDoubleBracket]Degree]+(a\[
\[LeftDoubleBracket]2\[RightDoubleBracket]-
    b\[LeftDoubleBracket]2\[RightDoubleBracket])Cos[
    b\[LeftDoubleBracket]3\[RightDoubleBracket]Degree];
trans\[Theta][a_,b_]:=
    a\[LeftDoubleBracket]3\[RightDoubleBracket]-
    b\[LeftDoubleBracket]3\[RightDoubleBracket];

transformXYTable=
    Table[Table[{transX[
        randomPositionListxy\[LeftDoubleBracket]
        i\[RightDoubleBracket],
        randomPositionListxy\[LeftDoubleBracket]
        n\[RightDoubleBracket]//N,
    transY[randomPositionListxy\[LeftDoubleBracket]
        i\[RightDoubleBracket],
        randomPositionListxy\[LeftDoubleBracket]
        n\[RightDoubleBracket]//N,
    trans\[Theta][
        randomPositionListxy\[LeftDoubleBracket]
        i\[RightDoubleBracket],
        randomPositionListxy\[LeftDoubleBracket]
        n\[RightDoubleBracket]//N},{i,1,
    Length[randomPositionListxy]}],{n,1,SpeckNum}];

r[x_,y_]=Sqrt[x^2+y^2];
\[Theta][x_,y_]=(ArcTan[x,y]);

(*This part calculates the radius for each LED on one Speck in order \
to talk to each other Speck within the field*)
rule =
    Table[Table[
        Flatten[Table[
            If[transformXYTable\[LeftDoubleBracket]j,i,
                1\[RightDoubleBracket]\[Equal]0&&
                transformXYTable\[LeftDoubleBracket]j,i,
                2\[RightDoubleBracket]\[Equal]0,{r\[Rule]0},
            NSolve[{r Cos\[Theta][
                transformXYTable\[LeftDoubleBracket]j,i,
                1\[RightDoubleBracket],
                transformXYTable\[LeftDoubleBracket]j,i,
                2\[RightDoubleBracket]] +

```

```

n 2\[Pi]/Leds ]^exp\[Equal]r[
transformXYTable\[LeftDoubleBracket]j,i,
1\[RightDoubleBracket],
transformXYTable\[LeftDoubleBracket]j,i,
2\[RightDoubleBracket]] ],{r}]], {n,
0,(Leds-1)}}],{i,1,
Length[transformXYTable\[LeftDoubleBracket]j\
\[RightDoubleBracket]]}],{j,1,Length[transformXYTable]}}];

(*This section takes the radius data and removes the non-
sensual ones i.e.
negative and zero (zero means the specks either coincide or \
its trying to calculate radius data for itself)*)
rspeck=
Table[Table[
Table[r/.rule\[LeftDoubleBracket]j,i,n\[RightDoubleBracket],{n,
1,Leds}],{i,1,
Length[transformXYTable\[LeftDoubleBracket]j\
\[RightDoubleBracket]]}],{j,1,Length[transformXYTable]}}];
rspeck=
Table[Table[
Table[If[rspeck\[LeftDoubleBracket]k,j,i\[RightDoubleBracket]<0,
0,rspeck\[LeftDoubleBracket]k,j,i\[RightDoubleBracket]],{i,
1,Length[
rspeck\[LeftDoubleBracket]1,1\[RightDoubleBracket]]}],{j,
1,Length[
rspeck\[LeftDoubleBracket]1\[RightDoubleBracket]]}],{k,1,
Length[rspeck\[LeftDoubleBracket]\[RightDoubleBracket]]}];
rspeck=
Table[Table[
Select[rspeck\[LeftDoubleBracket]j,
i\[RightDoubleBracket],#>0&],{i,1,
Length[rspeck\[LeftDoubleBracket]1\[RightDoubleBracket]]}],{j,
1,Length[rspeck]}}];

(*This section takes radius data and calculates,
using minimum from radius table, the connectivity for each Speck*)
connectivityTable=
Table[
Select[Select[
Table[If[
Length[rspeck\[LeftDoubleBracket]j,
i\[RightDoubleBracket]]>0,
Min[rspeck\[LeftDoubleBracket]j,i\[RightDoubleBracket]],
0],{i,1,
Length[rspeck\[LeftDoubleBracket]
j\[RightDoubleBracket]]}],#>0&],#<radius&]//
Length,{j,1,Length[rspeck]}}];

```

```

averageCon=Mean[connectivityTable]/N
,{i,10}],{j,1,6000,100}];

Export["C:\Documents and Settings\Christopher Reardon\Desktop\Mathematica \
Data\VCSEL Config\VCSELS2Radius03vDens",b1]

mean=Table[
  Mean[b1\[LeftDoubleBracket]i\[RightDoubleBracket]],{i,Length[b1]};
ListPlot[mean,PlotLabel\[Rule]"SpeckNet Connectivity Standard Deviation",
  PlotJoined\[Rule]True,
  PlotRange\[Rule]{Min[mean]-((Max[mean]-Min[mean])/4),
    Max[mean]+((Max[mean]-Min[mean])/4)}];

c1=Table[Table[
  Leds=3;exp=21;

  xStart=-0.5;xEnd=0.5;
  yStart=-0.5;yEnd=0.5;
  radius=0.3;

  Density=1*j;

  SpeckNum=(xEnd-xStart)*(yEnd-yStart)*Density;
  randomPositionListxy=
    Table[{Random[Real,{xStart,xEnd}],Random[Real,{yStart,yEnd}],
      Random[Real,{0,360}]},{i,SpeckNum}];

  (*This section takes each Speck in turn and transforms its position \
  along with all other Specks in-order to place the first Speck at (0,0,0)*)
  transX[a_,
    b_]:=(a\[LeftDoubleBracket]1\[RightDoubleBracket]-
      b\[LeftDoubleBracket]1\[RightDoubleBracket])Cos[
      b\[LeftDoubleBracket]3\[RightDoubleBracket] Degree]+(a\[
\LeftDoubleBracket]2\[RightDoubleBracket]-
      b\[LeftDoubleBracket]2\[RightDoubleBracket])Sin[
      b\[LeftDoubleBracket]3\[RightDoubleBracket]Degree];
  transY[a_,
    b_]:=-(a\[LeftDoubleBracket]1\[RightDoubleBracket]-
      b\[LeftDoubleBracket]1\[RightDoubleBracket])Sin[
      b\[LeftDoubleBracket]3\[RightDoubleBracket]Degree]+(a\[
\LeftDoubleBracket]2\[RightDoubleBracket]-
      b\[LeftDoubleBracket]2\[RightDoubleBracket])Cos[
      b\[LeftDoubleBracket]3\[RightDoubleBracket]Degree];
  trans\[Theta][a_,b_]:=
    a\[LeftDoubleBracket]3\[RightDoubleBracket]-
    b\[LeftDoubleBracket]3\[RightDoubleBracket];

  transformXYTable=

```

```

Table[Table[{transX[
    randomPositionListxy\[LeftDoubleBracket]
    i\[RightDoubleBracket],
    randomPositionListxy\[LeftDoubleBracket]
    n\[RightDoubleBracket]]//N,
transY[randomPositionListxy\[LeftDoubleBracket]
    i\[RightDoubleBracket],
    randomPositionListxy\[LeftDoubleBracket]
    n\[RightDoubleBracket]]//N,
trans\[Theta][
    randomPositionListxy\[LeftDoubleBracket]
    i\[RightDoubleBracket],
    randomPositionListxy\[LeftDoubleBracket]
    n\[RightDoubleBracket]]//N},{i,1,
Length[randomPositionListxy]}],{n,1,SpeckNum}];

r[x_,y_]=Sqrt[x^2+y^2];
\[Theta][x_,y_]=(ArcTan[x,y]);

(*This part calculates the radius for each LED on one Speck in order \
to talk to each other Speck within the field*)
rule =
Table[Table[
    Flatten[Table[
        If[transformXYTable\[LeftDoubleBracket]j,i,
            1\[RightDoubleBracket]\[Equal]0&&
            transformXYTable\[LeftDoubleBracket]j,i,
            2\[RightDoubleBracket]\[Equal]0,{r\[Rule]0},
        NSolve[{r Cos\[Theta][
            transformXYTable\[LeftDoubleBracket]j,i,
            1\[RightDoubleBracket],
            transformXYTable\[LeftDoubleBracket]j,i,
            2\[RightDoubleBracket]] +
            n 2\[Pi]/Leds ]^exp\[Equal]r[
            transformXYTable\[LeftDoubleBracket]j,i,
            1\[RightDoubleBracket],
            transformXYTable\[LeftDoubleBracket]j,i,
            2\[RightDoubleBracket]] },{r}]], {n,
            0,(Leds-1)}]],{i,1,
            Length[transformXYTable\[LeftDoubleBracket]j\
\[RightDoubleBracket]]}],{j,1,Length[transformXYTable]}];

(*This section takes the radius data and removes the non-
sensical ones i.e.
negative and zero (zero means the specks either coincide or \
its trying to calculate radius data for itself)*)
rspeck=
Table[Table[
    Table[r/.rule\[LeftDoubleBracket]j,i,n\[RightDoubleBracket],{n,

```



```

1,Leds}},{i,1,
Length[transformXYTable\[LeftDoubleBracket]j\
\[RightDoubleBracket]]}],{j,1,Length[transformXYTable]}];
rspeck=
Table[Table[
Table[If[rspeck\[LeftDoubleBracket]k,j,i\[RightDoubleBracket]<0,
0,rspeck\[LeftDoubleBracket]k,j,i\[RightDoubleBracket]],{i,
1,Length[
rspeck\[LeftDoubleBracket]1,1\[RightDoubleBracket]]}],{j,
1,Length[
rspeck\[LeftDoubleBracket]1\[RightDoubleBracket]]}],{k,1,
Length[rspeck\[LeftDoubleBracket]\[RightDoubleBracket]]}];
rspeck=
Table[Table[
Select[rspeck\[LeftDoubleBracket]j,
i\[RightDoubleBracket],#>0&],{i,1,
Length[rspeck\[LeftDoubleBracket]1\[RightDoubleBracket]]}],{j,
1,Length[rspeck]}];

(*This section takes radius data and calculates,
using minimum from radius table, the connectivity for each Speck*)
connectivityTable=
Table[
Select[Select[
Table[If[
Length[rspeck\[LeftDoubleBracket]j,
i\[RightDoubleBracket]]>0,
Min[rspeck\[LeftDoubleBracket]j,i\[RightDoubleBracket]],
0],{i,1,
Length[rspeck\[LeftDoubleBracket]
j\[RightDoubleBracket]]}],#>0&],#<radius&]//
Length,{j,1,Length[rspeck]}];

averageCon=Mean[connectivityTable]//N
,{i,10}],{j,1,6000,100}];

Export["C:\Documents and Settings\Christopher Reardon\Desktop\Mathematica \
Data\VCSEL Config\VCSELS3Radius03vDens",c1]

mean=Table[
Mean[c1\[LeftDoubleBracket]i\[RightDoubleBracket]],{i,Length[c1]}];
ListPlot[mean,PlotLabel\[Rule]"SpeckNet Connectivity Standard Deviation",
PlotJoined\[Rule]True,
PlotRange\[Rule]{Min[mean]-((Max[mean]-Min[mean])/4),
Max[mean]+((Max[mean]-Min[mean])/4)}];

d1=Table[Table[
Leds=4;exp=21;

```

```

xStart=-0.5;xEnd=0.5;
yStart=-0.5;yEnd=0.5;
radius=0.3;

Density=1*j;

SpeckNum=(xEnd-xStart)*(yEnd-yStart)*Density;
randomPositionListxy=
  Table[{Random[Real,{xStart,xEnd}],Random[Real,{yStart,yEnd}],
    Random[Real,{0,360}]},{i,SpeckNum}];

(*This section takes each Speck in turn and transforms its position \
along with all other Specks in-order to place the first Speck at (0,0,0)*)
transX[a_,
  b_]:= (a\[LeftDoubleBracket]1\[RightDoubleBracket]-
    b\[LeftDoubleBracket]1\[RightDoubleBracket])Cos[
    b\[LeftDoubleBracket]3\[RightDoubleBracket] Degree]+(a\
\[LeftDoubleBracket]2\[RightDoubleBracket]-
    b\[LeftDoubleBracket]2\[RightDoubleBracket])Sin[
    b\[LeftDoubleBracket]3\[RightDoubleBracket]Degree];
transY[a_,
  b_]:= -(a\[LeftDoubleBracket]1\[RightDoubleBracket]-
    b\[LeftDoubleBracket]1\[RightDoubleBracket])Sin[
    b\[LeftDoubleBracket]3\[RightDoubleBracket]Degree]+(a\
\[LeftDoubleBracket]2\[RightDoubleBracket]-
    b\[LeftDoubleBracket]2\[RightDoubleBracket])Cos[
    b\[LeftDoubleBracket]3\[RightDoubleBracket]Degree];
trans\[Theta][a_,b_]:=
  a\[LeftDoubleBracket]3\[RightDoubleBracket]-
  b\[LeftDoubleBracket]3\[RightDoubleBracket];

transformXYTable=
  Table[Table[{transX[
    randomPositionListxy\[LeftDoubleBracket]
    i\[RightDoubleBracket],
    randomPositionListxy\[LeftDoubleBracket]
    n\[RightDoubleBracket]]//N,
  transY[randomPositionListxy\[LeftDoubleBracket]
    i\[RightDoubleBracket],
    randomPositionListxy\[LeftDoubleBracket]
    n\[RightDoubleBracket]]//N,
  trans\[Theta][
    randomPositionListxy\[LeftDoubleBracket]
    i\[RightDoubleBracket],
    randomPositionListxy\[LeftDoubleBracket]
    n\[RightDoubleBracket]]//N},{i,1,
  Length[randomPositionListxy]}],{n,1,SpeckNum}];

```

```

r[x_,y_]=Sqrt[x^2+y^2];
\[Theta][x_,y_]=(ArcTan[x,y]);

(*This part calculates the radius for each LED on one Speck in order \
to talk to each other Speck within the field*)
rule =
Table[Table[
  Flatten[Table[
    If[transformXYTable\[LeftDoubleBracket]j,i,
      1\[RightDoubleBracket]\[Equal]0&&
      transformXYTable\[LeftDoubleBracket]j,i,
      2\[RightDoubleBracket]\[Equal]0,{r\[Rule]0},
      NSolve[{r Cos\[Theta][
        transformXYTable\[LeftDoubleBracket]j,i,
        1\[RightDoubleBracket],
        transformXYTable\[LeftDoubleBracket]j,i,
        2\[RightDoubleBracket]] +
        n 2\[Pi]/Leds ]^exp\[Equal]r[
        transformXYTable\[LeftDoubleBracket]j,i,
        1\[RightDoubleBracket],
        transformXYTable\[LeftDoubleBracket]j,i,
        2\[RightDoubleBracket]] },{r}]], {n,
        0,(Leds-1)}}],{i,1,
        Length[transformXYTable\[LeftDoubleBracket]j\
\[RightDoubleBracket]]}],{j,1,Length[transformXYTable]}];

(*This section takes the radius data and removes the non-
sensical ones i.e.
negative and zero (zero means the specks either coincide or \
its trying to calculate radius data for itself)*)
rspeck=
Table[Table[
  Table[r/.rule\[LeftDoubleBracket]j,i,n\[RightDoubleBracket],{n,
    1,Leds}],{i,1,
    Length[transformXYTable\[LeftDoubleBracket]j\
\[RightDoubleBracket]]}],{j,1,Length[transformXYTable]}];
rspeck=
Table[Table[
  Table[If[rspeck\[LeftDoubleBracket]k,j,i\[RightDoubleBracket]<0,
    0,rspeck\[LeftDoubleBracket]k,j,i\[RightDoubleBracket]],{i,
    1,Length[
      rspeck\[LeftDoubleBracket]1,1\[RightDoubleBracket]]}],{j,
    1,Length[
      rspeck\[LeftDoubleBracket]1\[RightDoubleBracket]]}],{k,1,
    Length[rspeck\[LeftDoubleBracket]\[RightDoubleBracket]]}];
rspeck=
Table[Table[
  Select[rspeck\[LeftDoubleBracket]j,
    i\[RightDoubleBracket],#>0&],{i,1,

```

```

Length[rspeck\[LeftDoubleBracket]1\[RightDoubleBracket]]},{j,
1,Length[rspeck]}}];

(*This section takes radius data and calculates,
using minimum from radius table, the connectivity for each Speck*)
connectivityTable=
Table[
  Select[Select[
    Table[If[
      Length[rspeck\[LeftDoubleBracket]j,
        i\[RightDoubleBracket]]>0,
      Min[rspeck\[LeftDoubleBracket]j,i\[RightDoubleBracket]],
      0},{i,1,
      Length[rspeck\[LeftDoubleBracket]
        j\[RightDoubleBracket]]},#>0&],#<radius&]//
    Length,{j,1,Length[rspeck]}}];

averageCon=Mean[connectivityTable]//N
,{i,10},{j,1,6000,100}];

Export["C:\Documents and Settings\Christopher Reardon\Desktop\Mathematica \
Data\VCSEL Config\VCSELS4Radius03vDens",d1]

mean=Table[
  Mean[d1\[LeftDoubleBracket]i\[RightDoubleBracket]],{i,Length[d1]}}];
ListPlot[mean,PlotLabel\[Rule]"SpeckNet Connectivity Standard Deviation",
PlotJoined\[Rule]True,
PlotRange\[Rule]{Min[mean]-((Max[mean]-Min[mean])/4),
  Max[mean]+((Max[mean]-Min[mean])/4)}}];

```